ANALYSIS OF THE DEVELOPMENT OF DYNAMIC STALL BASED ON OSCILLATING AIRFOIL EXPERIMENTS

Lawrence W. Carr, Kenneth W. McAlister, and William J. McCroskey

Ames Research Center
and U.S. Army Air Mobility R&D Laboratory
Moffett Field, Calif. 94035

1. Report No. NASA TN D-8382	2. Government Accession No.	3. Recipient's Catalog No.
4. Title and Subtitle ANALYSIS OF THE DEVELOPMENT OF DYNAMIC STALL BASED ON OSCILLATING AIRFOIL EXPERIMENTS		5. Report Date January 1977
		6. Performing Organization Code
7. Author(s) Lawrence W. Carr, Kenneth W. McAlister, and William J. McCroskey		8. Performing Organization Report No. A-6674
		10. Work Unit No.
9. Performing Organization Name and Address Ames Research Center, NASA and Ames Directorate, USAAMRDL Ames Research Center, Moffett Field, CA 94035		
		11. Contract or Grant No.
		13. Type of Report and Period Covered Technical Note
12. Sponsoring Agency Name and Address NASA, Washington, D.C. 20546 and US Army Air Mobility R&D Laboratory Moffett Field, CA 94035		
		14. Sponsoring Agency Code
15. Supplementary Notes		

16. Abstract

The effects of dynamic stall on airfoils oscillating in pitch were investigated by experimentally determining the viscous and inviscid characteristics of the airflow on the NACA 0012 airfoil and on several leading-edge modifications. The test parameters included a wide range of frequencies, Reynolds numbers, and amplitudes-of-oscillation. Three distinct types of separation development were observed within the boundary layer, each leading to classical dynamic stall. The NACA 0012 airfoil is shown to stall by the mechanism of abrupt turbulent leading-edge separation. A detailed step-by-step analysis of the events leading to dynamic stall, and of the results of the stall process, is presented for each of these three types of stall. Techniques for flow analysis in the dynamic stall environment are discussed. A method is presented that reduces most of the oscillating airfoil normal force and pitching-moment data to a single curve, independent of frequency or Reynolds number.

17. Key Words (Suggested by Author(s)) Aerodynamics Dynamic stall Unsteady turbulent boundary layers Unsteady separation	18. Distribution Statement Unlimited STAR Cat 02		
19. Security Classif. (of this report) Unclassified	20. Security Classif. (of this page) Unclassified	21. No. of Pages 105	22. Price* $5.25

TABLE OF CONTENTS

SYMBOLS

A	area of airfoil, m^2
$B.L.$	boundary layer
$B1$	leading-edge modification; serrations mounted at leading edge based on static tests
$B20BR$	leading-edge modification; serrations mounted at leading edge, bent to local contour, with serrations pointing upstream
$B4$	leading-edge modification; strip with no serrations, mounted at leading edge
C_M	pitching-moment coefficient, M/qA, nondimensional
$C_{M_{max}}$	maximum *negative* pitching-moment coefficient, nondimensional
C_{M_O}	pitching-moment coefficient measured at $\alpha = 6°$, nondimensional
C_N	normal-force coefficient, N/qA, nondimensional
$C_{N_{max}}$	maximum positive normal-force coefficient, nondimensional
C_{N_O}	normal-force coefficient measured at $\alpha = 6°$, nondimensional
$C_{p_{max}}$	maximum static-pressure coefficient, P/q, nondimensional
c	chord of airfoil, m
I	hot-wire flow-reversal type: sudden drop in signal
II	hot-wire flow-reversal type: gradual drop in signal to distinct minimum
III	hot-wire flow-reversal type: based on first fluctuation of signal to zero volts
IV	hot-wire flow-reversal type: subjective determination of change in signal indicating flow reversal or separation
k	reduced frequency, $\omega c/2U_\infty$
$L.E.$	leading edge of airfoil
M	pitching moment, N-m
N	normal force, N
p	static pressure on airfoil, N/m^2

q	dynamic pressure, N/m^2
Re	Reynolds number, $U_\infty c / \nu$
r_0	leading-edge radius, m
s	distance measured on surface of airfoil, m
t	time, sec
U_∞	free-stream velocity, m/sec
u'	fluctuating velocity, m/sec
x	distance measured along chord of airfoil, m
Y	nondimensional airfoil thickness (y/c) at $x/c = 0.0125$
y	distance measured normal to surface of airfoil, m
α	angle-of-incidence, deg
α_0	mean angle-of-incidence, deg
α_1	oscillatory amplitude, deg
α_{max}	maximum angle-of-incidence for given α schedule, deg
α_{min}	minimum angle-of-incidence for given α schedule, deg
$\Delta\alpha$	oscillation amplitude, deg
θ	angle of vane ahead of model, deg
ν	kinematic viscosity, m^2/sec
ω	rotational frequency, rad/sec

ANALYSIS OF THE DEVELOPMENT OF DYNAMIC STALL

BASED ON OSCILLATING AIRFOIL EXPERIMENTS

Lawrence W. Carr, Kenneth W, McAlister, and William J. McCroskey

Ames Research Center
and
Ames Directorate
U.S. Army Air Mobility R&D Laboratory

SUMMARY

The effects of dynamic stall on airfoils oscillating in pitch were
investigated by experimentally determining the viscous and inviscid character-
istics of the airflow on the NACA 0012 airfoil and on several leading-edge
modifications for a wide range of frequencies, Reynolds numbers, and
amplitudes-of-oscillation. A multiplicity of measuring techniques was incor-
porated to more fully delineate the airfoil response, including smoke-flow
visualization, hot-wire probes, and surface-pressure transducers. Analysis
and cross-correlation of these various inputs resulted in a new understanding
of the flow environment on an oscillating airfoil, and, in particular, the rela-
tionship between boundary-layer behavior and normal-force and pitching-moment
behavior. Three distinct types of separation development were observed within
the boundary layer, each leading to classical dynamic stall. Flow reversal
was universally observed prior to any detectable normal-force or pitching-
moment deviation from unstalled behavior, and in several instances, the flow
at the surface had reversed over a major portion of the airfoil before varia-
tions in integral force data were observed.

The major features of dynamic stall were qualitatively the same whether
the boundary layer gradually reversed from the trailing edge, or abruptly
broke down due to either laminar bubble-bursting or turbulent separation near
the leading edge. In all cases, a vortex was formed at the leading edge which
moved down the airfoil to produce large values of normal force and pitching
moment. A detailed step-by-step analysis of the events leading to dynamic
stall, and the results of the stall process are presented for each of these
three types of stall.

An important result of this study was the fact that although the normal-
force and pitching-moment curves were quite varied when plotted as functions
of angle-of-incidence, a properly scaled cross-plot of normal force versus
pitching moment resulted in a single representative curve for each airfoil,
provided the vortex had fully developed. This introduces the possibility of a
method that may allow prediction of engineering parameters without exhaustive
dynamic testing of airfoils.

Insights into the relative importance of leading-edge modifications,
reduced-frequency and amplitude variations, and Reynolds number changes are

presented. Finally, suggestions are made for future theoretical studies that offer the possibility for practical extension of aerodynamic modeling techniques to the dynamic stall problem.

INTRODUCTION

Dynamic stall is a phenomenon associated with an airfoil moving beyond its static stall angle while experiencing a rapid change in angle of attack. In steady flow, the angle of stall is essentially fixed for any given airfoil geometry; at most, it is a weak function of Reynolds number. However, when an airfoil is moved rapidly through an angle-of-attack range that includes the static stall angle, the angle of maximum lift can be greatly increased, and becomes strongly dependent on the rate and amplitude of oscillation. This dynamic overshoot of the static stall angle occurs with no detectable change in the loading trend until a strong vortex appears near the airfoil leading edge. The pitching moment is then radically altered (fig. 1), beginning with a large negative pitching moment which occurs as the vortex moves over the airfoil; when the vortex leaves the airfoil, the lift abruptly drops. The flow over the airfoil then becomes quiescent for a portion of the oscillation cycle, with a fully developed separated wake region appearing. Flow separation will usually persist for the remainder of the cycle, thus causing large hysteresis loops to develop in both the lift and pitching moment curves when viewed as a function of angle of attack.

The fact that the motion of an airfoil affects its stall behavior has been known for many years; the early work was primarily related to aeroelastic effects on aircraft wings (ref. 1), where small amplitude, high frequency oscillations were investigated. Dynamic stall was also found to be important in the design of jet engine compressors where larger amplitude variations were studied. The first analysis of the dynamic stall effects on helicopter rotor blades appeared in an experimental study in 1960 (ref. 2). Empirical techniques were developed (refs. 2, 3) that attempted to represent the primary effects of dynamic stall on airfoil lift and pitching-moment characteristics. Parametric experiments were run to expand the data base used for improving these empirical methods (refs. 4-6). The experiments were primarily directed toward obtaining aerodynamic force and moment coefficients as functions of frequency and angle, and the empirical corrections which developed from these tests were the prime source for improving helicopter aerodynamic prediction methods. The first investigation which attempted to isolate the fluid dynamic phenomena causing dynamic stall led to a correlation between experimental pressure distributions and the movement of a strong vortex along the surface of the airfoil (refs. 7, 8). Later research (ref. 9) verified visually that the vortex was directly associated with the radically changing pressure distribution on the oscillating airfoil. Flow visualization in water tunnel tests (ref. 10) also substantiated the presence of this vortex. The present series of experiments has been directed toward detailed examination of the viscous and inviscid events that combine to produce the phenomenon known as dynamic stall. Attention was focused on obtaining specific information about the fluid mechanics associated with the dynamic stall delay, as well as the dynamic stall itself.

2

In order to better understand the flow phenomena that will be discussed, a review of the aerodynamic terms to be used is of value. "Moment stall" is defined here as that point where the pressure distribution is altered sufficiently to produce a noticeable negative divergence in the pitching moment. This event is initiated by the rearward movement of the vortex that has formed near the leading edge; it is usually accompanied by a continued increase in lift. This is not the case in steady flow, where lift stall and moment stall occur simultaneously. "Lift stall" is defined as the condition where boundary-layer separation has occurred over enough of the airfoil to alter the pressure distribution such that no further lift can be obtained from further increases in angle of attack.

In steady flow, separation of a boundary layer is said to occur where the boundary-layer flow velocity near the surface is reduced to zero, and the flow detaches from the wall to form a wake that encloses a reversed-flow region (fig. 2). The separation and flow reversal points are coincident and the external stream is always distorted.

In unsteady flow, the location of the point of flow reversal and the point of flow separation are two distinctly different points. For example, theoretical studies of laminar flows have shown that the boundary-layer equations have a singularity at the point of flow reversal in steady flow (ref. 11), but that in unsteady flow, the location of the singularity associated with separation is distinctly different from the location of flow reversal (ref. 12). Thus, there can exist an unsteady boundary layer that has a region of reversed flow near the surface, while not showing any strong variations in the boundary-layer displacement or momentum thickness and little or no distortion of the external stream (fig. 3). This distinction between flow reversal and separation has also been demonstrated for unsteady turbulent boundary-layer flows (refs. 13, 16).

There were several types of separation observed in the present study of dynamic stall. Again, a review of steady flow counterparts will help in the later analysis of these unsteady flow conditions. In steady flow, depending on the type of separation that occurs, either an abrupt or a mild stall can result. Essentially, classical boundary-layer separation can appear in several ways. One type, leading-edge separation, occurs when the laminar boundary layer enters an adverse pressure gradient and locally separates before transition can occur. After this initial separation, the external flow can either completely diverge from the airfoil, causing an abrupt airfoil stall known as "leading-edge stall," or the separation can be followed by transition of the diverted flow to turbulent flow. Depending on the Reynolds number, one of several events can then occur: (1) the flow can quickly reattach itself to the airfoil as a turbulent boundary layer, enclosing a small bubble of separated flow (known as a laminar separation bubble) and then separate near the rear of the airfoil, causing "trailing-edge stall;" (2) the reattachment can be progressively delayed until the bubble grows to the full length of the airfoil, causing a stall known as "thin-airfoil stall;" or (3) the laminar separation bubble can remain small, but the turbulent flow over the bubble can reach a condition where the reattachment is no longer possible, causing a breakdown of the bubble, and producing "leading-edge bubble-bursting stall." Both

3

trailing-edge and thin-airfoil stall result in a gradual decay in lift compared with leading-edge or bubble-bursting stall, and the viscous flow must, therefore, be examined closely to verify which type of stall is occurring on a particular airfoil.

As indicated earlier, most studies of dynamic stall were aimed at obtaining airfoil section characteristics in unsteady flows. Since many of the experiments were performed at conditions where laminar separation bubbles were present (due to leading-edge separation), several studies were performed which linked leading-edge bubble bursting with the observed stall behavior (refs. 14, 15). More recently, the possibility was suggested that the unsteady turbulent boundary layer over the aft portion of the airfoil could be the cause of stall delay (ref. 16). The present test program was designed, in part, to determine the relative importance of the laminar bubble compared to the unsteady turbulent boundary layer as the primary cause of dynamic stall.

This paper presents a systematic analysis and discussion of the events that comprise dynamic stall, offers a step-by-step overview of the dynamic stall process as determined by several diagnostic tools, and correlates three basic separation mechanisms that were observed to cause dynamic stall.

Techniques found useful for experimental unsteady flow analysis are discussed, including a new nondimensionalization for correlating dynamic stall conditions. Insights into the relative importance of leading-edge modifications, reduced frequency and amplitude variations, and Reynolds number changes are presented.

DESCRIPTION OF EXPERIMENT

A major goal of this test was the determination of the relative importance of the leading-edge separation bubble vis-a-vis trailing-edge boundary-layer separation in the development of dynamic stall on an oscillating airfoil. Therefore, leading-edge shapes were chosen that would create clearly defined examples of these two classical stall types. According to Gault (ref. 17), whether or not leading-edge stall will occur on an airfoil is dependent on the radius measured at a specified percent of chord. Therefore, leading-edge shapes with differing leading-edge radii were selected to bracket the leading-edge geometry considered important to leading-edge separation-bubble formation. In particular, a "reduced leading-edge airfoil," having $r_o/c = 0.010$, and a "sharp leading-edge airfoil" with $r_o/c = 0.004$ (fig. 4) were tested in addition to the NACA 0012 airfoil. In contrast, a cambered airfoil that promotes trailing-edge separation was selected, the ONERA "0012 à Extension Cambre," which was developed in France for possible helicopter applications (fig. 4). These airfoil modifications were then tested for a range of Reynolds numbers, reduced frequencies, and amplitudes chosen so that dynamic conditions associated with the helicopter environment could be parametrically represented. The reference condition chosen was $\alpha = 15° + 10° \sin \omega t$, $k = 0.15$, and $Re = 2.5 \times 10^6$. Each airfoil was studied to determine the type of static stall that occurred and to evaluate the effects of pitching motion on the stall behavior.

4

A second goal of the experiment was to accurately determine the gross potential flow distortions that occurred during the stall process, and the details of the boundary-layer behavior, both during the stall delay and during the stall itself. For visualization of the gross distortions, smoke was introduced at several chordwise locations along the airfoil. To determine the boundary-layer response near the surface, hot-wire anemometer probes were placed at strategic locations along the chord. The location of the smoke ports, and the hot-wire anemometer probes are shown in figure 5.

The general characteristics of the various airfoil geometries were compared on the basis of smoke visualization and hot-wire probe outputs. Further comparisons were based on integral normal-force and pitching-moment characteristics obtained for each model tested. The upper and lower surfaces of each airfoil were instrumented with high response pressure transducers; the output signals were channeled to summing circuits (ref. 18) to obtain on-line output of normal force and pitching moment, and were stored on analog tape for later detailed digital analysis. Table 1 indicates all the test conditions and configurations that were studied during the qualitative portion of the wind-tunnel test, with annotations indicating those conditions for which force measurements, hot-wire measurements, or smoke-flow visualization movies were recorded. The shaded portions of this table represent the cases presented in this report.

Local free-stream velocity, dynamic pressure, turbulence intensity and flow angularity were measured ahead of the model (figs. 6, 11) to aid in determining tunnel interference. Tunnel wall corrections were not applied to the data, since it was determined that for the dynamic cases of interest the wall effects were not significant and that the test was essentially two-dimensional (details are presented in appendix A, "Analysis of Tunnel Interference Effects.")

Model Construction

The basic structure was a 1.22 m (4 ft) chord, 1.98 m (6.5 ft) span airfoil mounted vertically in the AMRDL-Ames 7- by 10-Foot Subsonic Wind Tunnel (fig. 6). The primary loads were carried by a 10 cm diameter tubular spar supported at the floor by a pivot bearing and at the top by a sleeve bearing. The NACA 0012 contour was used as a structural base; the modifications that were evaluated were effected by installing leading-edge caps on the basic NACA 0012 airfoil. The upper and lower surfaces of the instrumented mid-span section of the airfoil were removable so that instrumentation could be installed and modified.

Model Drive Mechanism

The model was sinusoidally oscillated in pitch by a crank, connecting-rod and flywheel mechanism (fig. 7). The mean angle of oscillation was varied by changing the length of the connecting rod; the oscillation amplitude was varied by attaching the rod at specific radial locations on the flywheel. High-frequency oscillations (0.15 to 2.0 Hz) were obtained using a compressed

air motor, while low-frequency oscillations (0.017 to 0.15 Hz) were obtained using a belt and pulley system attached to a variable-speed motor.

Pressure Transducers

All pressure transducers were differential, had a nominal flat frequency response of 250 Hz, and were referenced to tunnel total pressure. These transducers were installed in containers mounted on the inner surface of the removable panels (figs. 8, 9) so that tubing on the measurement side could be minimized. The pressure transducer gains were adjusted to provide equal response characteristics as required for input to the on-line normal-force and pitching-moment summing circuits, but quantitative calibration of the output was not performed. Therefore, all normal-force and pitching-moment data are presented without quantified scaling; instead, the data are referenced to the NACA 0012 for comparison.

Hot-Wire Anemometer Probes

Miniaturized hot-wire anemometer probes were installed on the airfoil upper surface at chordwise locations shown in figure 5. These probes were conventional two-prong, single-element probes that projected vertically from the surface of the model. The probe at $x/c = 0.05$ was 0.128 cm (0.050 in) above the airfoil; the probes at $x/c = 0.20$, 0.30, 0.45, 0.70, and 0.90 were all 0.064 cm (0.25 in) above the airfoil. The flow at the edge of the boundary layer was obtained by mounting long-stemmed probes at heights which would ensure a free-stream exposure during the unstalled portion of the cycle, and were located at $x/c = 0.013$, 0.05, 0.10, 0.20, 0.45, 0.60, and 0.90. All the hot-wire probe outputs were linearized and had a frequency response of 5000 Hz.

Smoke-Flow Visualization

Previous oscillating airfoil tests using smoke emitted from the leading edge and trailing edge as a flow visualization tool (ref. 9) had shown that smoke was very valuable for delineating the boundaries of the viscous region both before and after the stall occurred. Smoke was particularly useful for visualizing the formation and development of the vortex associated with dynamic stall. For this test, smoke ports were installed at $x/c = 0.0$, 0.20, 0.40, 0.70, and 0.90. The smoke was generated by pumping oil through resistance heated tubes. The smoke was passed through a plenum chamber where oil droplets were allowed to settle (fig. 7), and then piped to the smoke ports in the model. The smoke ports were supplied simultaneously except for a separate line to the leading edge. In order to minimize potential flow interactions due to the jets of smoke, the pressure applied to the smoke plenum was regulated for each flow condition so that the flow issuing from the smoke ports was just sufficient to permit visualization of the flow throughout the cycle. There is a possibility that the smoke flow from the leading edge may have caused some local disturbance to the boundary layer, since a small bulge near the leading edge was sometimes visible in the smoke. However, the smoke-flow

6

visualization correlates well with the hot-wire probe and pressure-transducer outputs, and these were both obtained with the smoke ports closed. The bulging that was observed is, therefore, considered to be of a local nature and not contributory to the later flow development. Since the smoke was injected at the leading edge as well as at other locations on the airfoil, the smoke exposes the complete boundary-layer thickness rather than only a diffusion layer submerged inside the actual aerodynamic boundary layer.

Photography of Smoke Flow

The smoke-flow visualization was recorded using high-speed cameras (250 frames/sec) located at two vantage points. One camera was mounted on an extension of the model support spar and rotated with the model (fig. 10); the second camera was fixed to the tunnel. The airfoil was illuminated from the front and rear using quartz and xenon lamps (fig. 11). The ground plane within the view of the cameras was covered with black velvet cloth to reduce reflection and increase contrast.

Analog Data Recorded

Time histories of normal force and pitching moment for 10 or more cycles of oscillation were recorded on a 14-channel analog tape recorder for each of the conditions studied. In addition, the following signals were recorded: (1) a 200/rev timing mark (modulated by a 1/rev dc step) generated by an optical system attached to the rotating flywheel of the drive mechanism; (2) a reference time code (generated electronically) for later identification of run and frame number; (3) tunnel dynamic pressure obtained from a pitot-static probe ahead of the model; (4) incidence of the airfoil obtained from a potentiometer keyed to the shaft supporting the model; (5) airfoil surface pressures located at x/c = 0.05 and 0.90; and (6) flow-reversal indications obtained from hot-wire anemometer probes located at x/c = 0.05, 0.20, 0.30, 0.45, 0.70, and 0.90.

On-Line Displays

The instantaneous values of normal force, pitching moment, dynamic pressure, and angle-of-incidence were channeled to a dual-beam oscilloscope. The normal force and pitching moments were nondimensionalized using the following technique: at each Reynolds number, the y-gain of the oscilloscope was adjusted so that the dynamic pressure always produced the same deflection. The x-beam of the oscilloscope was controlled by the instantaneous angle of incidence. When instantaneous normal-force or pitching-moment signals were supplied to the y-beam of the oscilloscope, C_N and C_M vs α curves (fig. 12) were produced (the normal force and pitching moment were automatically divided by the average q since the y-gain was set using q as the scaling factor). When combined with oscillograph records of the pertinent pressure, hot-wire, force, and moment outputs, the on-line C_N and C_M vs α plots offered a data analysis capability that proved very valuable in evaluating the various airfoil modifications that were studied.

TECHNIQUES FOR DYNAMIC STALL ANALYSIS

In order to properly analyze the dynamic stall process, flow visualization by smoke flow and yarn tufts, and boundary-layer measurements by hot-wire anemometry were obtained in addition to the traditional force and moment measurements. The smoke flow showed the overall flow-field characteristics, the tufts gave qualitative flow-reversal information, and the hot-wire data showed boundary-layer detail near the wall. These inputs were vitally important for proper interpretation of the force and moment data; without them the data could easily have been misinterpreted and many stall events would not have been documented. To better appreciate the information offered by these various diagnostic tools, their characteristics and application in the present test will now be discussed. These results will later be combined with the force and moment data to fully disclose the characteristics of dynamic stall.

Flow Visualization Analysis

The photographs obtained in the moving frame of reference proved more valuable and provided most of the data presented here. The film was studied frame-by-frame, to obtain quantitative measurements of the location, size, and movement of the vortex, as well as flow reversal at smoke-port and tuft locations. It must be emphasized that interpretation of boundary-layer development by analysis of smoke-flow visualization is a subjective task. It requires repeated frame-by-frame viewing of the high-speed films, using a stop-action projector to establish an ordered description of the flow events. Some of the more distinctive smoke-flow patterns are presented below.

Boundary-layer distortion (smoke): As the airfoil incidence was increased, the boundary layer as exposed by the smoke would grow. At a given angle, dependent on the airfoil being tested, a gross distortion or sudden growth of the local boundary-layer thickness would occur, causing a discernible change in the outer boundary of the smoke flow on the model.

Flow reversal (smoke): The overall smoke in the boundary layer generally obscured the local behavior upon exiting from the smoke ports. However, once the boundary layer lifted from surface, the smoke flow at each port could be observed and reversal of the smoke flow at the port could be determined. The most distinguishable characteristic of the smoke at the port was a complete change in flow direction. The only exception was during trailing-edge stall when a thick and slowly growing boundary layer afforded ample time to observe a more gradual reversal of the $x/c = 0.90$ smoke-port flow.

Flow reversal (tufts): As a complement to the smoke-flow visualization, tufts were attached at five chordwise stations ($x/c = 0.10, 0.30, 0.50, 0.75,$ and 0.90). These tufts revealed the behavior of the flow near the surface at each tuft location, thereby providing a separate set of indicators about activities within the boundary layer. This information was in clear contrast to the more global view presented by the smoke and was particularly important for determining leading-edge stall. The tufts also showed a more varied range of response to changes in the boundary layer.

8

The terms "tuft flutter" and "tuft reversal" are best defined within the context of the following typical chronological sequence of events: (1) *Fully attached*: tufts are quietly pointing in the downstream flow direction. Turbulent eddies may sporadically cause small motions, but no significant movement is apparent. (2) *Tuft flutter*: tufts show some degree of flapping but are still pointing downstream on the average. (3) *Tuft reversal*: the first time a tuft fully reversed, regardless of subsequent behavior such as flipping or swirling.

Flow Visualization Applications

Flow visualization was very helpful in determining the overall characteristics of the various stall types that were studied. The following sections show how each of the airfoils produced differing flow effects, and how the smoke made these differences clear.

Trailing-edge stall - cambered airfoil- The most easily understood dynamic stall occurred on the cambered airfoil, where stall developed as a relatively gradual forward progression of flow reversal from the trailing edge of the airfoil. It will be seen that actual separation of the boundary layer did not occur at the point of flow reversal, and that the external flow was not seriously distorted until the vortex formed.

Smoke: The smoke flow that occurred during this type of stall is shown in figure 13; in figure 13(a) a distortion of the boundary layer has occurred over most of the airfoil. Figure 13(b) shows a series of large scale eddies characteristic of all the airfoils just prior to penetration of flow reversal to the leading edge (note that the potential flow is not significantly altered); figure 13(c) shows the smoke boundary at the instant that flow reversal has reached the leading edge; figure 13(d) shows the fully developed vortex, as first detected in the film (on the cambered airfoil, this vortex was fairly diffused); and figures 13(e) and 13(f) show boundary-layer reattachment over the first 25 percent and 50 percent of chord, respectively.

Tufts: Figure 14 shows tuft and smoke-flow behavior for static and dynamic conditions on the cambered airfoil. The boundary-layer distortion as outlined by the smoke shows a steady progression forward from the trailing edge for all cases. Tuft flutter, tuft reversal and smoke-flow reversal at the smoke ports agree closely at $k = 0.05$. However, for $k = 0.15$ and 0.25, the agreement is less exact; this probably is due to the diffused nature of the shed vortex. Note that flow reversal occurred well before boundary-layer separation developed (the separation of the boundary layer occurred when the flow reversal reached the leading edge).

Leading-edge bubble-bursting stall - sharp leading-edge airfoil- As mentioned earlier, there are several types of boundary-layer characteristics associated with leading-edge stall. The type most often cited in the literature as being the cause of dynamic stall is leading-edge bubble bursting. In order to distinguish this type from leading-edge stall where no bubble is present, static oil-flow pictures were taken of the sharp leading-edge airfoil.

These photographs showed a definite bubble near the leading edge for static conditions (fig. 15). Also, the pressure traces near the leading edge show the presence of the bubble during the dynamic conditions.

Smoke: Leading-edge bubble-bursting stall as observed in the smoke-flow visualization is in distinct contrast to the trailing-edge stall described earlier. The leading-edge bubble-bursting stall was characterized by conditions where the entire boundary layer outlined by smoke appeared to suddenly lift off the surface as if pivoted about the leading edge; hot-wire data shows that the boundary layer actually first separates from the surface near the leading edge. Figure 16(a) shows the thickening of the boundary layer over the whole airfoil just prior to stall; figure 16(b) shows the characteristic appearance of large scale eddies just prior to stall; figure 16(c) shows the flow at the time when separation of the boundary layer has started at the leading edge and a separated zone has developed on the airfoil; figure 16(d) shows the fully developed vortex as first detected on the film (note that the vortex is much more tightly coiled, and is further forward on the airfoil than that associated with trailing-edge stall); and figures 16(e) and 16(f) show boundary-layer reattachment over the first 25 percent and 50 percent of chord, respectively. Comparison of figures 13 and 16 graphically substantiates the fundamental difference in the stall development between trailing-edge, and leading-edge bubble-bursting stall.

Tufts: For this airfoil, figure 17 shows that at $k = 0.05$ the boundary layer appears to separate from the surface simultaneously over the whole airfoil, as detected by smoke, tuft motion, and smoke-flow reversal at the smoke ports. As the frequency is increased, these events become more obviously initiated at the leading edge. For $k = 0.15$ and 0.25, the trend is clearly observable in tuft flutter, tuft reversal, and flow reversal at the smoke ports.

The boundary layer as outlined by smoke shows essentially simultaneous lift off at all x-stations, a factor discussed earlier. Note that as the reduced frequency is increased, the initial location of vortex detection moves from approximately $x/c = 0.40$ to $x/c = 0.10$. Movie films of this airfoil showed a corresponding tightening and strengthening of this vortex with increasing frequency.

A second leading-edge-separation stall type was created by testing the cambered airfoil at negative incidence. This resulted in a definite leading-edge stall behavior, as detected by tufts (fig. 18). Here, very abrupt flow reversal occurs at the leading edge of the airfoil causing a separation which then progresses down the airfoil with time. Unfortunately, no smoke-flow visualization or hot-wire data were obtainable because this surface of the airfoil was not equipped with the necessary instrumentation.

NACA 0012 airfoil- The present experiment has shown the NACA 0012 to have the most complex stalling behavior of all of the airfoils studied. Analysis of the clearly defined behavior of trailing-edge separation and leading-edge bubble bursting is a necessary prerequisite for analysis of the NACA 0012 behavior. Since all the experimental diagnostic tools are necessary, only a

10

partial picture can be obtained from flow visualization. However, flow visualization illustrates the magnitude of the problem.

1. Smoke. Figure 19(a) shows the flow when the smoke boundary layer indicates distortion on the rear half of the airfoil; figure 19(b) shows the characteristic large-eddy motion; figure 19(c) shows an almost simultaneous change in boundary-layer thickness over the first 30 percent of the airfoil (note that the boundary layer has not actually left the surface); figure 19(d) shows the presence of a vortex (the leading-edge flow is now fully detached); and figures 19(e) and 19(f) show the boundary-layer reattachment over the first 25 percent and 50 percent of the chord, respectively. It is not clear from these photographs exactly what kind of stall has occurred; it will be shown later that this is quite proper, since the NACA 0012 has a mixed form of trailing-edge separation and turbulent leading-edge separation.

2. Tufts. Figure 20 shows that for the NACA 0012, tuft reversal begins at the trailing edge and rapidly moves forward; at the higher frequencies the events occur almost simultaneously. At the higher frequencies this behavior could be considered as leading-edge stall. However, when compared to figure 17 it can be seen that there are significant differences in behavior: regardless of frequency, the vortex is not clearly definable until approximately 50 percent chord; the shedding of the vortex occurs significantly later in the cycle - both factors corresponding more to trailing-edge rather than to leading-edge stall behavior. More information is needed before a full understanding of this stall can be achieved.

It is clear that smoke-flow visualization was a very important diagnostic tool for substantiating the formation, extent, and movement of the leading-edge vortex. Smoke not only disclosed large-scale eddies within the turbulent boundary layer just prior to stall, but defined as well the viscous-inviscid boundary throughout the complete cycle. However, as has been shown on the NACA 0012, the information it supplies is of a global and subjective nature, and it did not supply critically needed information about the actual nature of the boundary layer on the airfoil itself.

Hot-Wire Anemometry Analysis

As discussed in the previous section, smoke-flow visualization requires subjective decisions to quantify the observations that are made of flow behavior. The hot-wire anemometer probes placed near the surface offset this weakness considerably. Analysis of these signals led to the precise determination of the events and processes occurring during dynamic stall.

Several different types of boundary-layer instrumentation were tested to evaluate their effectiveness for determining the nature of the boundary-layer separation leading to dynamic stall. These included single and dual-element heated-film skin-friction gages; special dual-hot-wire probes that were designed to detect changes in flow direction; miniature pitot-static pressure tubes facing both upstream and downstream; and arrays of conventional hot-wire anemometer probes. From this exploratory study, it was concluded that the linearized response of conventional hot-wire probes would be most effective

for determining the onset of boundary-layer flow reversal, separation, and the passage of the vortex over the upper surface of the model. The outputs of these hot-wire probes were recorded on analog tape, and several cycles of analog data for each case were then analyzed.

Representative oscillograph traces of single hot-wire anemometer probe outputs are shown in figure 21(a); corresponding pressure traces are in figure 21(b), the instantaneous velocities across the boundary layer are in figure 21(c), and at the edge of the boundary layer are in figure 21(d). It should be mentioned that a single-wire probe cannot be used to distinguish directly between forward or reverse flow, because the response never becomes negative. Instead, a cusp is formed at the minimum velocity as the flow direction in the boundary layer changes sign. Also, in a turbulent boundary layer, random fluctuations preclude the local average of the fluctuating signal from going to zero, thus complicating the interpretation of the measurements. Nevertheless, certain boundary-layer behavior could normally be inferred from the response of the wires. For example, near the leading edge, a sudden drop in the hot-wire signal for $x/c = 0.05$ (at the point marked "I" in fig. 21(a)) indicates an abrupt breakdown of the flow, and this signal is labeled Type I in subsequent figures and discussion. The Type II signal at $x/c = 0.45$ drops to a distinct minimum value as the flow reverses, although the flow breakdown appears much less abrupt than for Type I. Near the trailing edge, the approach to reversed flow is much more gradual, and a distinct instant of flow reversal is more difficult to ascertain in the presence of the random turbulent fluctuations. This case, Type III, was defined on the basis of the first fluctuation to reach zero, similar to the "intermittent turbulent separation" definition of reference 19 for nominally steady flows. It seems to precede true flow reversal in any average sense, but at least it can be used to define the earliest indication of a major boundary-layer event connected with flow reversal or separation.

Flow reversal, as well as the other dynamic stall events, was observed to vary somewhat from cycle to cycle, so the hot-wire data presented herein have been averaged over a number of cycles. For the basic NACA 0012 airfoil, the standard deviations in the values of ωt for flow reversal varied from about ±0.17 rad at $x/c = 0.90$ to about ±0.05 rad at $x/c = 0.05$ (fig. 22). The repeatability of the reversal point predictions can also be observed in this figure, where the test conditions were duplicated in two separate runs. In some cases, large irregular fluctuations such as in the second cycle in figure 21(a) at $x/c = 0.20$, or major variations from one cycle to the next, made it difficult to define flow reversal precisely or even to define a specific category of signal. However, close examination of the time history would usually reveal some fairly distinct change in the character of the signal that seemed symptomatic of either flow reversal or boundary-layer separation; these types of signals were called Type IV. Construction of velocity profiles from the hot-wire records that were obtained during the latter phase of this test at 10 or more y positions in the boundary layer should resolve these data better.

The hot-wire anemometer results are a definitive indicator of stall behavior, at least as it can be detected by analysis of flow near the airfoil surface. The first reversal of the boundary-layer flow occurs near the

12

surface; hot-wire probes further out in the boundary layer do not show flow reversal until a later time (fig. 21(c)). Flow reversal near the surface was always found to precede the pressure disturbances that accompanied boundary-layer separation, and to occur well before any measurable change in normal force or moment could be detected (fig. 23). It should be noted that the probe output for $x/c = 0.90$ was almost always the first to show flow reversal, even for the leading-edge stall airfoil. In this case, it responded long before the effects of the flow reversal that occurred at the leading edge had reached the trailing edge. However, the boundary layer at $x/c = 0.90$ was very thick (in some cases as much as 10 cm) and the flow in that region often showed almost quiescent mean behavior.

Hot-Wire Anemometry Application

The output of the hot-wire anemometer probes proved to be the most sensitive indicator of flow reversal, and was, therefore, used as the primary diagnostic tool for determining stall type; for the NACA 0012 they became the decisive tool for analysis.

Trailing-edge stall - cambered airfoil- Throughout the parametric range studied, flow reversal, as determined by hot-wire signals (fig. 24), shows a definite progression up the airfoil as the angle of attack is increased. The onset of flow reversal occurs at an angle that increases with increasing reduced frequency, k. A sharp break or distinct minimum in hot-wire signals at flow reversal seems to be characteristic for wires located ahead of the vortex for any given case. It is, therefore, significant that Type I and Type II reversals are detected as far aft as $x/c = 0.50$ on the airfoil, since the smoke-flow visualization for this airfoil shows that the vortex develops at about 40-50 percent chord (fig. 13). The Type III reversal over the rear of the airfoil is consistent with the diffused form of the vortex as detected in the smoke.

The boundary layer at the leading edge did not always completely reverse or separate, especially for $k \geq 0.15$, and the value of ωt corresponding to the sharp changes at $x/c = 0.50$ varied from cycle to cycle. Otherwise, the data were all within the standard deviations obtained for the experiment in general.

Leading-edge bubble-bursting stall - sharp leading-edge airfoil- For the sharp leading-edge modification, the first sign of flow reversal is definitely near the leading edge as detected by the leading-edge pressure transducer and by hot-film sensors placed on the surface (fig. 25). The region of reversed flow progressed downstream to about $x/c = 0.70$ before encountering the flow affected by the trailing edge, which showed flow reversal early in the cycle. As the frequency was increased, the progression of flow reversal from front to rear became even more pronounced, clearly supporting smoke-flow visualization results. Note that for this airfoil, no Type I flow was observed for any location or condition. This is attributable to the fact that separation first occurred near the leading edge. Thus, the hot-wire probes downstream of the leading edge responded to flow separation rather than flow reversal and a less abrupt velocity break resulted.

13

Turbulent leading-edge stall - NACA 0012 airfoil- It is now that the true
character of the NACA 0012 can be observed. The hot-wire signals show that
the NACA 0012 first experiences trailing-edge separation at all the frequen-
cies studied (fig. 26). This trailing-edge separation appears as a flow
reversal progressing from the trailing edge up to about 40 percent chord. At
this point, flow reversal progresses to the leading edge almost instantane-
ously. Close study of figure 21(a) shows that turbulent flow has been well
established as far forward as $x/c = 0.05$, long before flow reversal begins.
The hot wire traces for $x/c = 0.05$, 0.20, and 0.45 show almost simultaneous
reversal (fig. 26). Thus, flow reversal has occurred in an attached, fully-
turbulent boundary layer. When compared to leading-edge bubble-bursting stall
(fig. 25) it can be seen that, at the higher reduced frequencies, the NACA
0012 separation is not starting from the leading-edge - it is truly due to an
abrupt turbulent separation, possibly starting at midchord. The flow rever-
sals at $x/c = 0.05$ and 0.10 are Type I; there is a sudden drop in velocity
over the whole front section of the airfoil and smoke-flow visualization shows
the flow finally detaching from the leading-edge. All of these are indicative
of a modified form of leading-edge stall. Thus, the final stage of dynamic
stall on the NACA 0012 airfoil is caused by an abrupt *turbulent leading-edge
separation, a new form of leading-edge stall.*

ANALYSIS OF DYNAMIC STALL EVENTS

Process of Dynamic Stall - The Sequence on the NACA 0012

The events associated with dynamic stall were made clear by a combination
of flow visualization, hot-wire anemometry and normal-force and pitching-
moment data obtained over a wide range of reduced frequencies, Reynolds num-
bers, mean incidence angles and oscillation amplitudes. Extensive
cross-correlations between these test conditions brought the principal events
into focus. As mentioned earlier, the NACA 0012 airfoil has the most complex
stall process of all airfoils tested. Since it is the airfoil most often used
for theoretical and experimental research programs, the greater part of the
present experiment was devoted to obtaining information about its character-
istics. For these reasons, the NACA 0012 is discussed first, followed by
discussions of leading- and trailing-edge stall.

The vortex shedding process is the most obvious characteristic of dynamic
stall, and much effort has been expended in the analysis of this event. How-
ever, by the time the vortex is affecting the pressure distribution, dynamic
stall, as such, has already begun. To better understand the stall delay pro-
cess itself, analysis must include conditions significantly before the point
at which symptoms appear in the normal force and pitching moment. Therefore,
a chronology of events for a full cycle of oscillation is now presented for
the NACA 0012 airfoil at the standard condition studied during this program
$(k = 0.15$, $Re = 2.5 \times 10^6$, $\alpha = 15° + 10° \sin \omega t)$. Each of the following
paragraphs corresponds to events identified in figure 27.

Static stall angle exceeded (fig. 27(a)): The airfoil passes the static-
stall angle without any detectable change in the flow over the airfoil. The

14

flow behaves as if the airfoil were below stall in the sense that the boundary layer remains thin with no evidence of flow reversal at the surface.

Flow reversal appears at surface (fig. 27(b)): When the airfoil incidence reaches 19°-20°, a distinct change in the boundary-layer flow occurs; Type III flow reversal (gradual decrease in velocity to zero) appears at the rearmost hot-wire probe location, and the boundary layer on the rear portion of the airfoil begins to thicken. The main portion of the boundary-layer remains thin and appears attached.

Large eddies appear in boundary layer (fig. 27(c)): The boundary layer as delineated by smoke-flow visualization shows a wavy pattern on the outer boundary. This is characteristic of the type of flow that would appear if large eddies were moving down the airfoil. Downstream of $x/c = 0.70$, the mean flow near the surface becomes virtually quiescent, leaving only random fluctuations due to local turbulence.

Flow reversal spreads over airfoil chord (fig. 27(d)): The hot-wire flow-reversal probes near the surface of the airfoil indicate that flow reversal progresses up the airfoil from the trailing edge to the vicinity of $x/c = 0.30$. This progression is observable in the hot-wire signals (fig. 21(a)), and in the surface pressure (fig. 21(b)). A region of highly disturbed boundary-layer flow is created, although no discernible change can be detected in the normal force or pitching moments of figure 27 up to the angle where 50 percent of the surface of the airfoil is experiencing reversed flow. The lower boundary of the flow visualization band in figure 28 is determined by boundary-layer distortions outlined by the smoke, while the upper boundary is defined by tuft reversal and smoke-flow reversal at the smoke ports.

Vortex forms (fig. 27(e)): At $\omega t \approx 0.32\pi$ ($\alpha = 23.4°$) the boundary-layer flow on the front of the airfoil abruptly breaks down, or "separates." As near as can be determined from the hot-wire and pressure data, this event occurs simultaneously from $x/c = 0.30$ to almost the leading edge (the boundary-layer flow for $0.0 < x/c < 0.005$ does not completely separate until slightly later). As this abrupt separation occurs, the suction at $x/c = 0.10$ begins to rise, indicating the initial formation of the vortex. Dynamic stall has begun. As this vortex begins to form and move downstream, the magnitude of the reverse flow near the surface of the model increases, and the pitching moment starts to deviate from static values. The solid symbols in figure 28 indicate negative-pressure peaks, measured by pressure transducers, and reverse-velocity peaks, measured by the hot-wire probes. The locus of these peaks indicates that the vortex is traveling at approximately 35-40 percent of the free-stream velocity.

Lift-curve slope increases (fig. 27(f)): The first effect of dynamic stall on the force and moment characteristics appears as a change in the slope of C_N vs α curve. The normal force changes in the opposite sense to what is normally encountered in steady-flow stall; that is, C_N begins to rise more rapidly with increasing incidence. This rate of increase greatly exceeds the value of $2\pi\alpha$ that is normally an upper limit to lift-curve slopes in quasi-static flows.

15

Moment stall begins (fig. 27(g)): The change in the pressure distribution on the airfoil associated with the vortex that occurs at the near-maximum incidence causes the aerodynamic pitching moment to change drastically. This is somewhat analogous to the changes in C_M that occurs in static stall, and has been called "moment stall" by Harris and Pruyn (ref. 3) and subsequent investigators.

Lift stall begins (fig. 27(h)): The increased lift-curve slope discussed above continues until maximum C_N is reached. (The vortex is now approximately at midchord.) C_N then decreases sharply.

Maximum negative moment occurs (fig. 27(i)): Negative $C_{M_{max}}$ occurs at $\omega t = 0.47\pi$ ($\alpha = 24.95°$). The vortex core passes off the trailing edge of the airfoil at $\omega t = 0.55\pi$ ($\alpha = 24.8°$ on the downstroke). The lift continues to drop, and the moment increases rapidly to values more representative of static stall.

Airfoil enters full stall (fig. 27(j)): After the dynamic-stall vortex has left the airfoil, the flow over the airfoil experiences some lower amplitude oscillations before settling down as a fully separated flow which is quite similar to the type of flow observed on airfoils experiencing steady-state stall.

At $\omega t \simeq 0.7\pi$ ($\alpha = 23.1°$ on downstroke), a second vortex-like disturbance begins to form somewhat ahead of midchord and then moves downstream, but this produces relatively small secondary peaks in C_N and C_M during this part of the downstroke. During this period and continuing until the final reattachment process starts at $\omega t = 0.95\pi$ ($\alpha = 16.5°$ on downstroke), flow visualization indicated that the flow in the vicinity of the leading edge alternately reattached and reseparated, although this was not generally evident from the hot-wire and pressure transducer signals. The rest of the airfoil is fully separated.

Boundary-layer flow reattachment (fig. 27(k)): The boundary-layer flow reattaches to the airfoil progressively from the leading edge. The reattachment line proceeds downstream at approximately 25-35 percent of free-stream velocity. Reattachment has occurred over the complete airfoil by $\omega t = 1.2\pi$ ($\alpha = 7°$ on downstroke).

Unstalled force and moment values re-established (fig. 27(l)): Although the flow has reattached to the airfoil surface during the downstroke (as shown by smoke-flow visualization), the rest of the potential flow does not appear to return to unstalled conditions until the airfoil has passed through its minimum angle. The lift and moment return to their respective unstalled values at about $\alpha = 6°$ on the upstroke; this is probably associated with the time it takes for the separated region to close, and for this disturbed region to move downstream.

Dynamic Stall on the Cambered Airfoil

In comparison to the abrupt turbulent leading-edge separation occurring on the NACA 0012 airfoil, the cambered airfoil displayed a much more easily

16

analyzed gradual trailing-edge turbulent separation. The C_N and C_M for the cambered airfoil at standard conditions are compared to that for the NACA 0012 airfoil in figure 29. Following the ordered presentation given in the previous section, the sequence of events occurring on the cambered airfoil are as follows:

Static stall angle exceeded: The boundary layer is again unaffected by the passage of the airfoil through the static-stall angle.

Flow reversal appears at surface: Flow reversal first appears at $x/c = 0.90$ for $\omega t = 0.06\pi$ ($\alpha \simeq 17°$ - two degrees less than that associated with the NACA 0012). The boundary layer remains thin and appears attached.

Large eddies appear in boundary layer: The airfoil boundary layer thickens near the trailing edge, a large eddy structure develops, and quiescent flow appears downstream of $x/c = 0.70$.

Flow reversal spreads over airfoil chord: Flow reversal progresses smoothly from the trailing edge (fig. 24) and corresponding smoke-flow and tuft reversal are observed (fig. 14). Note that for $k = 0.15$ no change is observed in C_N or C_M characteristics until reversed flow has reached $x/c = 0.20$ (fig. 24).

Vortex forms: At $\omega t \simeq 0.12\pi$ ($\alpha = 18.7°$) a vortex develops - the stall process has begun. The stall development is much different than that observed on the NACA 0012. The vortex on the cambered airfoil is diffused, and its effects are less severe, especially in regard to the maximum negative value of C_M (fig. 29). During some cycles the boundary layer near the leading edge did not completely reverse or separate even after the vortex formed. Even when the leading-edge flow did separate, the vortex was still first observed at a location significantly further downstream than that occurring on the NACA 0012.

Lift-curve slope increases; moment stall begins: The lift-curve slope starts to exceed 2π and moment stall begins almost simultaneously. These events occur when the flow reversal has reached the hot-wire probe at $x/c = 0.20$ and coincide with the formation of the dynamic-stall vortex.

Lift stall begins; maximum negative moment occurs: For this case, $C_{N_{max}}$ is reached at $\omega = \pi/2$, ($\alpha = \alpha_{max}$), with $C_{M_{max}}$ occurring almost immediately afterwards. The vortex passes over the airfoil at a much slower pace than for the NACA 0012 and leaves the trailing edge at $\omega t = 0.8\pi$ ($\alpha \simeq 21°$ on the downstroke). C_N and C_M again rapidly return to values representative of static stall.

Airfoil enters full stall: Fully separated flow again appears on the airfoil. A second vortex also forms, but it is weaker, and has no significant effect on C_M.

Boundary-layer flow reattachment; unstalled force and moment values re-established: Boundary-layer reattachment again seems to have occurred before minimum angle is reached. The C_N and C_M curves again do not show

values corresponding to attached potential flow until the airfoil has passed this minimum incidence and started the next upstroke.

In summary, the overall character of C_N and C_M versus α loops for the trailing-edge stall on the cambered airfoil are qualitatively similar to those of the NACA 0012. However, the flow reversal on the front of the airfoil and the stall inception (events d and e) are fundamentally different in origin and have significantly different effects on the vortex formation. Although flow reversal begins earlier, lift stall is delayed, and the maximum negative moment is significantly reduced.

Dynamic Stall on the Sharp Leading-Edge Airfoil

Two airfoil geometries showed distinct indications of stall due to the mechanism of leading-edge laminar bubble bursting: the sharp leading-edge modification with $r_o/c = 0.004$, and the cambered airfoil at negative incidence ($\alpha = -15° + 10°$ sin ωt). The presence of a rather elongated bubble on these airfoils was verified by oil visualization during static tests. Dynamic verification of bubble bursting was obtained by hot-wire signals on the sharp leading-edge airfoil (fig. 25) and by observation of tufts on the inverted cambered airfoil (fig. 18). C_N and C_M for the sharp leading-edge airfoil are compared to the NACA 0012 airfoil in figure 30. For the sharp leading-edge airfoil, the stall developed as follows (the events on the inverted airfoil are similar):

Static-stall angle exceeded: The static-stall angle was significantly reduced. The boundary-layer flow was not altered upon passing through this static-stall angle.

Flow reversal appears on surface: Flow reversal is first detected by the $x/c = 0.05$ hot-film gage (fig. 25), in sharp contrast to the previous airfoil stall types (it also appears at $x/c = 0.90$, but the flow reversal in this region is apparently of little consequence).

Large eddies appear in boundary layer: The boundary layer from $0.20 < x/c < 0.70$ remains attached but shows ripples characteristic of the large-eddy structure observed on the other airfoils.

Flow reversal spreads over airfoil chord; vortex forms: At the same time that a vortex is forming at the leading edge, the tuft at $x/c = 0.10$ has reversed, while all the other tufts point downstream. It is quite clear (fig. 25) that there is a front-to-rear progression of the breakdown of the boundary-layer flow, in marked contrast to all the results presented earlier. For this case, flow reversal occurs after the formation of the vortex, and follows the vortex down the airfoil, in keeping with the characteristics of leading-edge bubble bursting. Also, smoke-flow visualization shows that the boundary layer separates from the leading edge without flow reversal first appearing at the surface farther down the airfoil. Flow reversal, vortex formation, and C_M stall inception occur virtually simultaneously on this airfoil, and at a significantly lower angle of incidence.

18

Lift-curve slope increases; moment stall begins: Above 2π, $\partial C_N/\partial\alpha$ increases at $\omega t = 0.0$ ($\alpha = 15°$), and moment stall occurs simultaneously. Although this trend in $\partial C_N/\partial\alpha$ was observed on the airfoils discussed above, the form of the C_N loop is radically different (fig. 30).

Lift stall begins: $C_{N_{max}}$ occurs at $\omega t = 0.23\pi$ ($\alpha = 21.7°$) and then gradually decreases until maximum incidence is reached.

Maximum negative moment occurs: $C_{M_{max}}$ is attained at $\omega t = 0.27\pi$ ($\alpha = 22.5°$).

Airfoil enters full stall: Fully-separated flow appears on the airfoil. A secondary vortex is observed, but has little effect on the normal force.

Boundary-layer flow reattachment; unstalled force and moment values re-established: The reattachment process is similar to the previous cases, and C_N and C_M do not return to unstalled values until the airfoil is again on the upstroke.

In summary, leading-edge bubble-bursting stall is both qualitatively and quantitatively different from the stall types appearing on either the NACA 0012 or the cambered airfoil. The inception of stall is abrupt, the sequence of boundary-layer events is fundamentally altered, and the shape of the normal force loop is significantly changed.

Discussion of Stall Results

The previous sections have highlighted the significant effects associated with leading-edge bubble bursting, and trailing-edge stall stereotypes. It has also been shown that the NACA 0012 did *not* stall due to laminar leading-edge bubble-bursting – that instead the mechanism was turbulent leading-edge separation (turbulent flow had existed from very near the leading edge with separation being triggered by flow reversal starting at about 50 percent chord). According to Gault's stall classification criterion (ref. 17) the basic NACA 0012 airfoil lies approximately on the boundary between leading-edge bubble-bursting and mixed leading-edge/trailing-edge stall at the Reynolds numbers of the present experiment. To determine the sensitivity of the airfoil stall to leading-edge radius, an airfoil with reduced leading-edge radius was tested. Details in appendix B show that this airfoil did not exhibit significantly different results from the NACA 0012; it was only when the sharp leading-edge airfoil was tested that classical leading-edge bubble-bursting stall was observed.

Since a laminar separation bubble was observed on the NACA 0012 during static tests, and some previous investigators had associated the inception of dynamic stall with laminar bubble behavior, several boundary-layer trips were used. With or without the laminar leading-edge bubble, the NACA 0012 behavior was essentially unaffected (see appendix C for details).

19

As an additional way to modify the leading-edge bubble, a series of serrations was placed on the leading edge of the NACA 0012. This study also served as a check on the validity of the test results (see appendix D for details). They demonstrated that passive modifications were not able to promote trailing-edge stall, but were able in certain cases to convert the stall to a full leading-edge form. These results further support the proposition that the NACA 0012 is an airfoil that is fundamentally among the turbulent-separation stall types. Thus, further NACA 0012 modification may best be directed toward energizing the turbulent boundary layer to enable this airfoil to penetrate deeper into the dynamic stall regime before stalling, or to modify the airfoil in such a way as to control the rate of vorticity shedding. If at the same time the stall characteristics can be modified to soften the stall when it does occur, significant improvements in the stalling behavior can be achieved.

PARAMETRIC STUDIES

All the data presented so far have been for the reference condition, $\alpha = 15° + 10° \sin \omega t$, $Re = 2.5 \times 10^6$ and $k = 0.15$, to facilitate comparative analysis. In order to assess the effect of frequency, amplitude of oscillation, and Reynolds number on the stall behavior, each airfoil was also tested for ranges of these parameters. The basic NACA 0012 was used as a reference, even though it has a complex stall behavior, because it is expected that this airfoil will continue to serve as a standard of reference for future tests.

Effect of Reynolds Number

Of all the parameters studied, the effect of Reynolds number was the least dramatic. However, although minor, Reynolds number effects were detectable across the full range studied. At the lowest reduced frequency tested ($k = 0.004$), stall overshoot was minimal (fig. 31) and most of the observed hysteresis loop was attributable to a delay in reattachment (a Reynolds number effect), rather than vortex shedding. At the reference conditions (not shown), a similarly weak dependence on Reynolds number was detected in the force and moment variation with angle of attack.

The effects of Reynolds number on flow reversal for the standard amplitude and reduced frequency are shown in figure 32. A more gradual progression of rear-to-front flow breakdown is apparent at low Reynolds numbers, while at $Re \geq 2.0 \times 10^6$, the flow breakdown between the quarter chord and the leading edge is essentially simultaneous. At the highest Reynolds number, flow reversal on the rear of the airfoil is delayed as a function of Reynolds number, but this does not seem to affect the dynamic stall process on the forward part of the airfoil. Figure 33 presents the smoke-flow visualization results for the standard condition. A range of Reynolds numbers was studied for each of the airfoil configurations tested, but no other distinguishing events occurred.

20

Effect of Reduced Frequency

The type of boundary-layer separation, stall, and resultant force behavior was primarily determined by airfoil geometry. However, the next most significant parameter was reduced frequency. Variations in reduced frequency caused consistent changes in hot-wire reversal data (figs. 24-26), with the initial angle for flow reversal directly dependent on this frequency. The effect of frequency on the hysteresis loops for normal force and pitching moment were even more dramatic. The phase angle for moment stall, $C_{N_{max}}$ and $C_{M_{max}}$ for the three basic airfoils are given in table 2.

The sequence of events described for the various airfoils at $k = 0.15$ applies in general terms for all the frequencies studied; figures 34(a) and 34(b) show the development of the dynamic normal-force and pitching-moment loops for the frequency range of $k = 0.02$ to 0.25 for the NACA 0012. Since the flow reversal is delayed by increases in reduced frequency, the subsequent development of stall events is correspondingly delayed. At the lower frequencies ($k = 0.02 - 0.05$) a vortex is formed which moves down the airfoil, and is shed into the wake before the airfoil has reached the maximum incidence angle. As the frequency is increased, the delay in stall inception results in vortex interactions at higher and higher angles of incidence. Note that for $k > 0.20$ the lift is still increasing even though the angle-of-incidence is decreasing. The occurrence of moment-stall inception, maximum normal force, and maximum negative moment for the NACA 0012 are plotted in figure 35 again showing a direct dependence on frequency. This behavior is basically typical of all the airfoils tested; for reference, data at $k = 0.05$, 0.15, and 0.25 are also presented for the cambered (fig. 36), the sharp leading-edge (fig. 37) and the inverted-cambered airfoil (fig. 38). Each case is plotted with the basic NACA 0012 airfoil data at corresponding conditions. The data are equally scaled, but as noted earlier, absolute magnitudes are not indicated; instead, the data have been matched at $\alpha = 8°$ to allow for a better comparison of the effect of airfoil characteristics on C_N and C_M behavior.

Effect of Oscillation Amplitude Variation

Although the reduced frequency, $\omega c / 2U_\infty$ has long been the standard parameter for correlating dynamic stall data, the present study has shown that the amplitude of the oscillation also is important. The nondimensional frequency parameter does account for much of the primary unsteady aerodynamic effects of oscillation, but the means that are used to produce this parameter must be carefully considered. For example, in figure 39, the cambered airfoil is presented for $\alpha = 15° + 6°$ sin ωt; for $\alpha = 15° + 10°$ sin ωt; and for $\alpha = 15° + 14°$ sin ωt, all at the same reduced frequency, $k = 0.15$. It is clear that the resultant stall behavior is significantly dependent on the amplitude of oscillation.

The essential factor involved in these changes is the strength and timing of the dynamic stall vortex. When $\Delta\alpha = 6°$, the vortex is always shed at the maximum angle of oscillation, even if dynamic stall would not have occurred until later, had the amplitude been larger. Thus the change in pitch direction precipitates the stall. This early vortex shedding results in a milder

21

stall due to a reduction in vortex strength. When the $\Delta\alpha$ is increased to 10°, the vortex is only shed at the maximum angle of oscillation at the highest reduced frequency studied. At the lower frequencies, particularly the standard case of $k = 0.15$, a fully developed vortex forms naturally as a result of the breakdown of the boundary layer. For the extreme case of $\Delta\alpha = 14°$, there was no reduced frequency studied at which the vortex was delayed until maximum angle.

Tests at Constant Pitch Rate

Another possible parameter, pitch rate, was investigated to determine its applicability in correlating dynamic-stall data. If the history of the oscillation was important, then the character of the flow as the airfoil passed through the mean angle could be a determining factor in the resultant stall behavior. To evaluate this theory, the cambered and the NACA 0012 airfoils were oscillated at a series of conditions having the same pitch rate at the mean angle. As can be seen in figure 40, the stall behaviors were widely different, showing that pitch rate was not a satisfactory parameter for correlation.

Effect of Mean Angle Variation

The effect of changing the mean angle of oscillation while maintaining a constant oscillatory amplitude has been carefully investigated in the past (refs. 2, 3). It was observed that oscillation conditions that are either fully within the attached flow regime, or fully within the stalled regime show little hysteresis in the force and moment data. It is only when the airfoil oscillates in and out of stall that hysteresis is observed.

Although this result was substantiated in the present test, this was not a primary research area. Therefore, mean-angle variations during this test were limited to the NACA 0012 airfoil, which was oscillated at $k = 0.15$, $Re = 2.5 \times 10^6$ and $\alpha = 6° + 6° \sin \omega t$, $\alpha = 11° + 6° \sin \omega t$, and $\alpha = 15° + 6° \sin \omega t$. As expected, the airfoil never stalled for the case $\alpha_0 = 6°$ (not presented) and the results did not vary significantly from static data. The $\alpha_0 = 15°$ condition resulted in a premature stall (fig. 39) as was discussed earlier. However, the $\alpha_0 = 11°$ case is significantly different, and offers special insights into the effect on dynamic stall of combining mean-angle, oscillation-angle, and frequency variation. For this case, the airfoil oscillation exceeded the static stall by only a small margin. As the oscillatory frequency was increased, a critical frequency was reached when the flow no longer separated from the airfoil during any part of the cycle – the airfoil oscillated with no measurable stall effects on C_N or C_M, or on the flow near the surface. Figure 41(a) shows C_N, C_M, and pressure near the leading-edge at low frequency; note the graphic changes in all three variables as stall occurs. Figure 41(b) presents the same parameters for $k = 0.24$, where no stall was present.

It was possible that the gross stall behavior could be unaffected even though the boundary layer was experiencing flow reversal. Figure 42(a) shows

22

the C_N and hot-wire outputs at x/c = 0.05, 0.20, and 0.70; a comparison with figure 42(b) demonstrates that the boundary-layer flow as well as the potential flow show no evidence of stall at the reduced frequency of 0.24. Thus, the airfoil is completely free of any stall behavior at k = 0.24 but when the frequency is reduced, for this mean angle and oscillation angle, all the characteristics of dynamic stall reappear.

Summary of Parametric Study

The implications of the above findings can now be summarized.

Comparison of oscillatory data from different tests is subject to misinterpretation if the reduced frequency is matched without regard for the physical frequency and oscillation amplitude.

The strength and effects of the vortex, especially in terms of negative $C_{M_{max}}$, can be measurably altered depending on the history of oscillation. At each reduced frequency, the airfoil will experience moment stall at the angle when the boundary layer separates. If the oscillation amplitude is large enough, this separation will occur on the upstroke. However, if the airfoil oscillation direction is changed before this angle is reached, the separation is forced to occur at the top of the cycle. Less circulation is present at this time, and therefore a weaker vortex is formed.

The viscous behavior itself is significantly changed by varying the relative magnitudes of the unsteady and steady components of the adverse pressure gradient that the boundary layer must negotiate.

The airfoil does experience history effects, but these effects are not clearly correlatable based on any simple parameter of the mechanics of oscillation.

CORRELATION TECHNIQUE: C_N-C_M CROSSPLOT

The leading-edge vortex generated during dynamic stall is probably the most obvious characteristic of the stall process. As shown in the previous sections, this vortex causes radical variations from static stall behavior. In particular, C_N increases beyond 2π and may continue to do so during decreasing alpha, C_M becomes strongly negative, and large hysteresis loops appear for both C_N and C_M. It is of special significance that during these conditions, the relation between C_N and C_M remains basically unchanged.

To demonstrate this point, C_N-C_M plots have been created for a major portion of the test results. The data have been scaled by choosing C_N and C_M at α = 6° on the upstroke as a minimum (corresponding to fully unstalled values), and $C_{N_{max}}$ and $C_{M_{max}}$ of each test condition as a maximum. This non-dimensionalization will be shown to permit the results from a wide range of conditions to be overplotted in a manner that emphasizes the chronology of significant events occurring during dynamic stall.

Using the C_N-C_M technique, the data obtained during the frequency sweep of the basic NACA 0012 airfoil can be reasonably approximated by a single curve up to $C_{N_{max}}$ (fig. 43). This figure presents the major dynamic stall developments in a form that is independent of reduced frequency; the effects of boundary-layer displacement, then moment stall, passage of the vortex, and lift stall are identifiable. Note that although the angle corresponding to the inception of moment stall varies significantly across the frequency sweep, the location for this stall inception on the C_N-C_M curve remains almost constant. (The angles for $k = 0.05$, 0.15, and 0.25 are shown in fig. 43.) Also, the curves are essentially coincident up to $C_{N_{max}}$ and $C_{M_{max}}$ although the C_N-C_M values associated with any specific incidence angle (e.g., α_{max}) are significantly different (α_{max} is identified in bold type in the figure for $k = 0.10$, 0.15, 0.20 and 0.25). Compare figure 43 to figure 44 where C_N is plotted in conventional form for the same set of conditions. It is clear that the use of the C_N-C_M plot removes the angle-of-incidence as a parameter; the same C_N-C_M relationship results from a wide range of C_N-α and C_M-α relationships. This is because the induced aerodynamic effects of the vortex during its residence time become nondimensionally similar when scaled by the maximum C_N and C_M experienced. It is significant that this similarity is independent of the point in the cycle at which the vortex forms. As long as the vortex is triggered by separation of the boundary layer while the angle of incidence is still increasing, the rate of change of alpha, the maximum angle of oscillation, and the frequency of oscillation do not change this C_N-C_M correlation.

Further study of the C_N-C_M curves in figure 43 shows that the shedding of the secondary vortex occurs at lower C_N and C_M values as the reduced frequency increases (as indicated by the secondary loops appearing for $k = 0.10$ and 0.15). Since the free-stream velocity has been held constant for these cases, this secondary vortex characteristic may be associated with a change in phase of the interaction between the airfoil and the unsteady wake. This possibility becomes more apparent when C_N-C_M curves are created for a Reynolds number sweep at $\alpha = 15° + 10° \sin \omega t$ and constant k (fig. 45). In this case, both the pre-stall and post-stall behavior can be reduced to a single curve including the secondary vortex behavior. Even though the free-stream velocity and physical frequency have changed significantly the reduced frequency remains constant and results in coincident curves for C_N-C_M. This situation remains true for Reynolds number sweeps at $\alpha = 15° + 14° \sin \omega t$ and $\alpha = 15° + 6° \sin \omega t$ as well, although the shapes of the curves are dramatically different. The $\alpha = 15° + 14° \sin \omega t$ condition (fig. 46) repeats that observed at $\alpha = 15° + 10° \sin \omega t$, with the addition of a second secondary vortex; however, the $\alpha = 15° + 6° \sin \omega t$ case (fig. 47) shows a much altered curve. This variation can be attributed to the fact that for $\alpha = 15° + 10° \sin \omega t$ and $\alpha = 15° + 14° \sin \omega t$, the vortex is shed while the airfoil is still experiencing a pitch-up condition. Thus, the triggering of the vortex is primarily associated with unsteady boundary-layer phenomena. For the $\alpha = 15° + 6° \sin \omega t$ condition, the shedding of the vortex occurs at α_{max} and results in significant changes in the C_N-C_M relation because the full vortex strength is not attained in this case.

24

The effect of alpha schedule on the force and moment response has been shown to be significant for a wide range of Reynolds numbers. The effect of alpha schedule on response to frequency variation is even more striking. Comparison of the cambered airfoil at $\alpha = 15° + 10°$ $\sin \omega t$ (fig. 48) to the same airfoil oscillating at $\alpha = 15° + 6°$ $\sin \omega t$ (fig. 49) illustrates the strong changes that can occur. The $\alpha = 15° + 10°$ $\sin \omega t$ case experiences fully-developed vortex shedding during the upstroke; the $\alpha = 15° + 6°$ $\sin \omega t$ case has the vortex triggered by the change in the direction of oscillation. In fact, as noted on the figure, the break in the C_N-C_M curve always occurs at the maximum angle for the $\alpha = 15° + 6°$ $\sin \omega t$ case.

As the frequency is increased, the moment-stall angle increases. It is interesting to note that if the moment-stall angle is attained before the airfoil oscillation direction is reversed, the C_N-C_M crossplot is not dependent on oscillation amplitude. For example, the cambered airfoil at $\alpha = 15° + 6°$ $\sin \omega t$ and $k = 0.07$ has a C_N-C_M curve (fig. 49) that is strikingly similar to the C_N-C_M curve for the same airfoil at $\alpha = 15° + 10°$ $\sin \omega t$ and $k = 0.05$, which has moment stall at $\alpha = 20.5°$ (fig. 48). This occurs because the stall has already started before the maximum angle is reached, resulting in similar strength vortices. However, as the k is increased, the vortex shed during $\alpha = 15° + 6°$ $\sin \omega t$ no longer is fully developed; therefore, it results in the changing C_N-C_M patterns seen in the figure for $\alpha = 15° + 6°$ $\sin \omega t$ as compared to the data shown for $\alpha = 15° + 10°$ $\sin \omega t$.

Thus, the C_N-C_M crossplot clearly identifies those airfoil test conditions where dynamic stall has fully developed before the airfoil reaches maximum incidence, as compared to those cases where the stall is triggered prematurely by the airfoil motion as it reverses direction.

Universality of Correlation

The fact that C_N vs C_M assumes an almost universally similar curve for a wide range of reduced frequencies and Reynolds numbers offers interesting possibilities for the development of a universal dynamic-stall model that would permit prediction of stall behavior for many conditions with minimal experimental input. Certainly for the NACA 0012 airfoil at the conditions studied during this test, such a curve would seem feasible, and will be explored. It is interesting that the NACA 0012, the most difficult airfoil to analyze from the boundary-layer point of view, seems to be the easiest to study using the C_N-C_M technique. When the same method is applied to the cambered airfoil, a known trailing-edge stall airfoil, or to the leading-edge bubble-bursting stall airfoil, the general trend is again observed, but the data do not collapse so conveniently to a single curve. For the cambered airfoil (fig. 48) a greater dependence on reduced frequency is observed after the stall has begun, which indicates a greater dependence on k than is observed for the NACA 0012. However, it should be remembered that the cambered airfoil experiences a different vortex formation than the NACA 0012. The cambered airfoil vortex developed as a large, fairly-diffused vortex in the 25-50 percent chord region, whereas the NACA 0012 vortex developed with a tight core near the leading edge; this may explain the observed variation in C_N-C_M. It is somewhat less obvious why the leading-edge stall airfoil should show an even stronger dependence on reduced frequency (fig. 50). In this case, the

C_N significantly depends on reduced frequency even before dynamic stall has commenced, and definite excursions are observed in the C_N-C_M curves after stall inception. Here, the cause may be attributable to the mechanism that triggers the vortex, since this airfoil showed the most variation in stall angle from cycle-to-cycle. This airfoil exhibits variations that cannot fully be removed by the scaling technique presently used.

Even though these airfoils do not fully collapse to the universal C_N-C_M curve, the fact that the salient features of dynamic stall are repeatedly found to be represented by this single curve regardless of frequency, Reynolds number, or amplitude of oscillation, means that this technique should be valuable for correlating dynamic-stall test results.

DISCUSSION OF UNSTEADY SEPARATION ON DYNAMICALLY STALLING AIRFOILS

Flow reversal always results in boundary-layer separation in steady flow. This is not the case in the unsteady airfoil environment. For each of the three airfoil stall types tested, flow reversal occurred significantly before any detectable change in the normal force or moment coefficients (figs. 24-26). In fact, the flow had often reversed on the cambered airfoil all the way to the 25 percent chord point before moment stall was detected. For the $k = 0.15$, $Re = 2.5 \times 10^6$, and $\alpha = 15° + 10° \sin \omega t$ case, this airfoil had flow reversal on the surface for 8° of angle change before any catastrophic breakdown of the boundary-layer flow occurred and a leading-edge vortex developed. The normal-force curves showed a gradual decrease in the lift-curve slope during this angle change, but the basic aerodynamic characteristics correspond to those of an unstalled airfoil up to the inception of the stall vortex.

Applicability of Noninteracting Viscous Models to Dynamic Stalls

Flow reversal was often observed over a major portion of the cycle, without any detectable potential-flow effects. Thus, analysis of the unsteady boundary layer could be performed using attached weak-interaction potential-flow models up to the point where the vortex formed.

A primary area for research in the pre-stall environment centers on the delay in boundary-layer detachment during oscillation of the airfoil. Indeed, the problem to be solved is why an unsteady turbulent boundary layer remains attached in a pressure environment that would immediately separate a steady boundary-layer flow. A possible answer is that the fluid involved in the development of the dynamic stall does not have a constant history – much of the fluid has experienced milder adverse pressure gradients along its path than would occur in a steady flow, and can thus progress further before reversing. However, this possibility needs theoretical substantiation. To do so using a fully-interacting analysis would be a very complex task, and the choice of one turbulence model from among those presently available would require more information and understanding of the flow field than is now available. However, based on experimental observations, this question and others can be addressed using attached unsteady-flow analysis which would allow the

26

study of these subjects without requiring sophisticated potential-flow models. As the analysis of the attached flow prior to vortex formation is perfected, a greatly improved level of understanding about the character of the unsteady turbulent boundary layer on the oscillating airfoil would be obtained.

When the reversed flow region on an oscillating airfoil can be correctly modeled analytically, then techniques for improving the dynamic stall behavior of airfoils can be based on a more solid theoretical foundation. It is important that the many techniques presently being pursued for modeling of the complete dynamic stall process be first tested on the less severe problem of flow reversal without separation. Weak-interaction potential-flow modeling will permit this type of analysis to be performed.

The trailing-edge separation and the turbulent leading-edge separation stall types studied during this test were both preceded by a gradual progression of flow reversal from the trailing edge forward. Both resulted in a significant period of time when the flow was reversed at the surface with no change in the potential flow, and are therefore good candidates for weak-interaction analysis. The leading-edge bubble-bursting stall type also can be analyzed to first order using weak interaction techniques. Thus, by analyzing the unsteady boundary-layer behavior in a weak-interaction potential flow, it should be possible to predict at least the type of dynamic stall that will occur on an arbitrary airfoil design.

Formation of the Dynamic Stall Vortex

The actual formation of the dynamic-stall vortex is possibly the most difficult of the phenomena to explain concerning dynamic stall. Dynamic stall has already begun once the vortex has formed; approximate prediction of the flow after this point would probably reduce to a potential-flow description of the kinetics of the fluid motion rather than the kinematics of the fluid itself. Provided the vortex strength and origin are known, a calculation procedure for its motion and its effects on the airfoil normal-force and pitching-moment characteristics has been proposed (refs. 14, 20). Thus, the actual mechanism by which the vortex is formed is one of the serious unsolved problems in the analysis of dynamic stall. The mechanism by which the boundary-layer vorticity transfers into the tight, strong vortex that is shed at the point of dynamic stall is probably the key to stall modification. It is, therefore, very important to identify the factors involved in its inception.

As discussed earlier, there are cases where the stall delay can occur while shedding a less than fully developed vortex, or even without forming a vortex at all. On the other hand, the self-triggered vortex that occurs for high-amplitude oscillation is very strong and is difficult to analyze because the instability that triggers the vortex can be initiated from many different sources.

It is thus advantageous to study cases where the vortex has been triggered by a controlled external input. For example, $\alpha = 15° + 6° \sin \omega t$ offers a condition where the change in oscillation direction causes the vortex to form. As has been shown in the C_N-C_M plots for the cambered airfoil at

27

$\alpha = 15° + 6° \sin \omega t$ (fig. 49), there exists a definite dependence on the oscillation rate; the strength of the vortex seems to be directly related to the oscillation rate. This case offers the theoretician a condition where the amount of vorticity shed from the leading edge is directly related to reduced frequency.

Another condition that offers insight into the characteristics of the viscous flow is the $\alpha = 11° + 6° \sin \omega t$ case discussed earlier. At low frequency, the boundary layer separated, but as the frequency was increased, the flow reached a point where unsteady effects prevented separation. This condition is of significant value as a test of theoretical models, since this problem (at high frequency) can be approached using weak-interaction potential flow. The validity of the model can then be tested by reducing the oscillation frequency and observing the point at which the boundary-layer flow breaks down and separation occurs during the cycle.

A further case of interest occurred for the cambered airfoil for $\alpha = 15° + 6° \sin \omega t$ and $k = 0.24$ (fig. 40). At these conditions the airfoil experienced a separation that extended to the leading edge, but did not form the vortex normally associated with dynamic stall. In this case, there was a significant overshoot of the static stall angle. Separation was dynamically delayed, but the absence of a shed vortex implies that the conditions that force the vorticity to shed from the leading edge were not met, and the vorticity entered the wake in a more normal manner.

All of these cases are ones that only moderately push the limits of theoretical modeling, and, therefore, are suggested as starting cases for analyzing the viscous behavior responsible for dynamic stall delay. It should be remembered that by the time the vortex begins to form at the leading edge, flow reversal has usually occurred near the surface over much of the airfoil. The boundary layer has sometimes remained attached for as much as 6° to 8° incidence change, even with this flow reversal. In summary, it seems that the primary question to be answered by the viscous-flow theoretician is: Why does the turbulent boundary layer remain attached in a pressure environment that would immediately separate a steady flow?

CONCLUSIONS

Based on the present experiment, the following conclusions can be made.

1. A new form of leading-edge stall should be included in discussions of dynamic stall: abrupt leading-edge turbulent separation. The basic NACA 0012 airfoil at helicopter flight Reynolds numbers and low Mach numbers stalls dynamically by the mechanism of abrupt turbulent leading-edge separation initiated by a progressive forward movement of trailing-edge separation. The boundary-layer behavior leading to this form of stall is quite distinct from that associated with dynamic stalls initiated by laminar bubble-bursting, or conventional trailing-edge separation.

28

2. Dynamic stall is sensitive to many parameters; of those studied, the following are presented in order of decreasing importance: airfoil geometry, frequency of oscillation; amplitude of oscillation; and Reynolds number.

3. The essential character of the stall phenomenon can be reduced to a single parametric curve by plotting C_N versus C_M in properly scaled form.

4. Dynamic stall can result from several different boundary-layer developments. In particular, during the present study three distinct boundary-layer separation mechanisms were observed to cause the same classical dynamic-stall behavior.

5. Extensive regions of reversed flow can exist on oscillating airfoils before normal-force and pitching-moment data are affected.

6. Details of the boundary-layer characteristics near the airfoil surface are necessary in any future experiments of oscillating airfoils if proper classification of airfoil stall character is to be made.

7. There is merit in analyzing dynamic stall-delay using weak-interaction models, since flow reversal was often observed over a major portion of the airfoil before any potential-flow effects were observed in the integral force and moment data.

Ames Research Center
      National Aeronautics and Space Administration
            and
Ames Directorate
      U.S. Army Air Mobility R&D Laboratory
            Moffett Field, CA 94035, July 2, 1976

APPENDIX A

ANALYSIS OF TUNNEL INTERFERENCE EFFECTS

In most wind-tunnel tests, the presence of the tunnel walls induces some changes in the aerodynamic parameters. Correction for tunnel wall boundary-layer interference, tunnel blockage, and streamline curvature effects can be performed for unstalled airfoils in steady flow (ref. 21); however, to analytically correct data for oscillatory motion having large areas of stalled flow is beyond the state of the art. The significance of the wall effects for the present test, therefore, have been ascertained partially by experiment. In order to obtain information about the tunnel-model interaction, a flow-direction sensing vane, a hot-wire anemometer probe, and a local pitot-static probe were mounted from the tunnel ceiling about two chord lengths ahead of the model quarter chord (fig. 11). In addition, the model was tested with and without end plates.

Model-Tunnel Wall Boundary-Layer Interaction

Separation of the tunnel-wall boundary layer in the vicinity of a high-lift airfoil is a common static-airfoil test problem, and the present test was no exception. As the airfoil was increased in angle-of-attack, successively greater outboard portions of the airfoil separated, ultimately resulting in a three-dimensional stall pattern. However, this was primarily a static, or at most a low-frequency phenomenon. The addition of end-plates (fig. 51) caused major changes in the results for $k < 0.10$, significantly reducing the three-dimensionality that was present at these frequencies. However, for $k \geq 0.10$ no measurable differences in behavior could be detected with or without end plates. As further verification of this, hot-wire probes were mounted at $x/c = 0.70$ at seven span-wise locations. The boundary-layer growth as detected by these probes was uniform across the span at the higher reduced frequencies, even when the end plates were removed. Since most of the present studies of airfoil boundary layer and force measurements were performed at or above $k = 0.15$, end plates were not considered essential. Although the unsteady data for frequencies below $k = 0.05$ are open to possible reinterpretation, the data presented for these conditions are consistent with the trends obtained at higher frequencies. In any case, for $k \geq 0.15$, measurement nonuniformities were below the accuracy threshold of the test program, and the conclusions presented in the report are for these higher frequencies.

Tunnel Blockage

Direct measurement of blockage effects was not feasible in the dynamic environment. Therefore, the effect of blockage was inferred from the measurements of the instantaneous free-stream dynamic pressure, velocity, and turbulence intensity during tests of the NACA 0012. Although these data were recorded ahead of the model, it is deemed representative of the tunnel

30

blockage effects, since blockage results in a global interference which affects the flow far from the model.

Tunnel blockage during static tests is conventionally associated with a decrease in cross-sectional area at the location where the model is stationed, and for the present test this resulted in an increase of free-stream velocity that was at most of the order of 3 percent (within the accuracy of the present test). The dynamic blockage effects were determined by studying two oscillatory conditions: unstalled (where solid blockage was important); and stalled (where wake blockage was also important). The analysis of the blockage during the unstalled oscillation was performed on two cases: $\alpha = 6° + 6° \sin \omega t$ and $\alpha = 11° + 6° \sin \omega t$. As can be seen from figure 52, there is no noticeable effect on local q or the local free-stream velocity, for these conditions.

The situation is significantly altered when separation is present. After dynamic stall occurs, a significant portion of the tunnel mass flow is affected, being either trapped in the separated region or absorbed in the shed vortex (which traveled at only 40 percent of free-stream velocity). For these conditions, conservation of mass required that the upstream velocities must adjust to this strong change in the flow near the model – this was observed for all cases where stall was present on the airfoil (fig. 53). The effect of frequency change on the blockage due to stall is presented in figure 54. A sinusoidal variation in q was observed for $k = 0.05$. However, this variation was considerably damped as k was increased from 0.05 to 0.15; and for $k \geq 0.15$, the q variation becomes independent of frequency. Again, based on these considerations, it was decided that for conditions at $k = 0.15$ or above, tunnel blockage corrections were not required.

Streamline Curvature

In steady flow, streamline curvature effects due to the presence of tunnel walls can cause an airfoil to appear cambered (of the order of 1 percent) (ref. 21). This effect is a significant one in static testing, but recent research in slotted tunnels (ref. 22) has shown that 2-percent slotting of the tunnel ceiling and floor will fully correct the camber effect on a 4-ft chord airfoil (duplicating the present test) in static testing. When the airfoil was oscillated, the differences between results measured in a closed tunnel and one with 2-percent slots were less than the differences measured from one cycle to the next (ref. 23).

Flow Direction

Although no specific conclusions were drawn from the results of the oscillating vane data taken during the test, representative outputs of this vane are presented in figure 55. The variations are quite random at lower frequencies, and becomes periodic only at the higher frequency range. This synchronization can be associated with the greater far-field influence caused by the increased lift at high frequency.

31

Turbulence Intensity

The turbulence intensity was very dependent on the amount of stall present in the cycle. Figure 52 shows the response to oscillations below stall. A small change in turbulence intensity was noticed for $15° + 6° \sin \omega t$ and $k = 0.15$ (not shown); however, phasing becomes obvious for $15° + 10° \sin \omega t$ and $k = 0.15$ (fig. 53(a)), and is very definite for the $15° + 14° \sin \omega t$ and $k = 0.10$ condition (fig. 53(b)). Upstream, q and U_∞ show the same pattern, although they are somewhat less sensitive to amplitude. Before stall, there is no correlation; for $15° + 6° \sin \omega t$, a correlation appears; the correlation is fully established at $15° + 10° \sin \omega t$; and the correlation is not significantly increased for $15° + 14° \sin \omega t$. This progression can be attributed to the fact that at $15° + 6° \sin \omega t$ the shed vortex has not fully developed, and therefore does not affect the tunnel flow as severely as it does for the cases where the vortex is allowed to reach full strength before being shed. Conversely, the $15° + 10° \sin \omega t$ and $15° + 14° \sin \omega t$ cases have fully developed vortices at stall, and therefore result in strong correlations.

Conclusions

Based on the above observations, dynamic data obtained on an oscillating airfoil is much less dependent on wall corrections than its static counterpart. Therefore, with the exception of nondimensionalization of normal force and pitching moment by the instantaneous value of dynamic pressure obtained during the cycle, no wall or tunnel corrections have been applied to the data, nor are they considered necessary for $k \geq 0.15$.

32

APPENDIX B

REDUCED LEADING-EDGE AIRFOIL RESULTS

The results of the test programs have shown that the NACA 0012 airfoil stalled due to turbulent leading-edge separation. However, it was necessary to verify that this separation condition was not overly sensitive to leading-edge radius. According to Gault (ref. 17), the NACA 0012 is on the boundary of leading-edge bubble-bursting stall. To study this effect, the extension shown in figure 4 was added, reducing the leading-edge radius from 0.0158c to 0.010c and the Gault leading-edge geometry parameter, Y (at x/c = 0.0125), from 0.019 to 0.016. This configuration was tested with and without the standard trip described in appendix C at the leading edge.

The static-stall characteristics of this modified airfoil were slightly more abrupt than that of the basic NACA 0012, and stall occurred at a slightly lower angle. The dynamic results are shown in figure 56. The test results at k = 0.15 indicate a fairly abrupt flow breakdown at $\omega t \simeq \pi/4$ (α = 22.1°), and dip in the C_N-α curve before the vortex induced overshoot of C_N begins. However, there was no indication of bubble-bursting flow reversal or separation as was observed on the sharp leading-edge airfoil.

Since a laminar bubble was observed at α = 12° in steady flow, a trip was used to eliminate the bubble completely. These results exhibited an earlier onset of stall, both statically and dynamically, than was observed without the trip (fig. 57).

Both with and without the trip, the primary vortex seemed to form closer to the leading edge than on the basic NACA 0012 airfoil. A secondary vortex that was stronger than that occurring on the basic NACA 0012 airfoil caused a significant increase in C_N during the downstroke for the k = 0.15 condition (figs. 56, 57). The pitching moment is also affected by this phenomenon. However, the reduction in leading-edge radius to 0.010c did not result in classical leading-edge bubble-bursting stall.

It is especially significant that true leading-edge stall was not observed until the NACA 0012 airfoil leading-edge radius was reduced to 0.004c, the case discussed earlier as "leading-edge laminar-bubble bursting." This demonstrates that the basic NACA 0012 airfoil configuration is actually well within the boundary for turbulent leading-edge boundary-layer separation.

APPENDIX C

BOUNDARY-LAYER TRIPS ON THE NACA 0012 AIRFOIL

In all of the basic NACA 0012 airfoil test cases studied, the existence of a distinct leading-edge laminar-separation bubble could be inferred from the hot-wire and pressure-transducer signals, and in the static case, from oil-flow visualization. At high incidence, that is, $\alpha \geq 14°$, the bubble was located very near the leading edge, between $s/c = 0.01$ and 0.02; that is, upstream of $x/c = 0.007$. However, the initial breakdown of the flow into a stalled condition always seemed to occur downstream of this location, both statically and dynamically, as an abrupt turbulent separation. Since several previous investigators have associated the inception of dynamic stall with laminar-bubble behavior it became important to establish the nature of dynamic-stall effects without a bubble present.

A trip was installed at the leading edge of the basic NACA 0012 airfoil to eliminate the leading-edge laminar-separation bubble by promoting transition to turbulence ahead of the bubble. Several trip designs were investigated, including an upstream-facing saw-tooth-edged tape, and a rectangular trip-tape 0.46 mm wide by 0.16 mm high. (Since there was no detectable difference in either the static or dynamic results between these two designs, the rectangular tape was adopted as the standard trip configuration.) Flow reversal measurements obtained with the rectangular trip are shown in figure 58 for the same flow conditions depicted in figure 26 without the trip. The type III flow reversal on the rear position of the airfoil was virtually unaffected, but the breakdown of the leading-edge flow began earlier with the trip than in the case without the trip.

The onset of stall was also more irregular, complex, and ill-defined with the trip than without (as indicated by the dashed lines, and multiplicity of signal types appearing in figure 58, compared to the results shown in figure 26). For $k \geq 0.05$, there seemed to be a tendency for the boundary-layer flow between $x/c = 0.05$ and 0.20 to break down slightly before the flow at midchord, based on the hot-wire signals and tuft behavior. Also it should be mentioned that for $k \geq 0.05$ a "vortex peak" first appeared in the static pressure at $x/c = 0.05$ whereas this was not observed until $x/c \gtrsim 0.10$ without the trip. The earlier onset of dynamic stall and earlier shedding of the primary and secondary vortex with the trip can be seen (fig. 59). Differences also appear in the fully stalled regime after the secondary vortex is swept downstream, and the reattachment process seems to proceed more smoothly in the tripped case. However, the basic process of dynamic overshoot of the static stall angle, the development of flow reversal, and the ultimate vortex shedding are not fundamentally changed, even though the bubble has been removed. Thus, it can be concluded that the leading-edge bubble does not play an important part in dynamic stall on the NACA 0012 airfoil at helicopter flight Reynolds number and reduced frequency.

34

APPENDIX D

SERRATIONS ON LEADING EDGE OF NACA 0012

In order to evaluate the possibility of modifying the NACA 0012 stall behavior passively, several series of leading-edge serrations were tested. The general design of these serrations was based on earlier static test results (ref. 24); in addition, several new serration designs evolved during the test and were evaluated. Figures 60 to 62 present the results for three of the series tested: $B1$, a configuration essentially scaled from the static tests and mounted near the stagnation point; $B4$, a strip with no serrations mounted at the leading edge; and $B20BR$, a serration type which was bent to the local contour of the leading edge and reversed so that the serrations pointed upstream toward the stagnation point. Analysis of oil flow visualization during static tests showned that $B1$, the original serration design, did not trip the boundary layer ahead of the laminar bubble, but did interact with the bubble to the extent that local distortions appeared. As seen in figure 60, dynamic testing of this design showed that the interactions caused by the serrations did not significantly change the dynamic C_N and C_M characteristics. Since it has already been demonstrated that the NACA 0012 stalls dynamically due to turbulent leading-edge separation, the effect of the basic serrations may have been absorbed by the turbulent flow occurring during the oscillation. In any case, the basic serrations did not provide an effective modification of the dynamic stall of the NACA 0012 airfoil for the Reynolds numbers considered during this test.

When the metal strip $B4$ was installed at the leading edge a more noticeable change in C_N and C_M occurred (fig. 61). In this case, the boundary layer was probably tripped as it left the downstream edge of the strip; the resulting force and moment curves are similar to those of the NACA 0012 airfoil tripped using the standard technique (fig. 59). In contrast, the $B20BR$ configuration (fig. 62) seems to have changed the NACA 0012 airfoil into a fully leading-edge stall type. The $B20BR$ results are compared to the NACA 0012 airfoil in figure 62, and to the sharp leading-edge airfoil in figure 63.

It is interesting to note that the normal-force and pitching-moment characteristics of the $B20BR$ airfoil so closely resemble those of the sharp leading-edge airfoil, even though the serrations produced a fully turbulent flow on the entire upper surface (compared to the sharp leading-edge airfoil where the laminar bubble-bursting was the dominant boundary-layer characteristic). Thus, the stall characteristics of airfoil $B20BR$ seem to imply a bubble-bursting type of stall, but originating in a turbulent boundary layer.

In any case, passive modifications in the form of serrations or boundary-layer trips, which produced major changes in the laminar leading-edge separation bubble, did not promote trailing-edge stall on the NACA 0012 airfoil. This further supports the conclusion that the NACA 0012 airfoil is not a leading-edge bubble-bursting stall airfoil.

REFERENCES

1. Bisplinghoff, Raymond L.; Ashley, Holt; and Halfman, Robert L.:
   Aeroelasticity. Addision-Wesley Pub. Co., 1955.

2. Carta, F. O.: Experimental Investigation of the Unsteady Aerodynamic
   Characteristics of a NACA 0012 Airfoil. UAC RL Report M-1283-1,
   July 26, 1960.

3. Harris, Franklin D.; and Pruyn, Richard R.: Blade Stall - Half Fact,
   Half Fiction. J. Amer. Helicopter Soc., vol. 13, no. 2, April 1968,
   pp. 27-48.

4. Liiva, J.; Davenport, F. J.; Gray L.; and Walton, I. C.: Two-Dimensional
   Tests of Airfoils Oscillating Near Stall. U.S. Army AVLABS, TR68-13,
   1968 (also J. of Amer. Helicopter Soc., vol. 14, no. 2, 1969, pp. 26-33;
   and J. Aircraft, vol. 6, no. 1, 1969, pp. 46-51).

5. Gray, L.; Liiva, J.; and Davenport, F. J.: Wind-Tunnel Tests of Thin
   Airfoils Oscillating Near Stall. U.S. Army AVLABS, TR68-89A, 1969.

6. Windsor, R. I.: Measurement of Aerodynamic Forces on an Oscillating Air-
   foil. U.S. Army AVLABS TR69-98, Mar. 1970.

7. Garelick, M. S.: Non-Steady Airloads on Dynamically Stalling Two-
   Dimensional Wings. Master's Thesis, M.I.T., 1967.

8. Ham, N. D.; and Garrelick, M. S.: Dynamic Stall Considerations in
   Helicopter Rotors. J. Amer. Helicopter Soc., vol. 13, April 1968,
   pp. 49-55.

9. Martin, J. M.; Empey, R. W.; McCroskey, W. J.; and Caradonna, F. X.: An
   Experimental Analysis of Dynamic Stall on an Oscillating Airfoil.
   J. Amer. Helicopter Soc., vol. 19, no. 1, Jan. 1974, pp. 26-32.

10. Werlé, H.: Visualization of Hydrodynamique d'Ecoulements Instationnaires.
    Proc. of the IUTAM Symposium on Recent Research in Unsteady Boundary
    Layers, Quebec, Canada, May 24-28, 1971, vol. 2, pp. 1422-1443.

11. Goldstein, S.: On Laminar Boundary-Layer Flow Near a Position of
    Separation. Quart. J. Mech. Appl. Math. 1, pt. 1, March 1948,
    pp. 43-69.

12. Sears, W. R.; and Telionis, D. P.: Unsteady Boundary-Layer Separation.
    Proc. IUTAM Symposium on Recent Research in Unsteady Boundary Layers,
    Eichelbrenner, E. A., ed., Quebec, May 24-28, 1971, pp. 404-447 (also,
    SIAM J. Applied Math., vol. 28, no. 1, 1975, pp. 215-235 with title:
    Boundary-Layer Separation in Unsteady Flow).

36

13. Patel, V. C.; and Nash, J. F.: Unsteady Turbulent Boundary Layers with Flow Reversal, Unsteady Aerodynamics. vol. 1, Univ. of Arizona (R. B. Kinney, ed.), 1975.

14. Ham, Norman D.: Aerodynamic Loading on a Two-Dimensional Airfoil During Dynamic Stall. AIAA Journal, vol. 6, no. 10, Oct. 1968, pp. 1927-1934.

15. Johnson, Wayne; and Ham, Norman D.: On the Mechanism of Dynamic Stall. J. Amer. Helicopter Soc., vol. 17, no. 4, Oct. 1972, pp. 36-45.

16. Nash, J. F.; Carr, L. W.; and Singleton, R. E.: Unsteady Turbulent Boundary Layers in Two-Dimensional Incompressible Flow. AIAA Journal, vol. 13, no. 2, Feb. 1975, pp. 167-173.

17. Gault, Donald E.: A Correlation of Low-Speed Airfoil-Section Stalling Characteristics with Reynolds Number and Airfoil Geometry. NACA TN 3963, 1957.

18. Parker, A. G.; and Bicknell, J.: Some Measurements on Dynamic Stall. J. Aircraft, vol. 11, no. 7, July 1974, pp. 371-374.

19. Sandborn, V. A.; and Kline, S. J.: Flow Models in Boundary-Layer Stall Inception. J. Basic Eng., Ser. D., vol. 83, 1961, pp. 317-327.

20. Baudu, N.; Sagner, M.; and Souquet, J.: Modelisation du Decrochage Dynamique d'un Profil Oscillant, AAAF 10th Colloque d'Aerodynamique Appliquee, Lille, France, Nov. 1973.

21. Pope, Alan; and Harper, John J.: Low-Speed Wind Tunnel Testing. John Wiley & Sons, 1966.

22. Parker, A. G.: Use of Slotted Walls to Reduce Wind Tunnel Boundary Corrections in Subsonic Flow. AIAA Journal, vol. 12, no. 12, Dec. 1974, pp. 1771-1772.

23. Parker, A. G.: Force and Pressure Measurements on an Airfoil Oscillating Through Stall. Final Report Part II TEES-3018-75-01A, Aug. 1975, Texas A&M University, NASA CR-145877.

24. Soderman, P. T.: Aerodynamic Effects of Leading-Edge Serrations on a Two-Dimensional Airfoil. NASA TM X-2643, Sept. 1972.

TABLE 1.– MATRIX OF TEST CONDITIONS RECORDED AND PRESENTED

Airfoil Geometry	Frequency Variation $\alpha = 15° + 10° \sin \omega t$, $Re = 2.5 \times 10^6$								Reynolds Number Variation $\alpha = 15° + 10° \sin \omega t$, $k=.15$, $Re \times 10^{-6}$						Amplitude Variation $k=.15$, $Re=2.5 \times 10^6$	
	$k=0$	$k=.004$	$k=.02$	$k=.05$	$k=.10$	$k=.15$	$k=.20$	$k=.25$	1.0	1.5	2.0	2.5	3.0	3.5	$\alpha_1=6°$	$\alpha_1=14°$
Basic Airfoils																
NACA 0012	FH	FH	FHS	FHS	FHS	FHS	FHS	FHS	FHS	FHS	FHS	FHS	FHS	FHS	FHS	FHS
Sharp L.E.	FHS	FH	FH	FHS	FH	FHS	FH	FHS		FH		FH	FH			FH
Camber	FHS	FH	FH	FHS	FH	FHS	FH	FHS		FH		FH		FH	FHS	FH
Modifications																
B1	FH	FH	FH	FH	FH	FH	FH	FH		FH		FH		FH		
B20BR	FHS	H	FH	FHS	FH	FHS	FH	FHS		S		FHS				
B4			F	F	F	F	F	F				F				
Reduced L.E.	FHS	FH	FH	FHS	FH	FHS	FH	FH		F		FHS		H		
Neg. Camber	F		F	F	F	F	F	F				F				
Camber $15° \pm 14°$	F	F	F	F	F	F	F			F	F	F			F	
Tripped Airfoils																
NACA 0012	FH	FH	FHS	FHS	FHS	FHS	FHS	FHS	S	FHS	S	FHS	S	FHS		
Reduced L.E.	FHS	FH	FH	FHS		FHS		FHS		FH	F	F				
Neg. Camber	F	FH	F	F	F	F	F	F				F				

F – Force and moment data
H – Hot wire anemometer data
S – Smoke flow visualization
▨ – Data presented

Special cases – force data only

Airfoil	α_0	α_1	K	$Re \times 10^{-6}$
NACA 0012	15°	10°	.004	1.5, 2.0, 3.5
	10°	6°	.24	2.5
	11°	6°	.24	2.5
	15°	6°	.24	1.0, 1.5, 2.5
	15°	14°	.10	1.0, 1.5, 2.0
Camber	15°	6°	.02, .075, .11, .15, .20, .24	2.0

TABLE 2.— PHASE ANGLE FOR MOMENT STALL AND MAXIMUM NORMAL
FORCE AND PITCHING MOMENT AT VARIOUS REDUCED FREQUENCIES;
$Re = 2.5 \times 10^6$, $\alpha = 15° + 10°$ sin $\phi\pi/180$

Basic NACA 0012 Airfoil

k	ϕ, Moment Stall	ϕ, $C_{N_{max}}$	ϕ, $C_{M_{max}}$
0.02	10°	13°	19°
0.05	22°	32°	33°
0.10	42°	58°	63°
0.15	55°	76°	84°
0.20	67°	95°	107°
0.25	78°	104°	124°

Sharp Leading-Edge Airfoil

k	ϕ, Moment Stall	ϕ, $C_{N_{max}}$	ϕ, $C_{M_{max}}$
0.02	−17.5°	−9°	0°
0.05	−11°	4°	7°
0.10	0°	22°	27°
0.15	7°	42°	49°
0.20	15°	63°	74°
0.25	26°	67°	95°

Cambered Airfoil

k	ϕ, Moment Stall	ϕ, $C_{N_{max}}$	ϕ, $C_{M_{max}}$
0.02	18°	28°	28°
0.05	30°	48°	48°
0.10	46°	70°	75°
0.15	64°	90°	93°
0.20	83°	110°	115°
0.25	102°	120°	137°

NACA 0012 AIRFOIL

$$\alpha = 15° + 10° \sin \omega t \qquad k = \frac{\omega c}{2U_\infty} = 0.15 \qquad Re = 2.5 \times 10^6$$
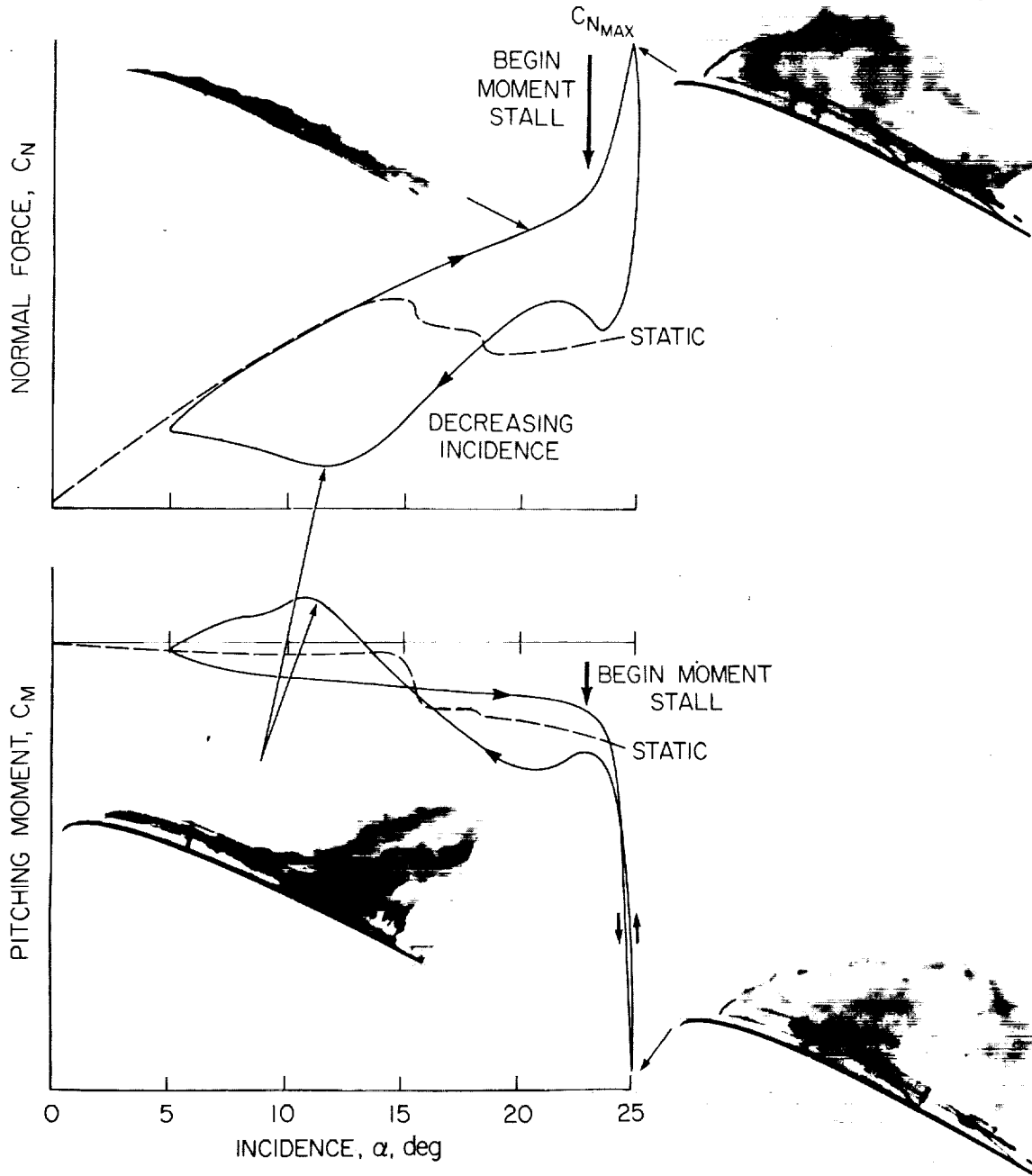
Figure 1.- Typical static and dynamic variation of normal force and pitching moment as function of angle-of-incidence.

TYPICAL VELOCITY PROFILE

EDGE OF BOUNDARY LAYER

SEPARATION POINT

REVERSED FLOW REGION

WAKE REGION
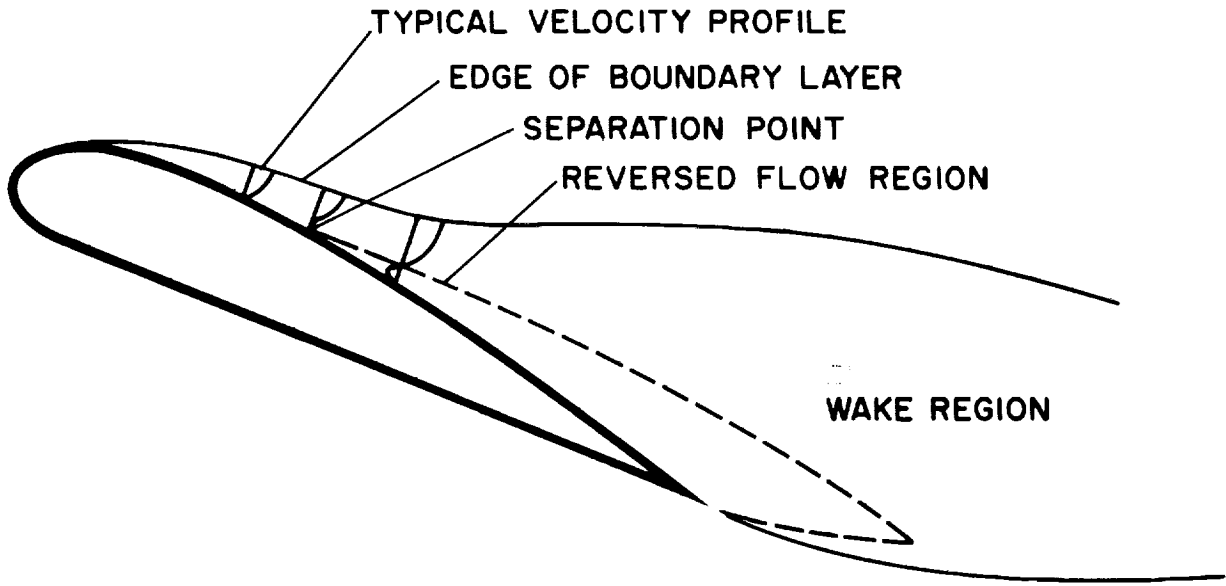
Figure 2.- Steady separation on an airfoil.

EDGE OF BOUNDARY LAYER

TYPICAL VELOCITY PROFILE

REVERSED FLOW BOUNDARY

WAKE
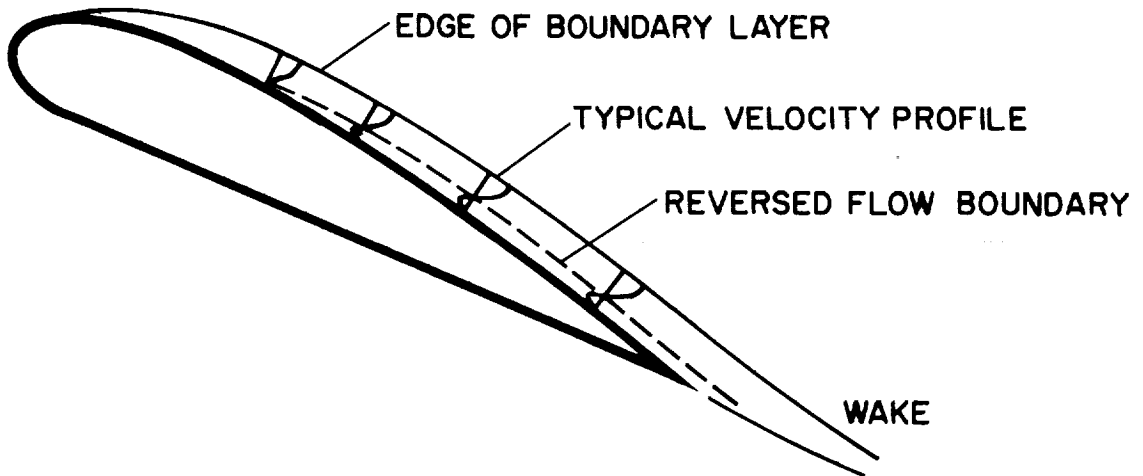
Figure 3.- Unsteady flow reversal on an oscillating airfoil.

42

0.035c

0.010c

SHARP LEADING-EDGE
$r_o/c = 0.004$

0.018c

0.004c

REDUCED L.E. RADIUS
$r_o/c = 0.010$

BASIC NACA 0012
$r_o/c = 0.0158$

0.025c

CAMBERED AIRFOIL $r_o/c = 0.0117$
POSITIVE AND NEGATIVE INCIDENCE

L.E. BUBBLE

SERRATIONS ON
LOWER SURFACE

L.E.

$\alpha = 15°$
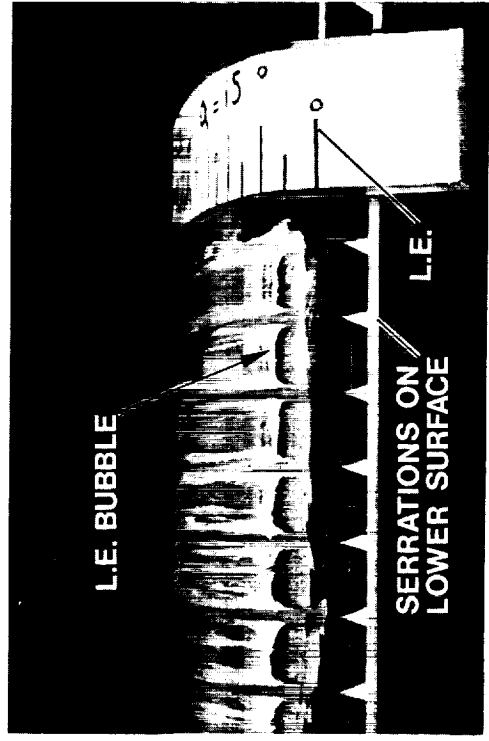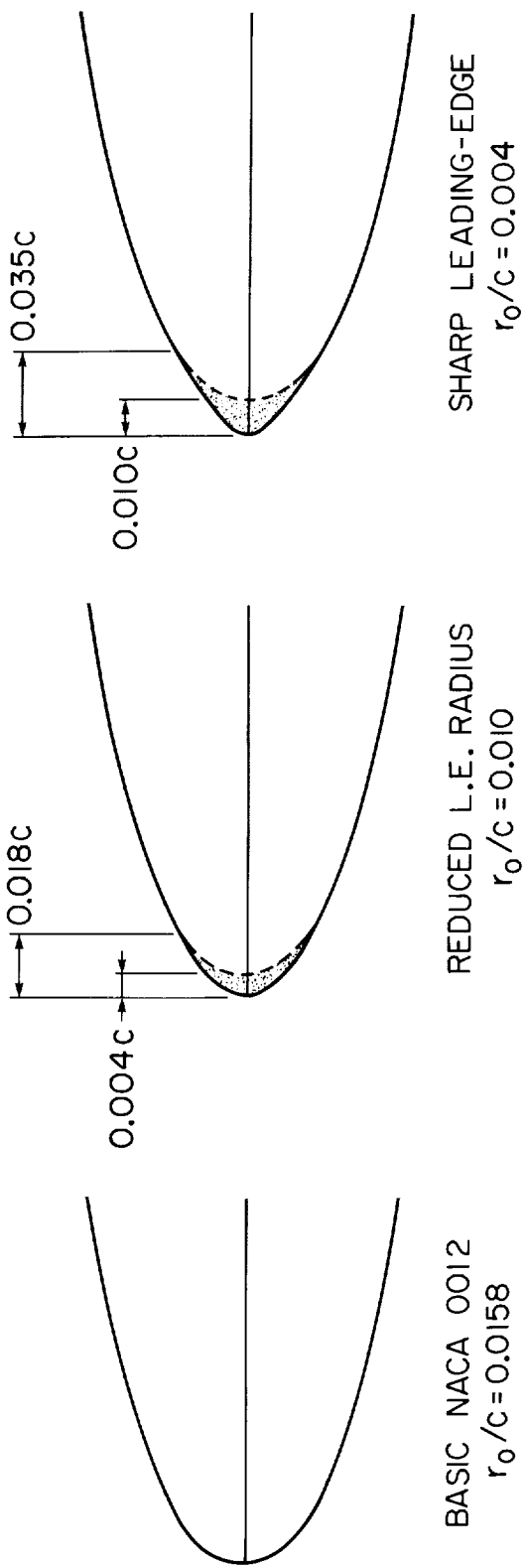
NACA 0012 WITH SERRATIONS
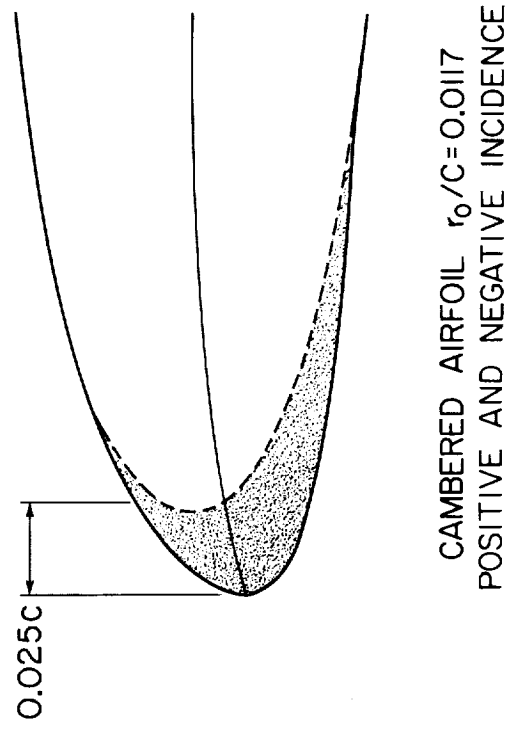
Figure 4.- Airfoil configurations tested.
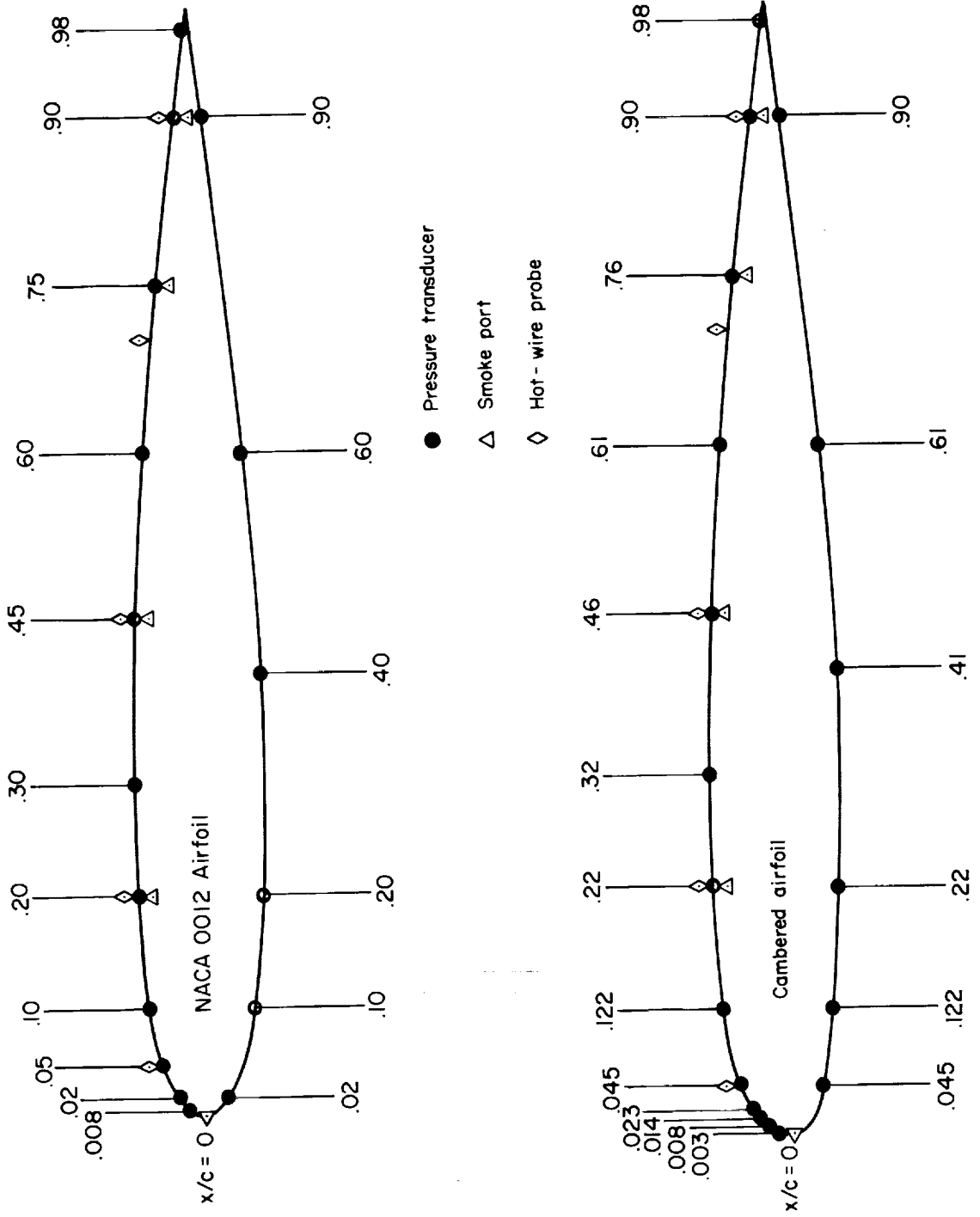
Figure 5.– Schematic showing locations of pressure transducers, hot–wire probes, and smoke ports.

Main tunnel pitot probe

Hot-wire probe

Transducer reference pitot probe

Flow angle vane

Tubular Spar

Ground plane   Black velvet

Figure 6.- View of two-dimensional airfoil in wind tunnel.
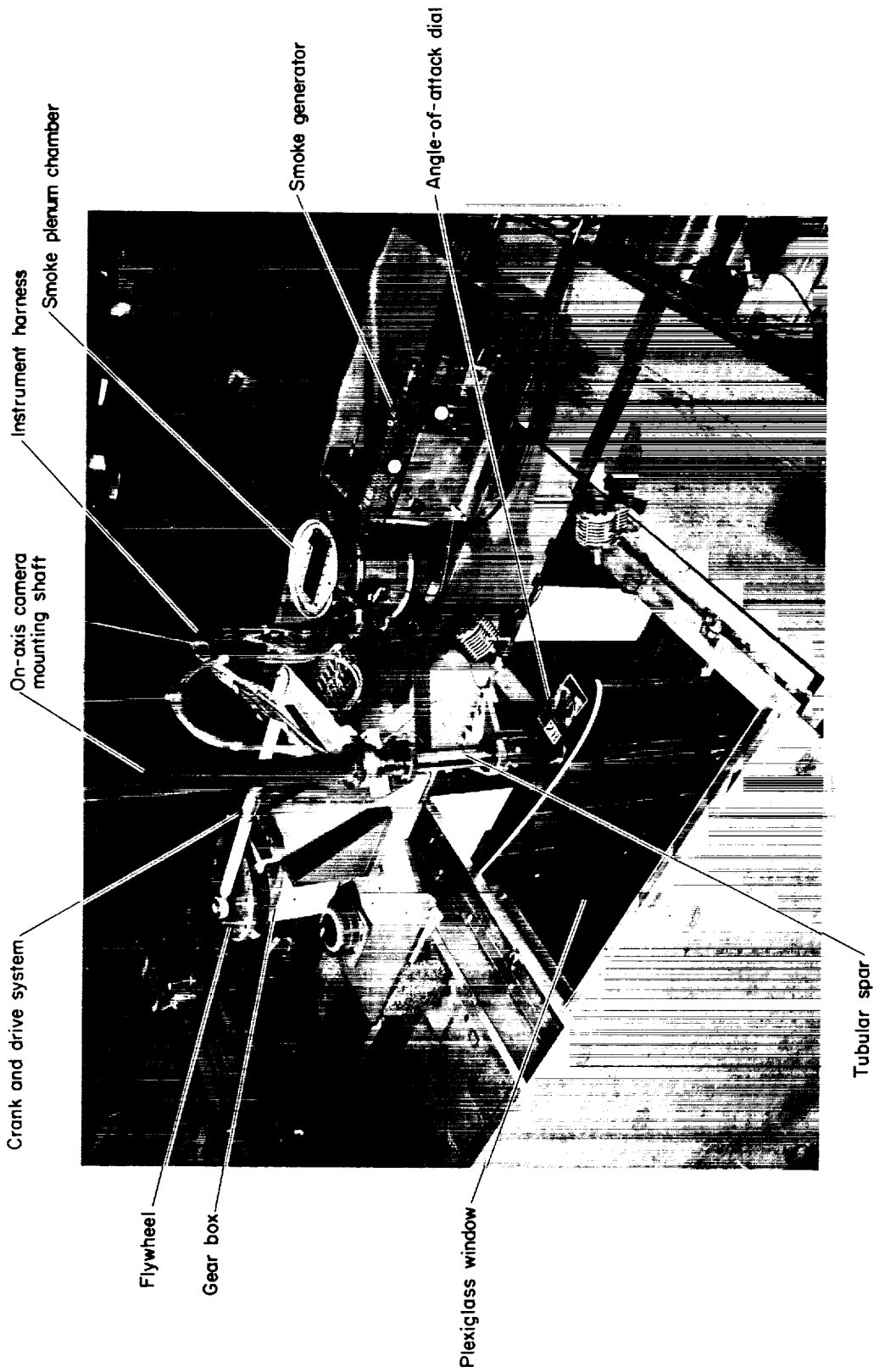
Figure 7.– Drive mechanism layout.

Hot wire probe receptacle

Local smoke flow plenum

Smoke port

Pressure transducer receptacle
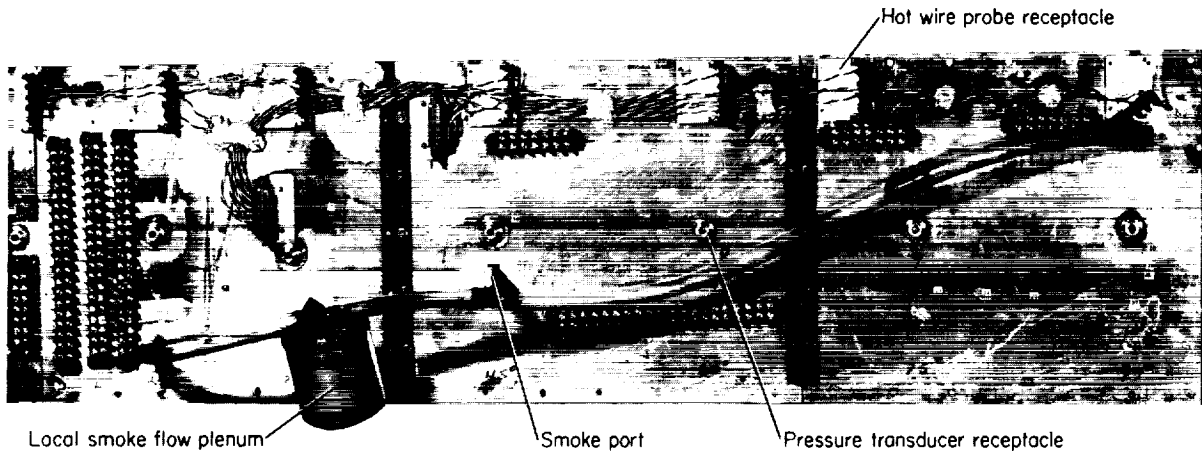
Figure 8.- View of underside of instrumented center section.

Tube to L.E. smoke port

Pressure transducer receptacles
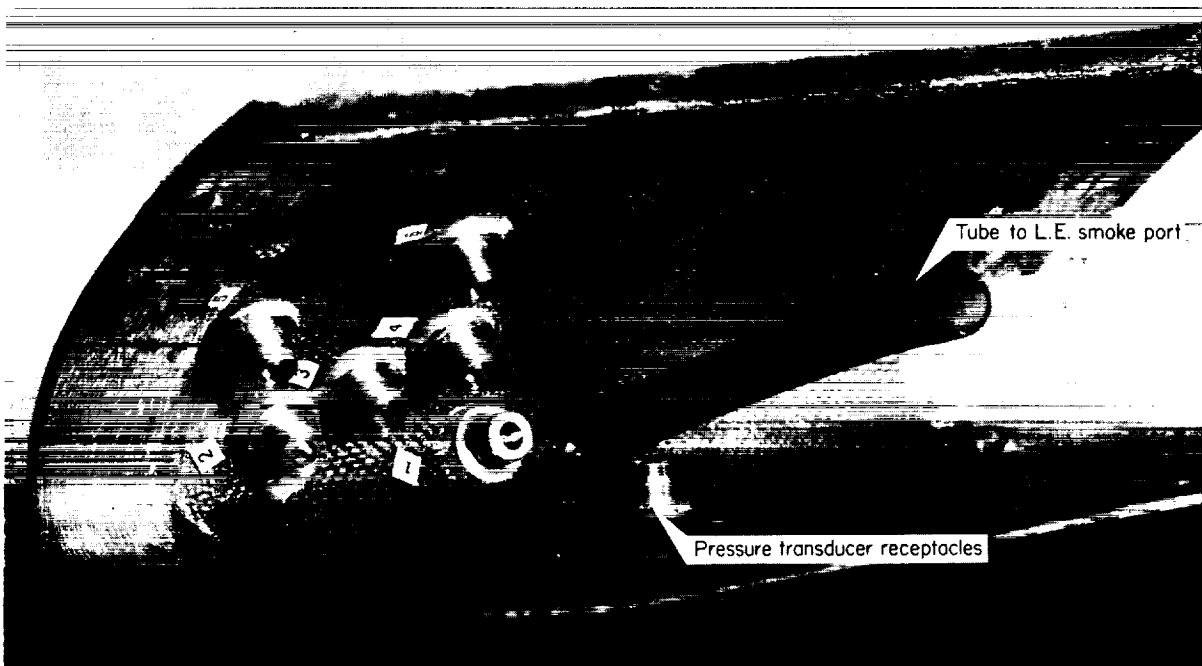
Figure 9.- View of instrumented leading-edge section.

Figure 10.- Location of stationary and on-axis high speed camera.
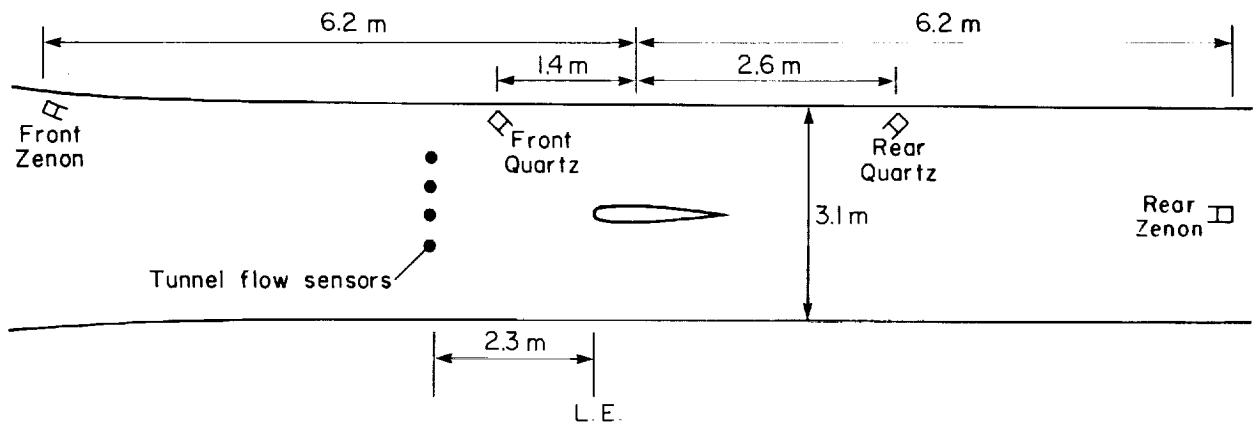
Figure 11.- Location of lights and local-tunnel-flow sensors.
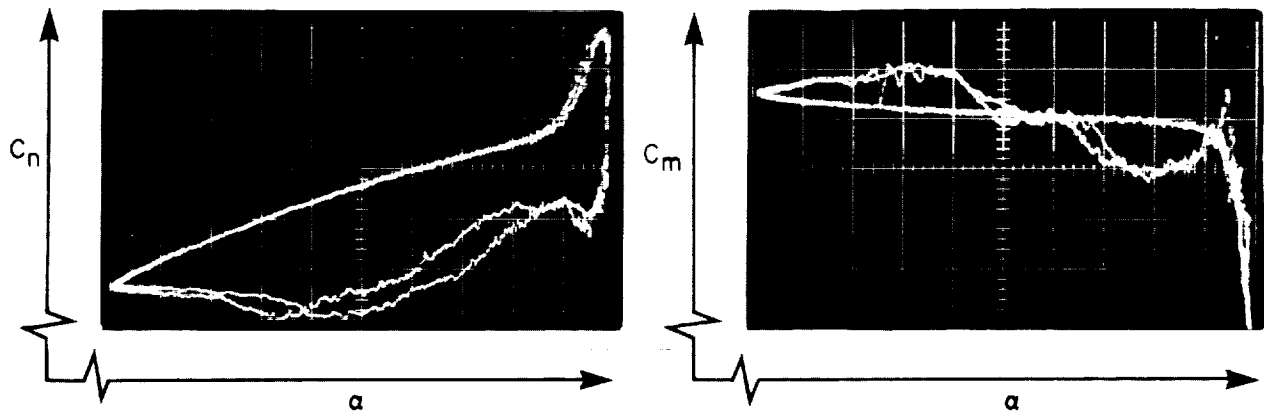
Figure 12.- On-line display of normal force and pitching moment. NACA 0012 airfoil, $\alpha = 15° + 10°$ sin ωt, k = 0.15, Re = 2.5×10^6.

Cambered Airfoil

α = 24.0°

Direction of rotation

(a)

α = 24.7°

(d)

α = 24.95°

(b)

α = 15.2°

(e)

α = 25.0°

(c)

α = 11.9°

(f)
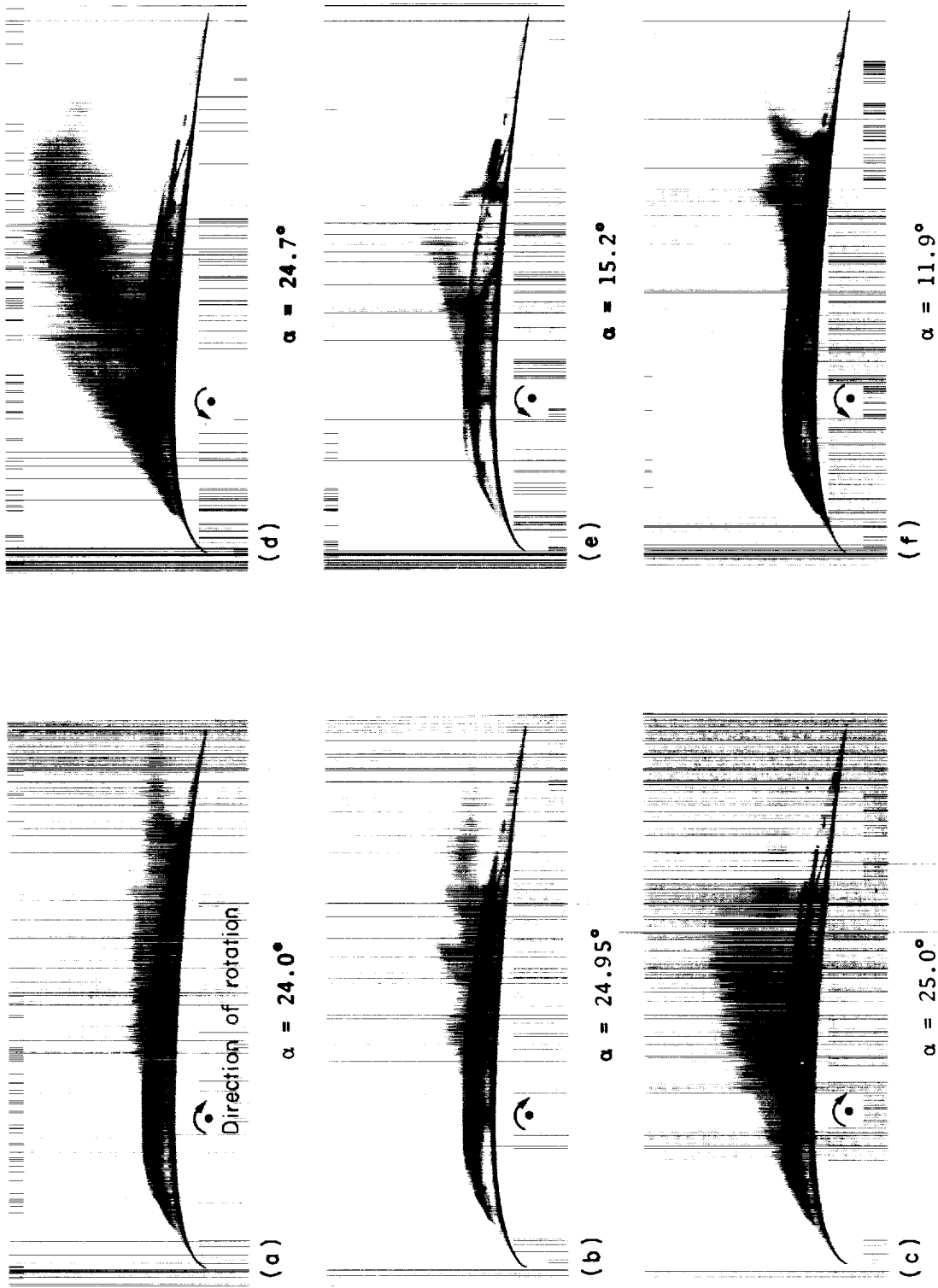
Figure 13.- Photographs of stall events on the cambered airfoil as shown by smoke-flow visualization.
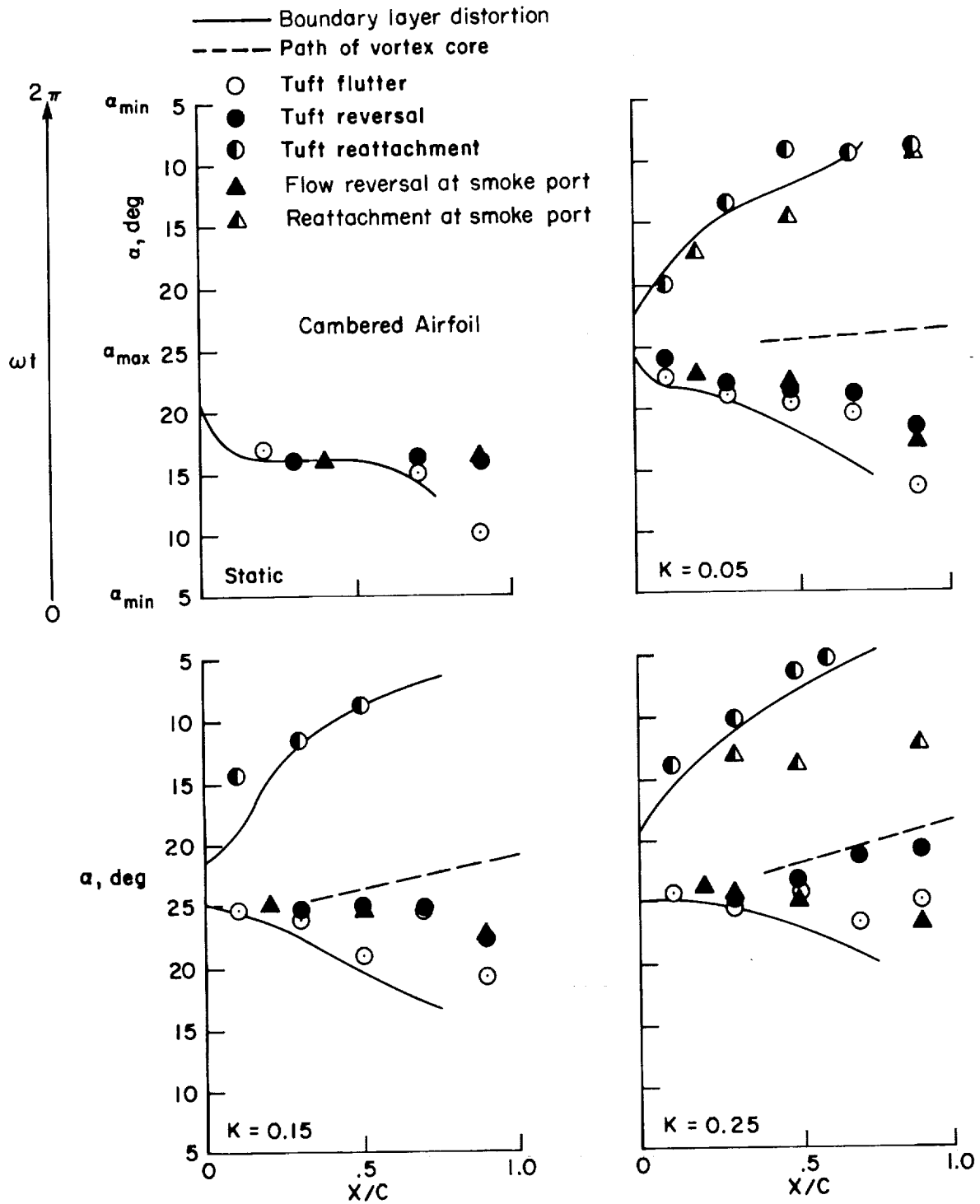
Figure 14.- Stall events on the cambered airfoil as determined by flow visualization for a range of reduced frequencies.
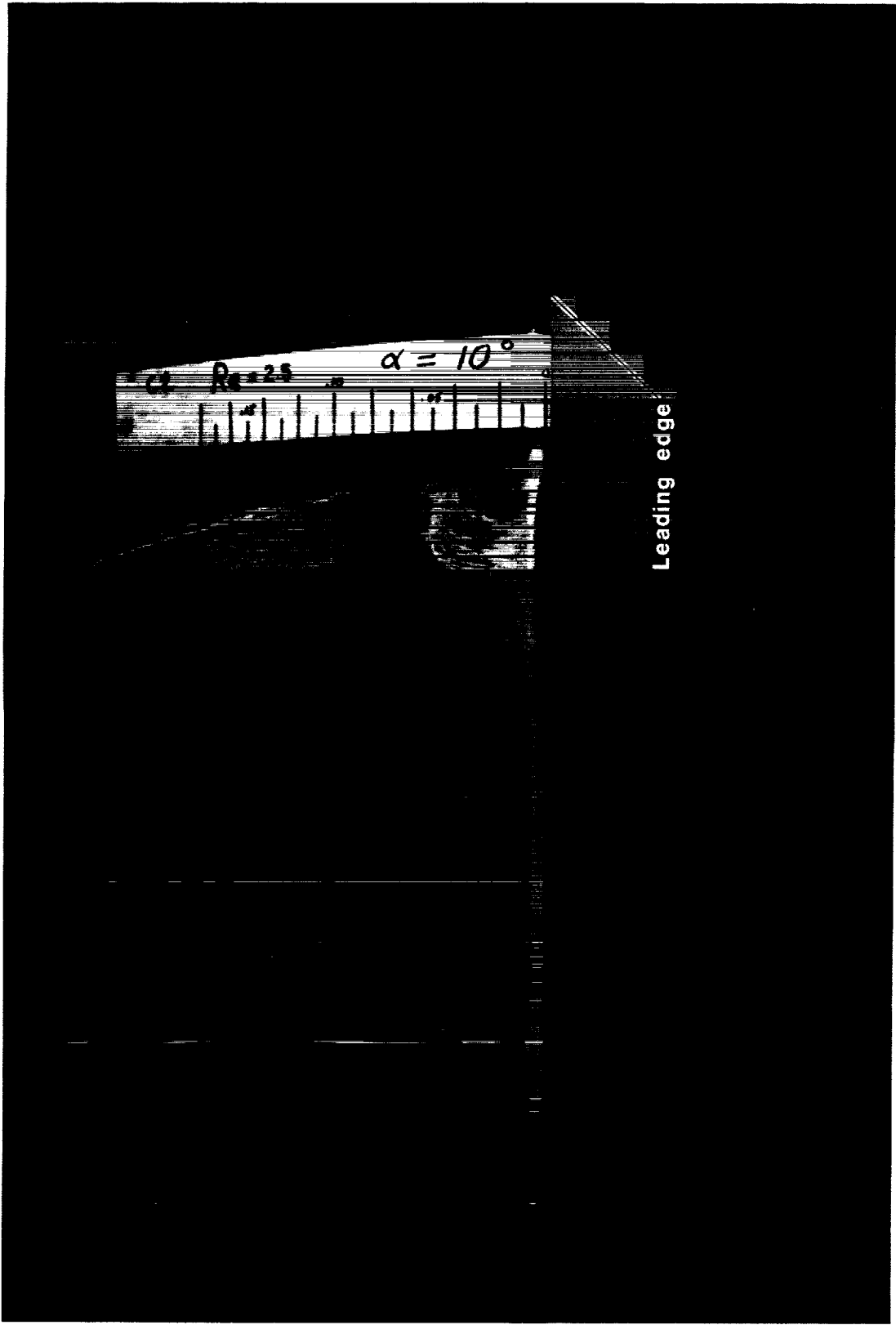
Figure 15.- Bubble near leading edge on sharp leading-edge airfoil at $\alpha = 10°$, $Re = 2.5 \times 10^6$.

Sharp L.E. Airfoil

Direction of rotation

(a) $\alpha = 14.6°$

(b) $\alpha = 15.0°$

(c) $\alpha = 16.1°$

(d) $\alpha = 19.0°$

(e) $\alpha = 10.0°$

(f) $\alpha = 7.8°$
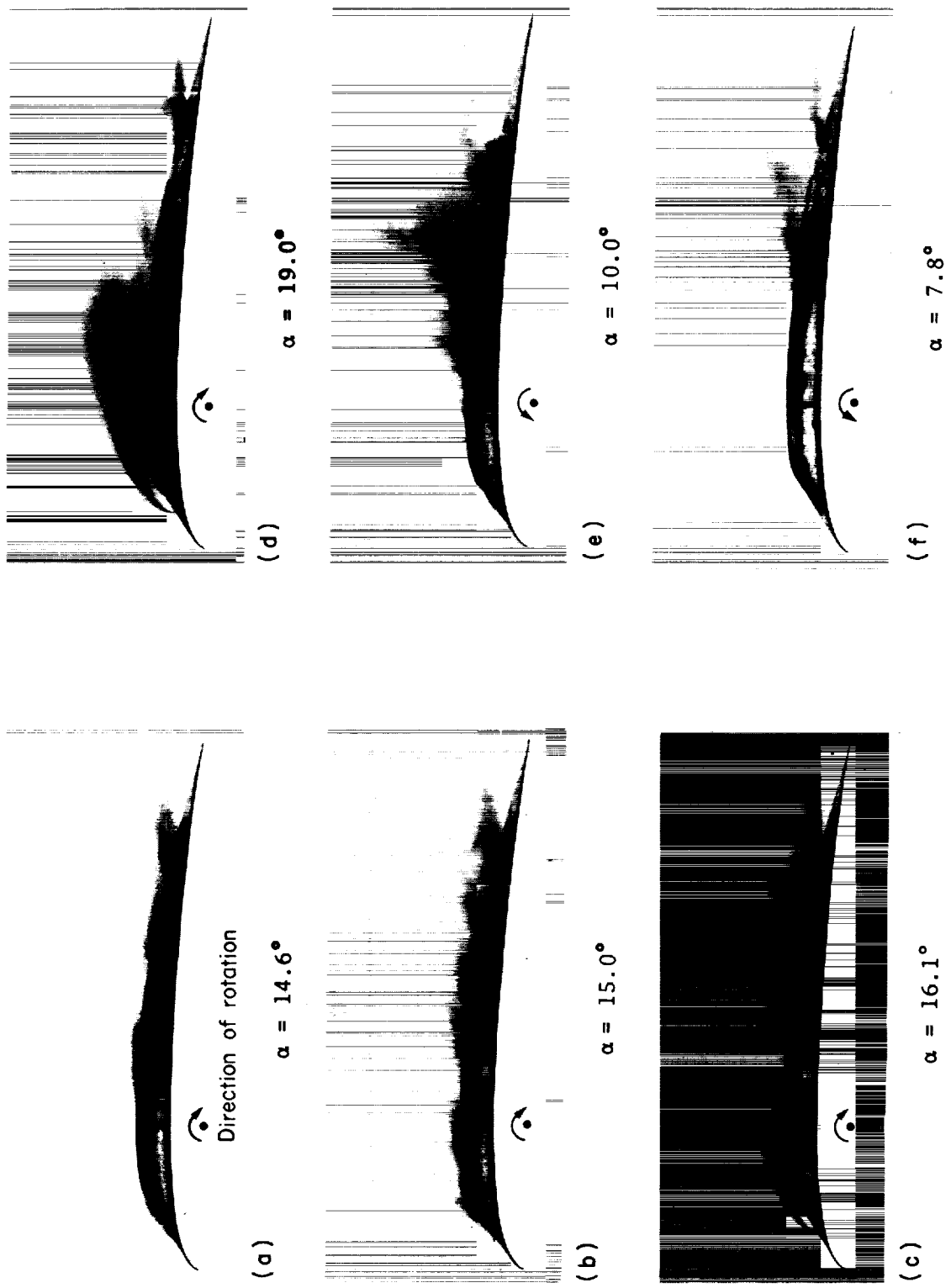
Figure 16.- Photographs of stall events on the sharp leading-edge airfoil as shown by smoke-flow visualization.
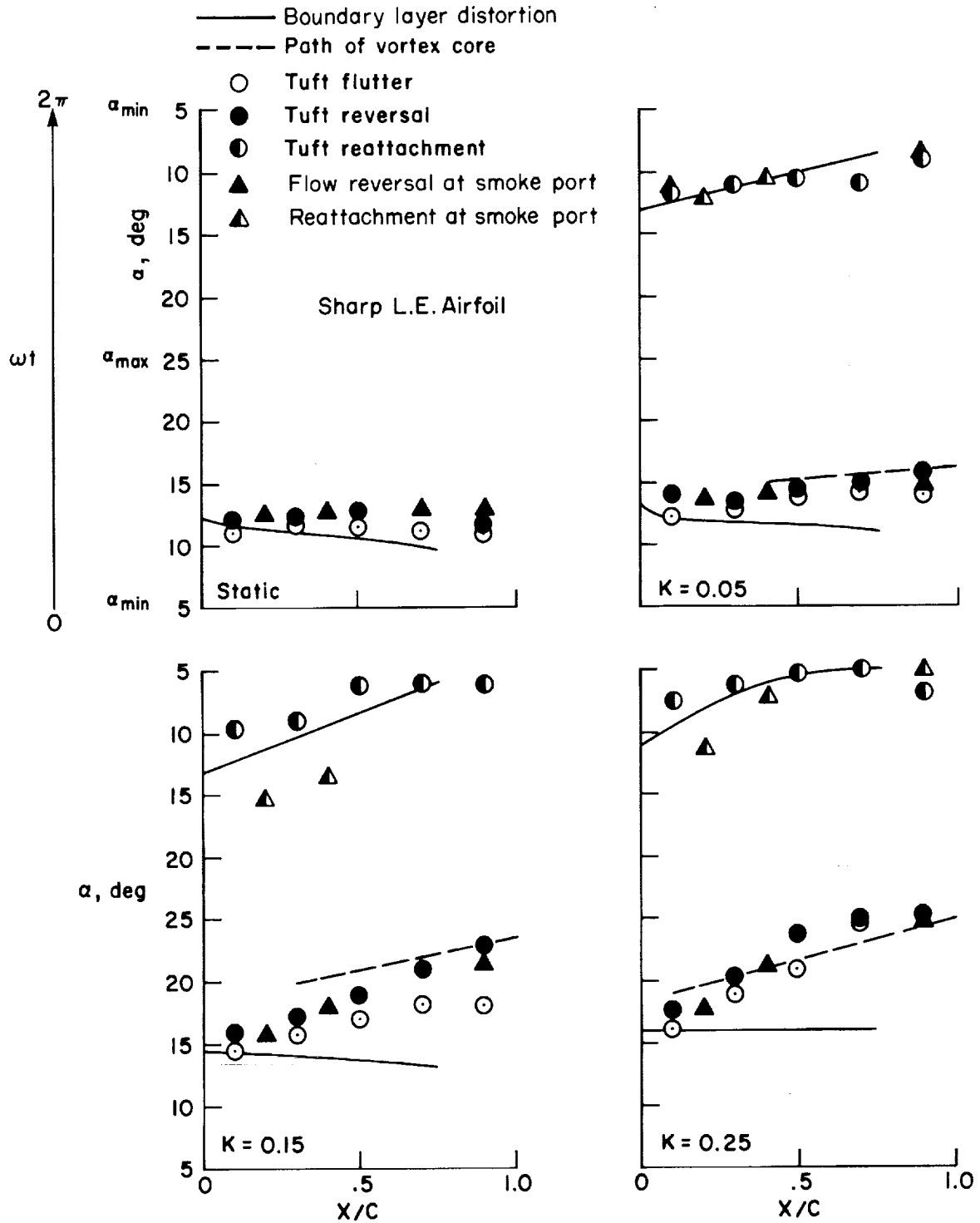
Figure 17.- Stall events on the sharp leading-edge airfoil as determined by flow visualization for a range of reduced frequencies.
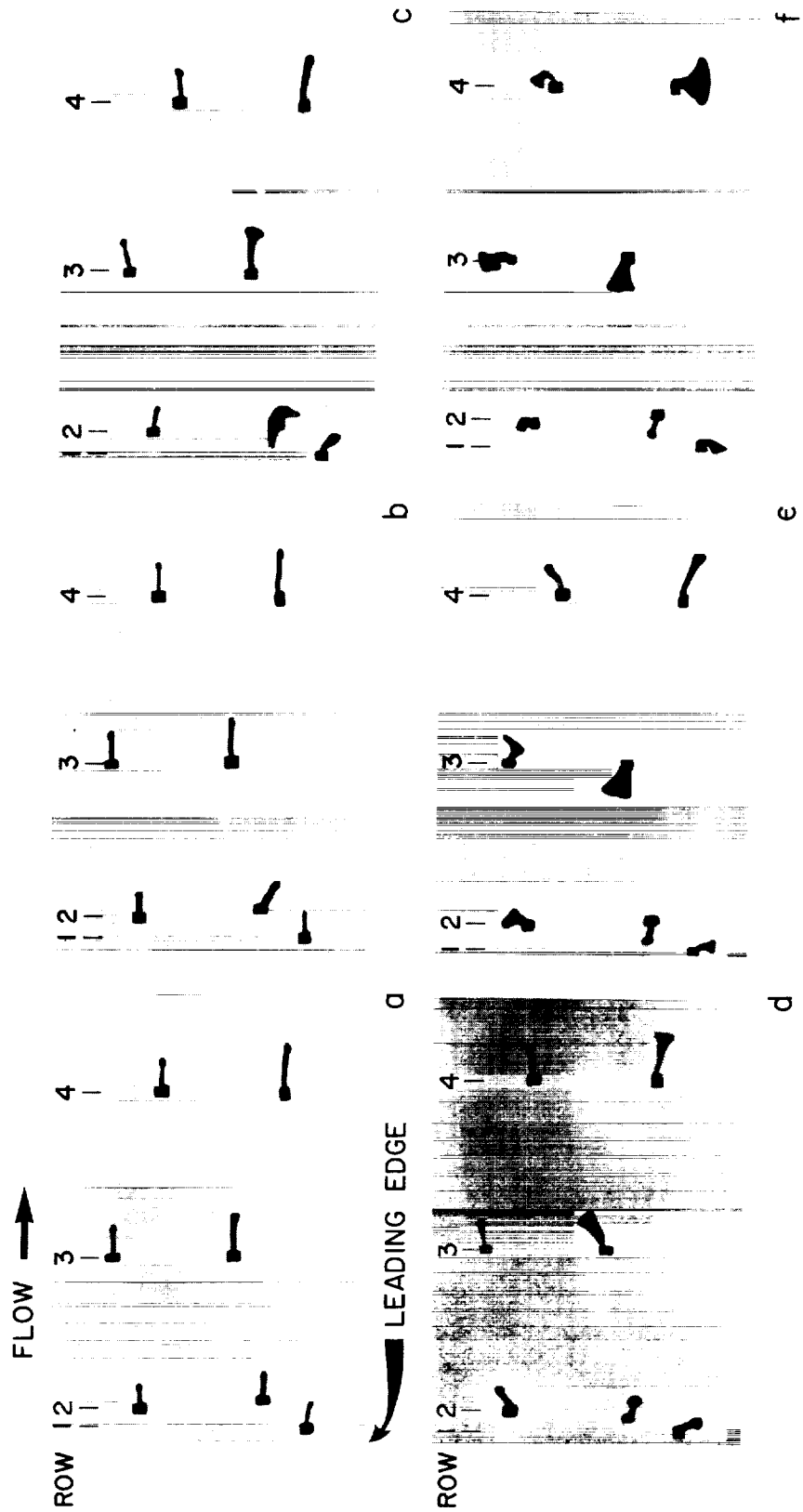
Figure 18.- Photographs of tuft behavior on the inverted cambered airfoil during dynamic stall.

55

NACA 0012 Airfoil

Direction of rotation

$\alpha = 24.0°$

(a)

$\alpha = 24.4°$

(b)

$\alpha = 24.5°$

(c)

$\alpha = 24.7°$

(d)

$\alpha = 13.8°$

(e)

$\alpha = 11.0°$

(f)
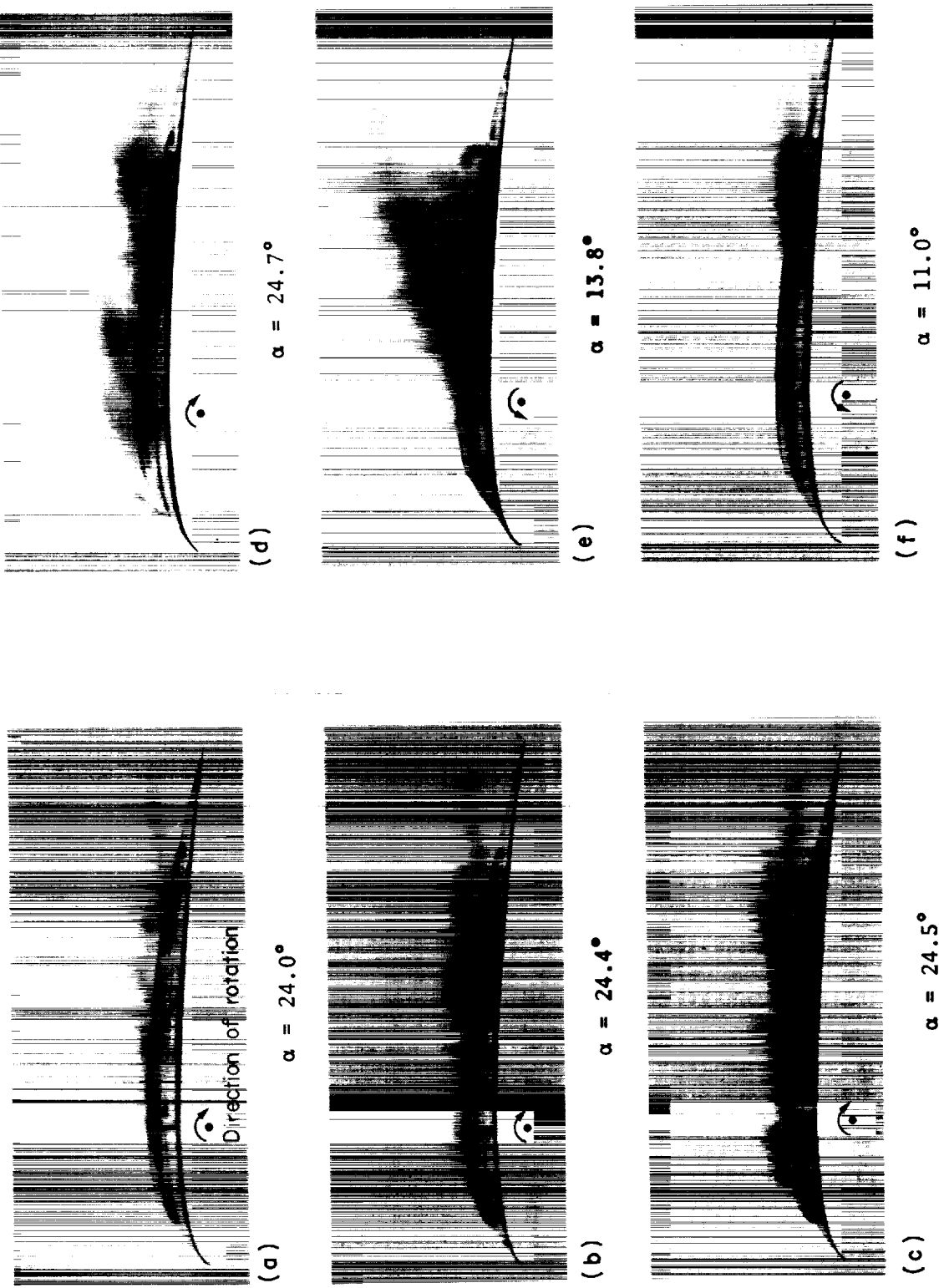
Figure 19.- Photographs of stall events on the NACA 0012 airfoil as shown by smoke-flow visualization.

56
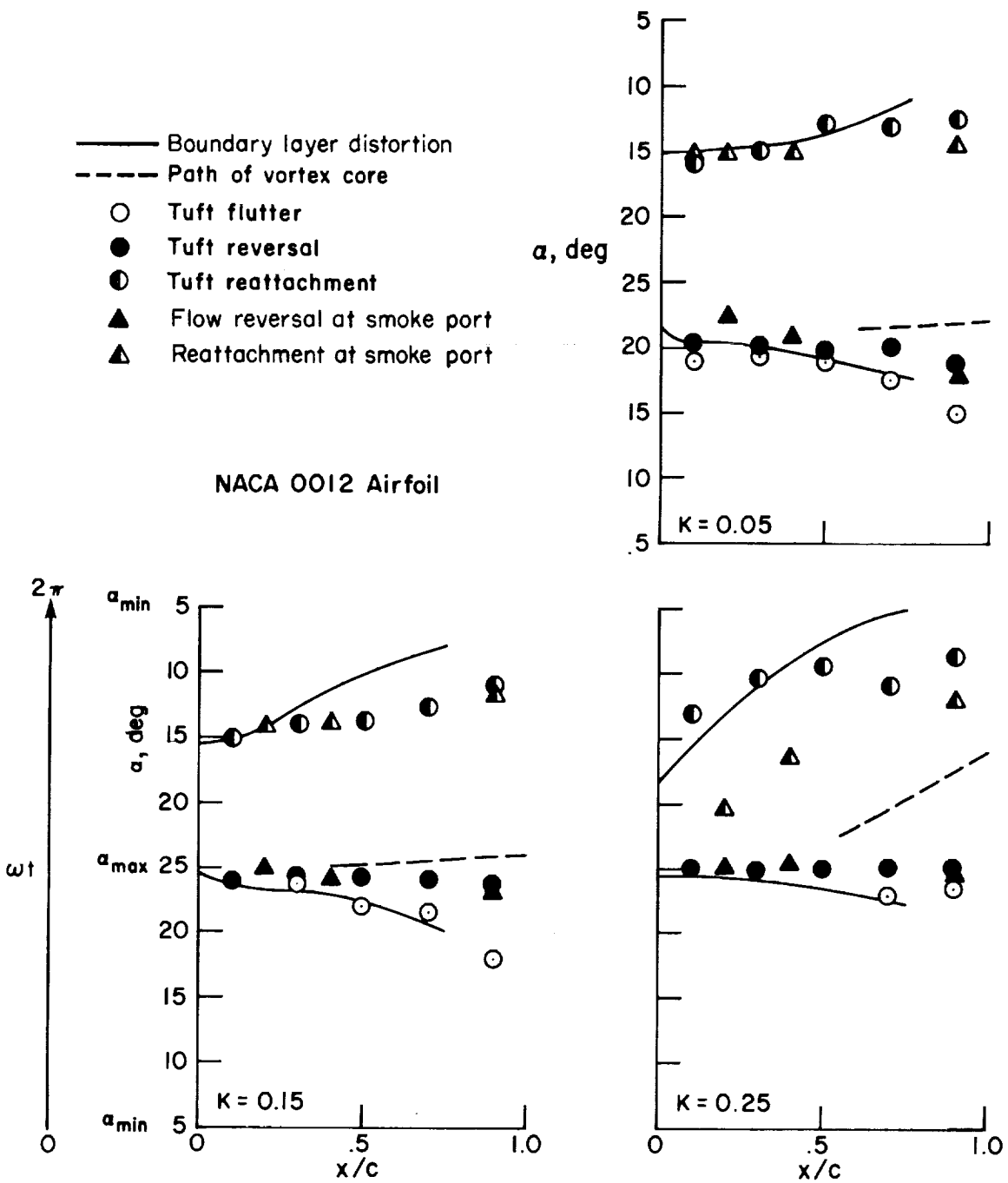
Figure 20.- Stall events on the NACA 0012 airfoil as determined by flow visualization for a range of reduced frequencies.

NACA 0012 AIRFOIL

$\alpha = 15° + 10° \sin \omega t$

$k = 0.15 \qquad Re = 2.5 \times 10^6$

I, II, III, IV Type of flow reversal
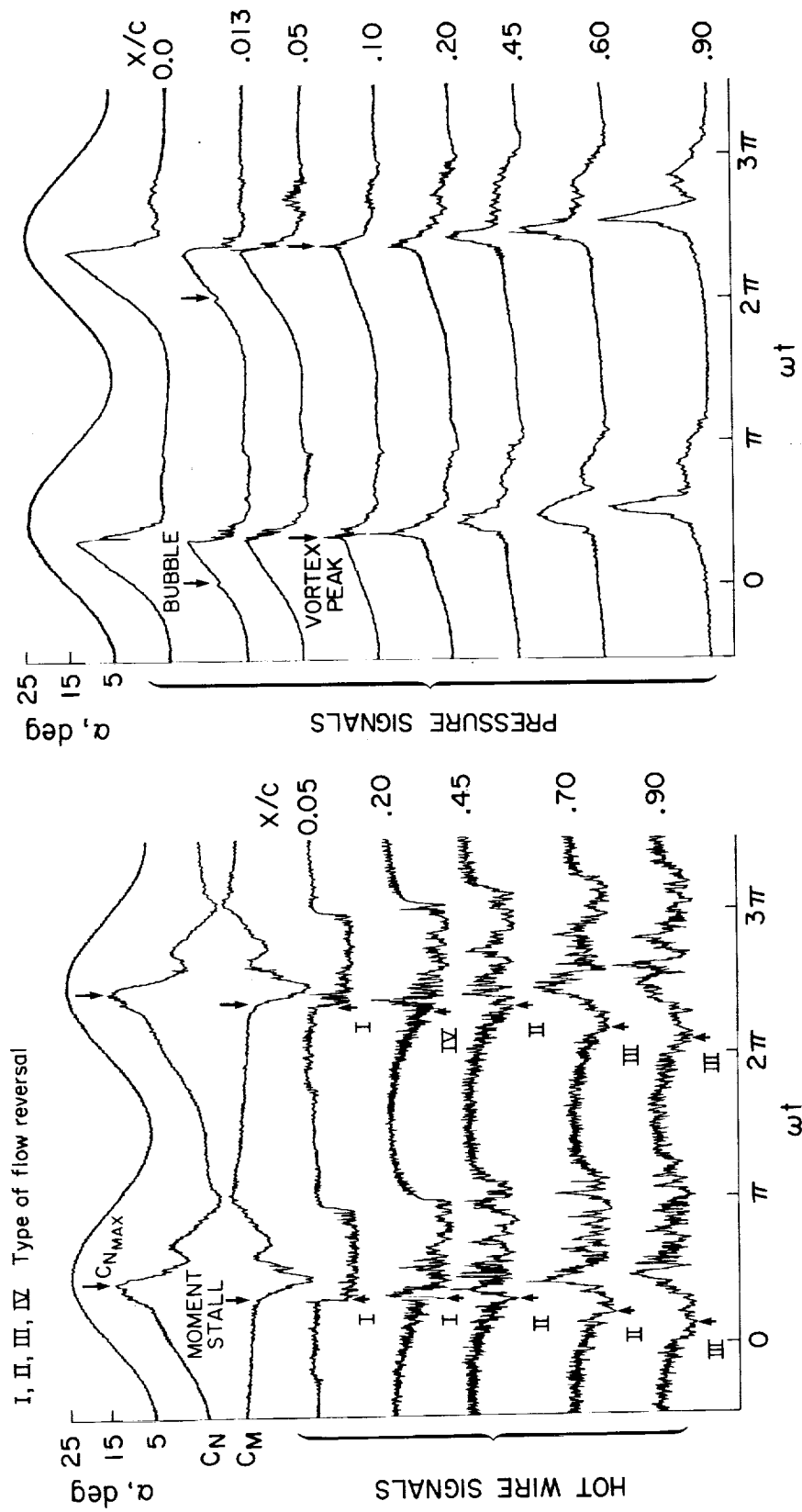
(a) Hot-wire output near airfoil surface.

(b) Pressure transducer output at airfoil surface.

Figure 21.- Representative hot-wire and pressure transducer response to dynamic stall on the NACA 0012.

58
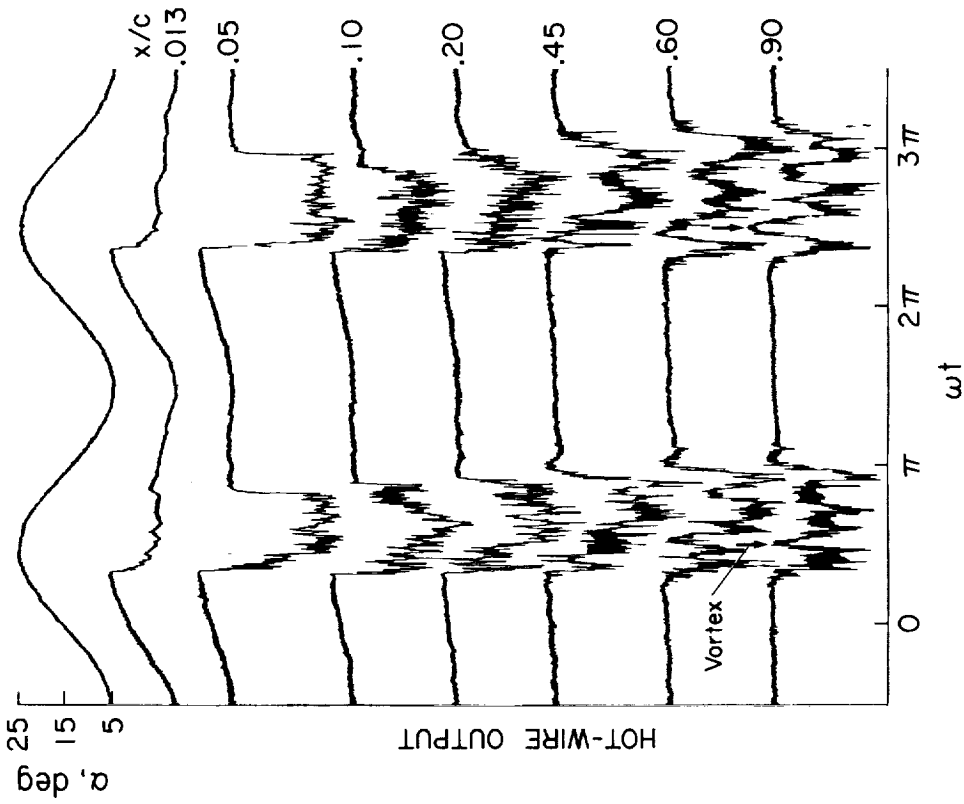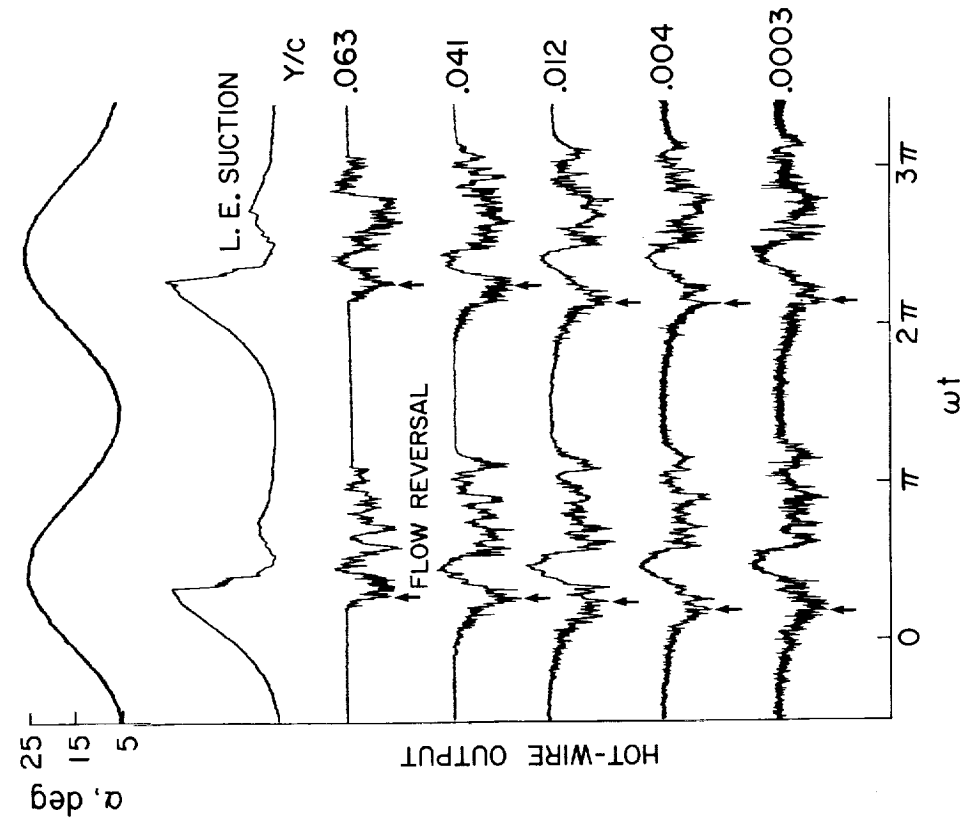
(c) Hot-wire output through the boundary layer at x/c = 0.70 (not linearized).

(d) Hot-wire output along airfoil at boundary-layer edge (not linearized).

Figure 21.- Concluded.

59
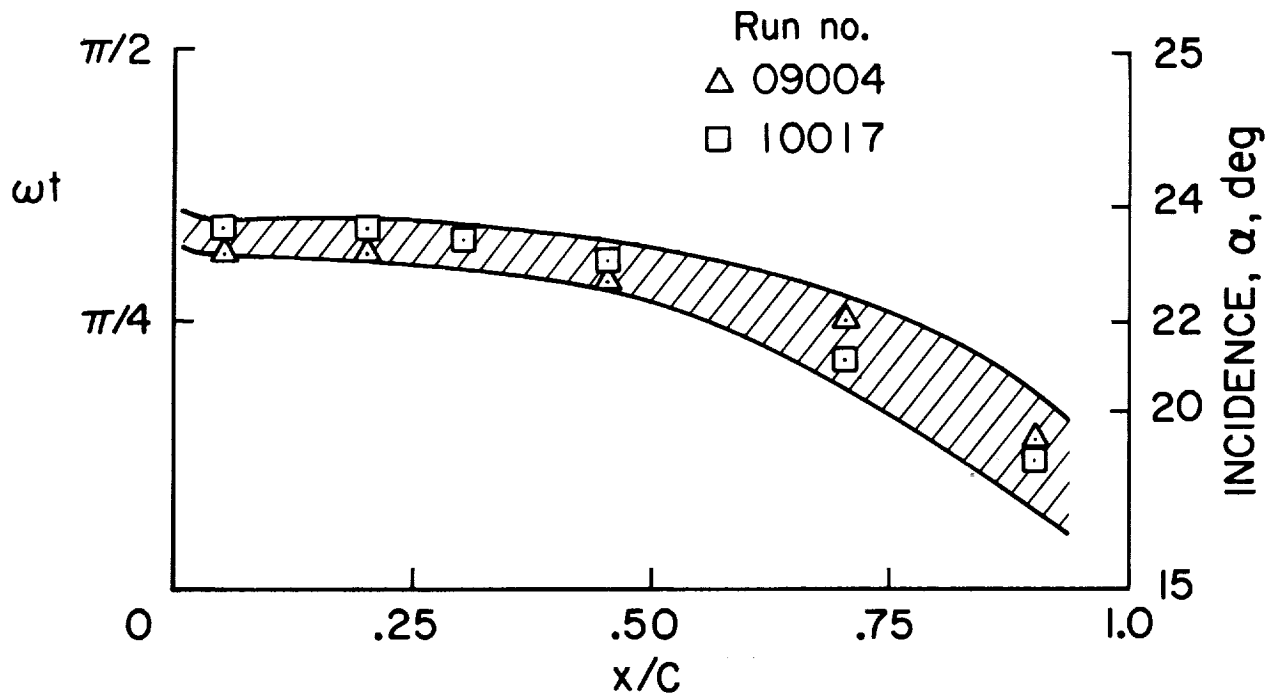
Figure 22.- Repeatability of flow-reversal measurements on the NACA 0012.
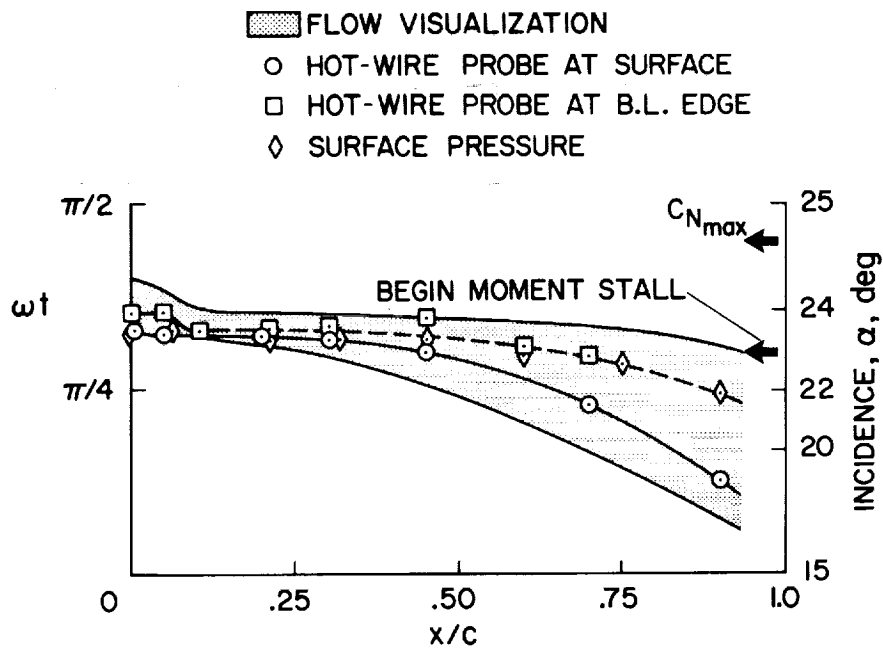
Figure 23.- Comparison of various methods for flow-reversal detection on the NACA 0012.
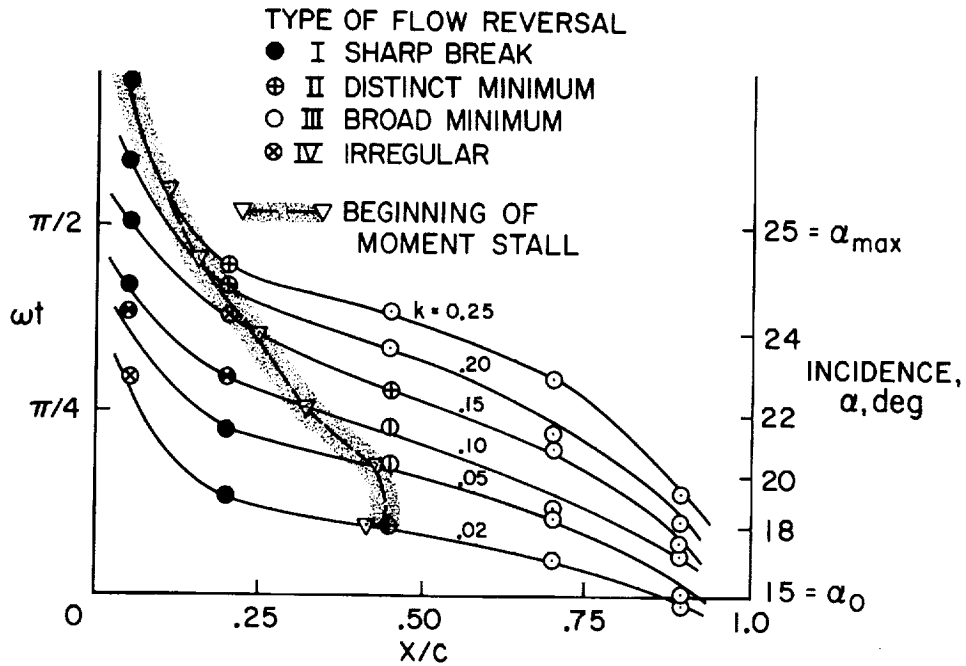
Figure 24.- Movement of the flow-reversal point as a function of incidence
angle on the cambered leading-edge airfoil as determined by hot-wire
probes.

SHARP LEADING EDGE AIRFOIL
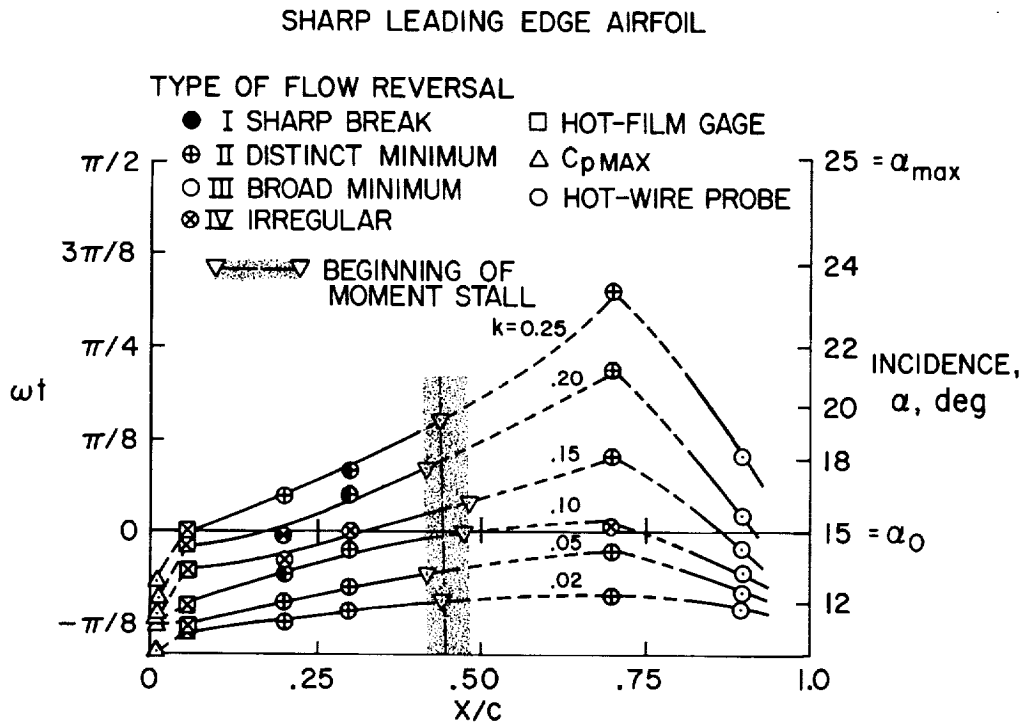
Figure 25.- Movement of the flow-reversal point as a function of incidence
angle on the sharp leading-edge airfoil as determined by hot-wire probes,
hot-film sensors, and pressure transducers.

61

NACA 0012 AIRFOIL

TYPE OF FLOW REVERSAL
● I SHARP BREAK
⊕ II DISTINCT MINIMUM
○ III BROAD MINIMUM
⊗ IV IRREGULAR

▽═══▽ BEGINNING OF MOMENT STALL

$\pi/2$

ωt

$\pi/4$

k=0.25
.20
.15
.10
.05
.02

$25 = \alpha_{max}$

24

INCIDENCE, α, deg

22

20

18

$15 = \alpha_0$

0   .25   .50   .75   1.0

X/C
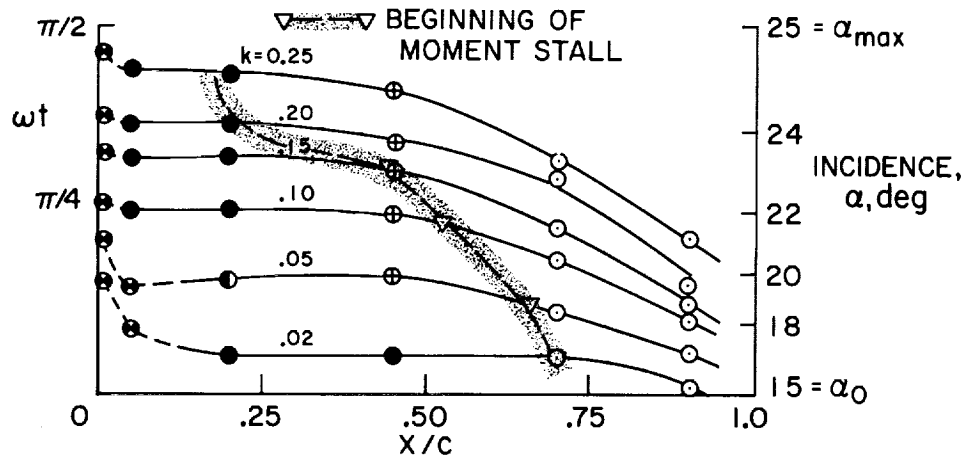
Figure 26.- Movement of the flow-reversal point as a function of incidence angle on the NACA 0012 airfoil as determined by hot-wire probes.

THE EVENTS OF
DYNAMIC STALL ON
THE NACA 0012 AIRFOIL
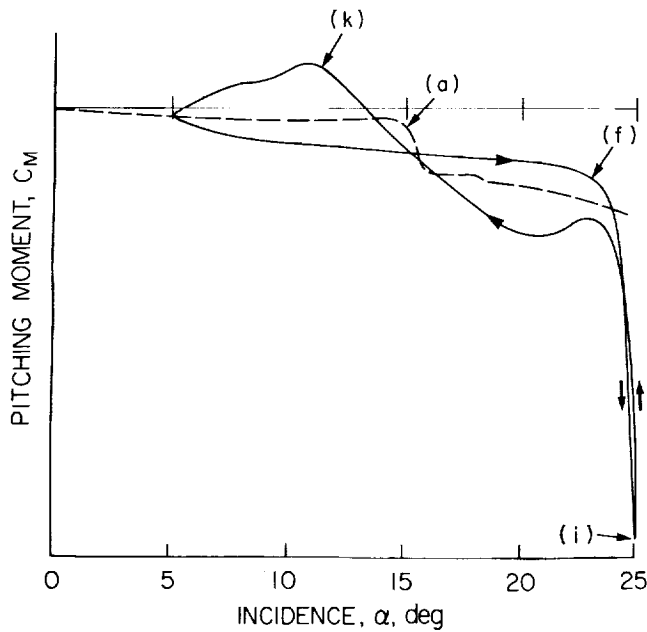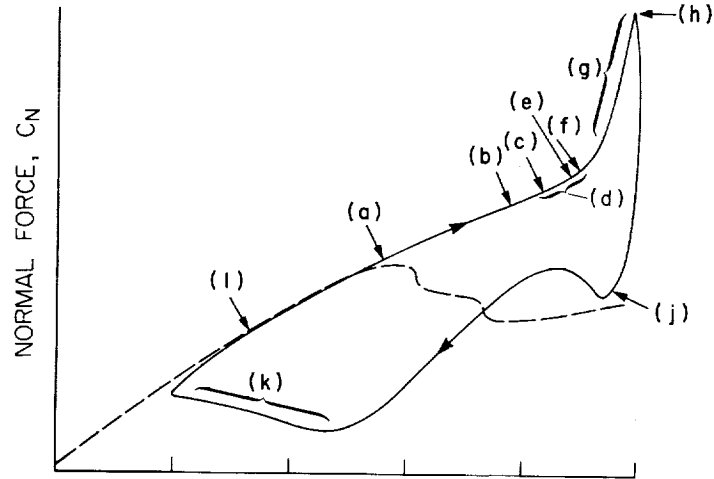
(a) STATIC STALL ANGLE EXCEEDED

(b) FIRST APPEARANCE OF FLOW
REVERSAL ON SURFACE

(c) LARGE EDDIES APPEAR IN
BOUNDARY LAYER

(d) FLOW REVERSAL SPREADS OVER
MUCH OF AIRFOIL CHORD

(e) VORTEX FORMS NEAR
LEADING EDGE

(f) LIFT SLOPE INCREASES

(g) MOMENT STALL OCCURS

(h) LIFT STALL BEGINS

(i) MAXIMUM NEGATIVE MOMENT

(j) FULL STALL

(k) BOUNDARY LAYER REATTACHES
FRONT TO REAR

(l) RETURN TO UNSTALLED VALUES

Figure 27.- Dynamic stall events on NACA 0012 airfoil.
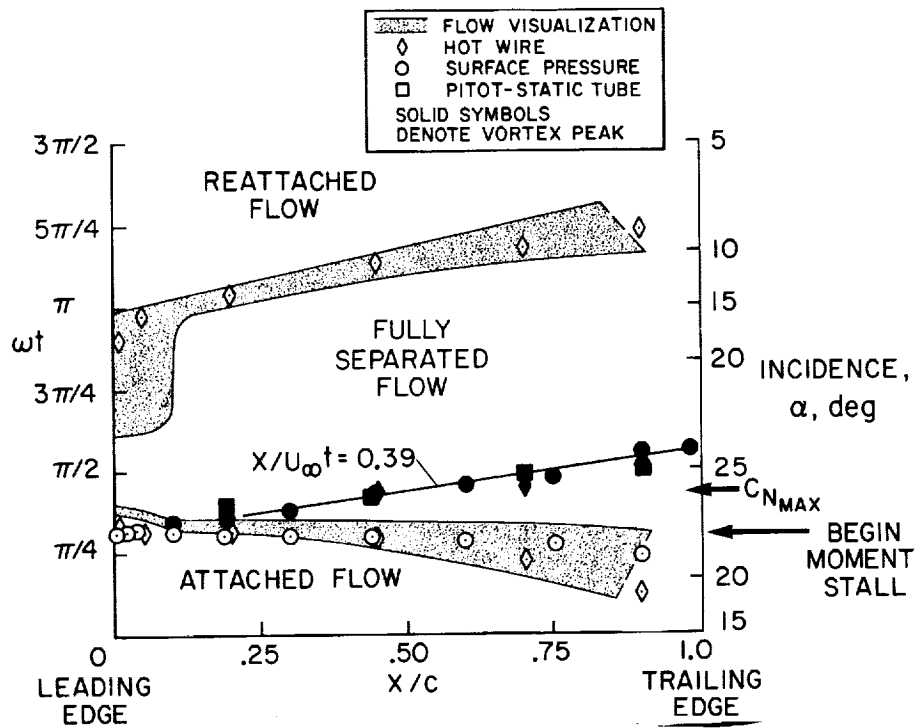
Figure 28.- Development of dynamic stall on the NACA 0012 as determined by various detection devices.
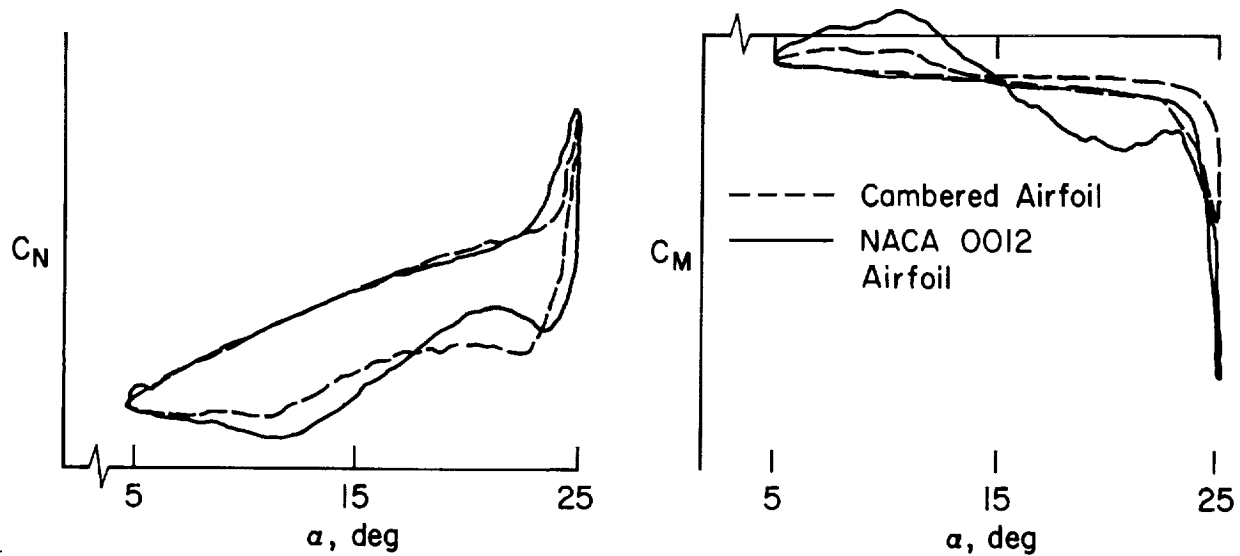
Figure 29.- Normal force and pitching moment on the cambered airfoil at
k = 0.15, α = 15° + 10° sin ωt and Re = 2.5×10⁶.
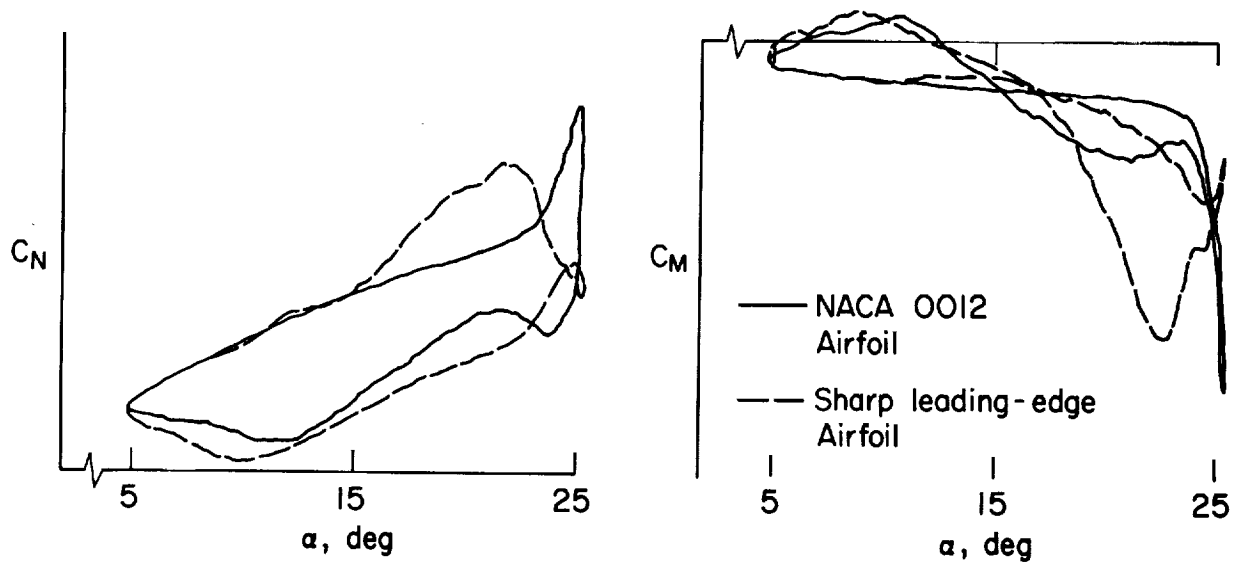
Figure 30.- Normal force and pitching moment on the sharp leading-edge airfoil
at k = 0.15, α = 15° + 10° sin ωt, Re = 2.5×10⁶.
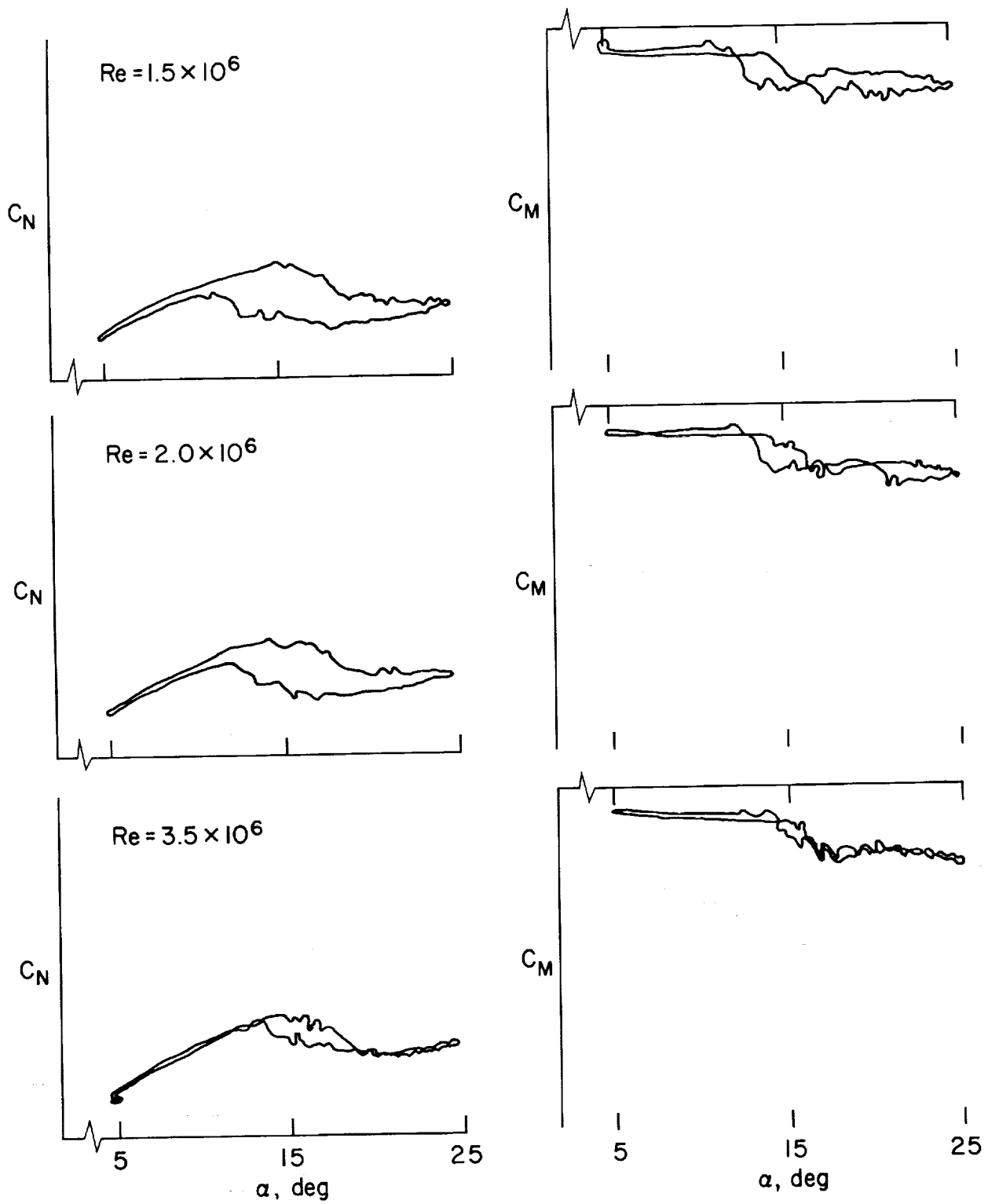
Figure 31.- Normal force and pitching moment on NACA 0012 airfoil at k = 0.004; α = 15° + 10° sin ωt; Re = 1.5, 2.0, 3.5×10⁶.
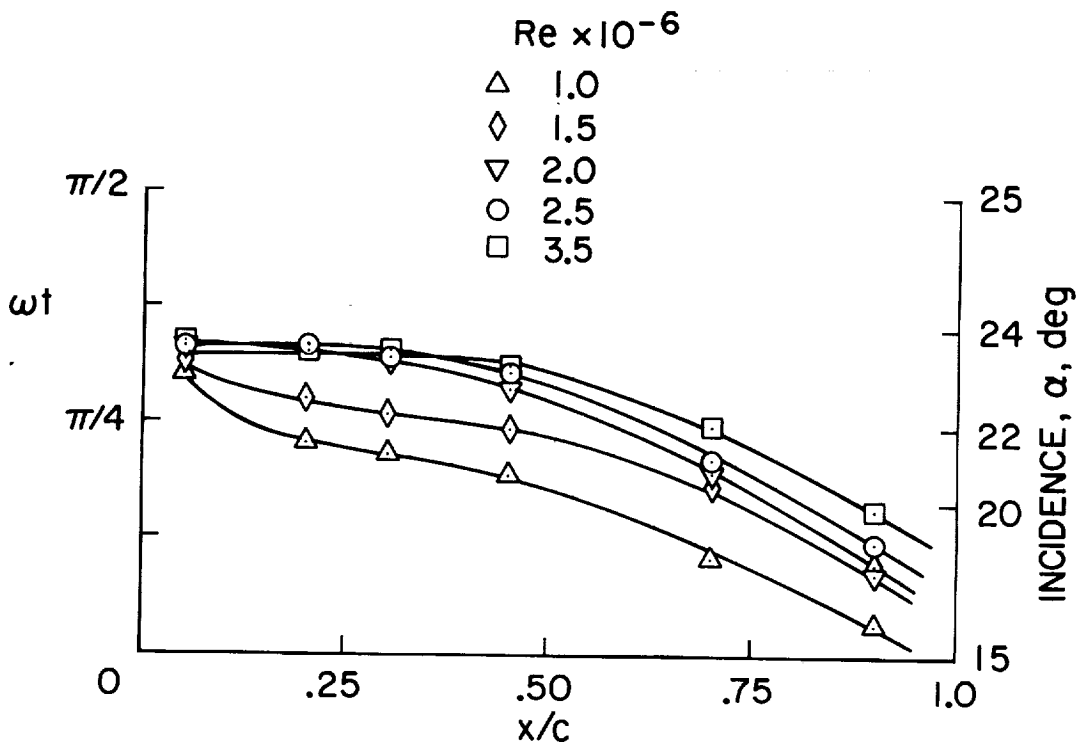
Figure 32.- Locus of flow reversal on the NACA 0012 as a function of Reynolds number as determined by hot-wire probes.

Boundary layer distortion
Path of vortex core
○ Tuft flutter
● Tuft reversal
◐ Tuft reattachment
▲ Flow reversal at smoke port
△ Reattachment at smoke port

α, deg

Re = 1.5 × 10⁶

NACA 0012 Airfoil

2π

α_{min}

α, deg

ωt

α_{max}

α_{min}

Re = 2.5 × 10⁶

Re = 3.5 × 10⁶

X/C

X/C
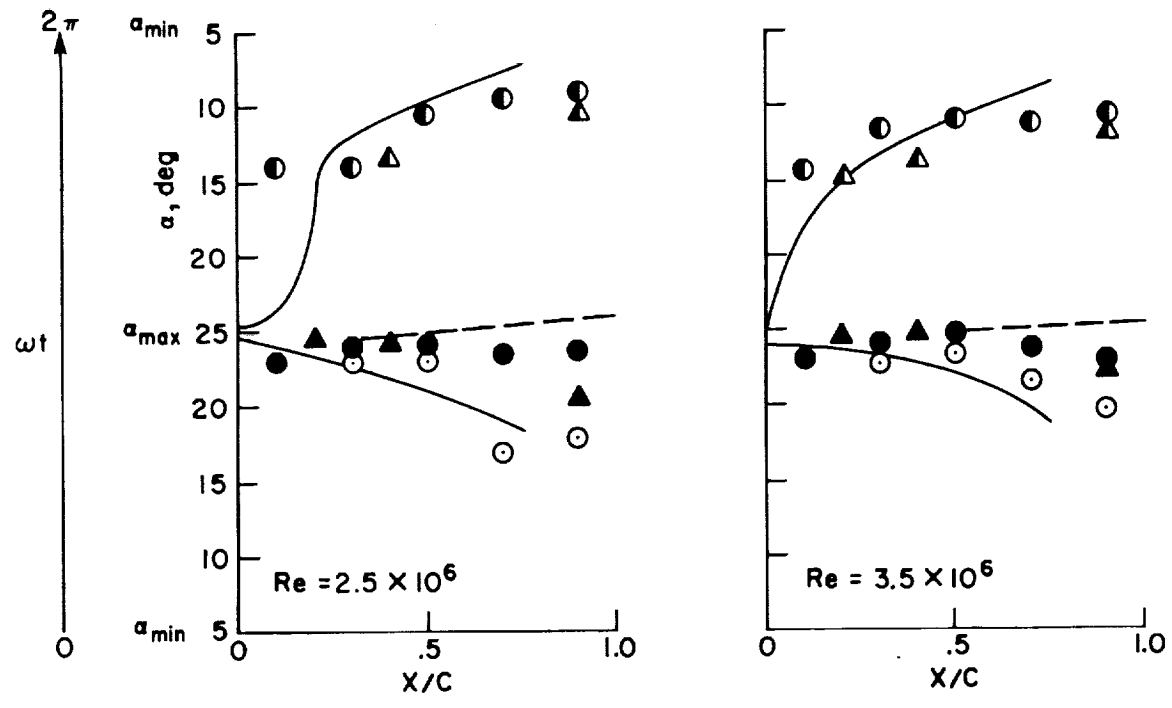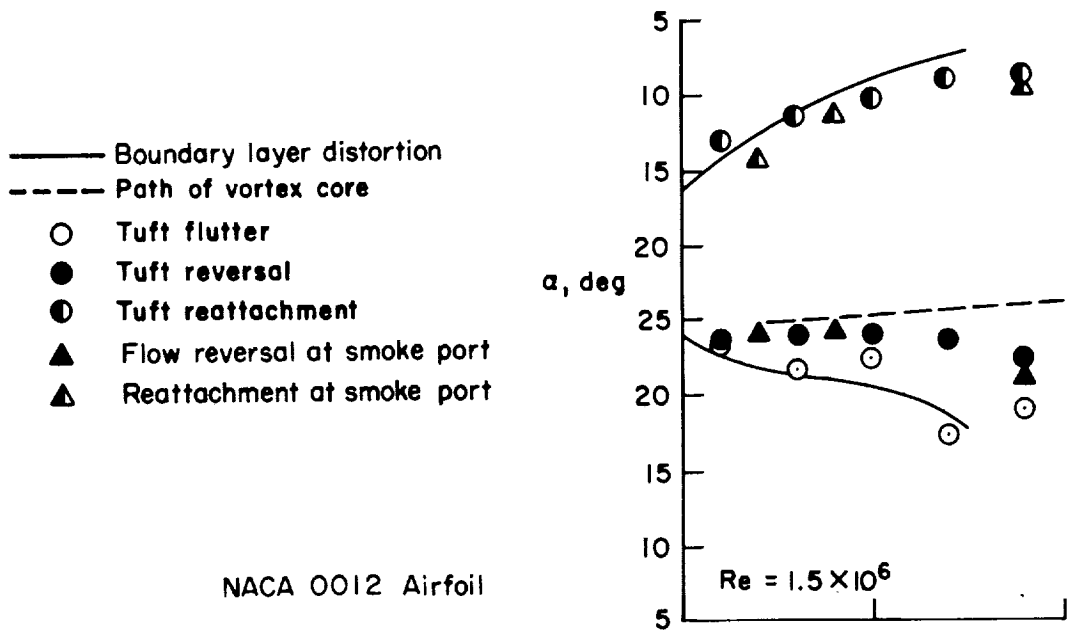
Figure 33.- Stall events on the NACA 0012 for a range of Reynolds number as determined by flow visualization.
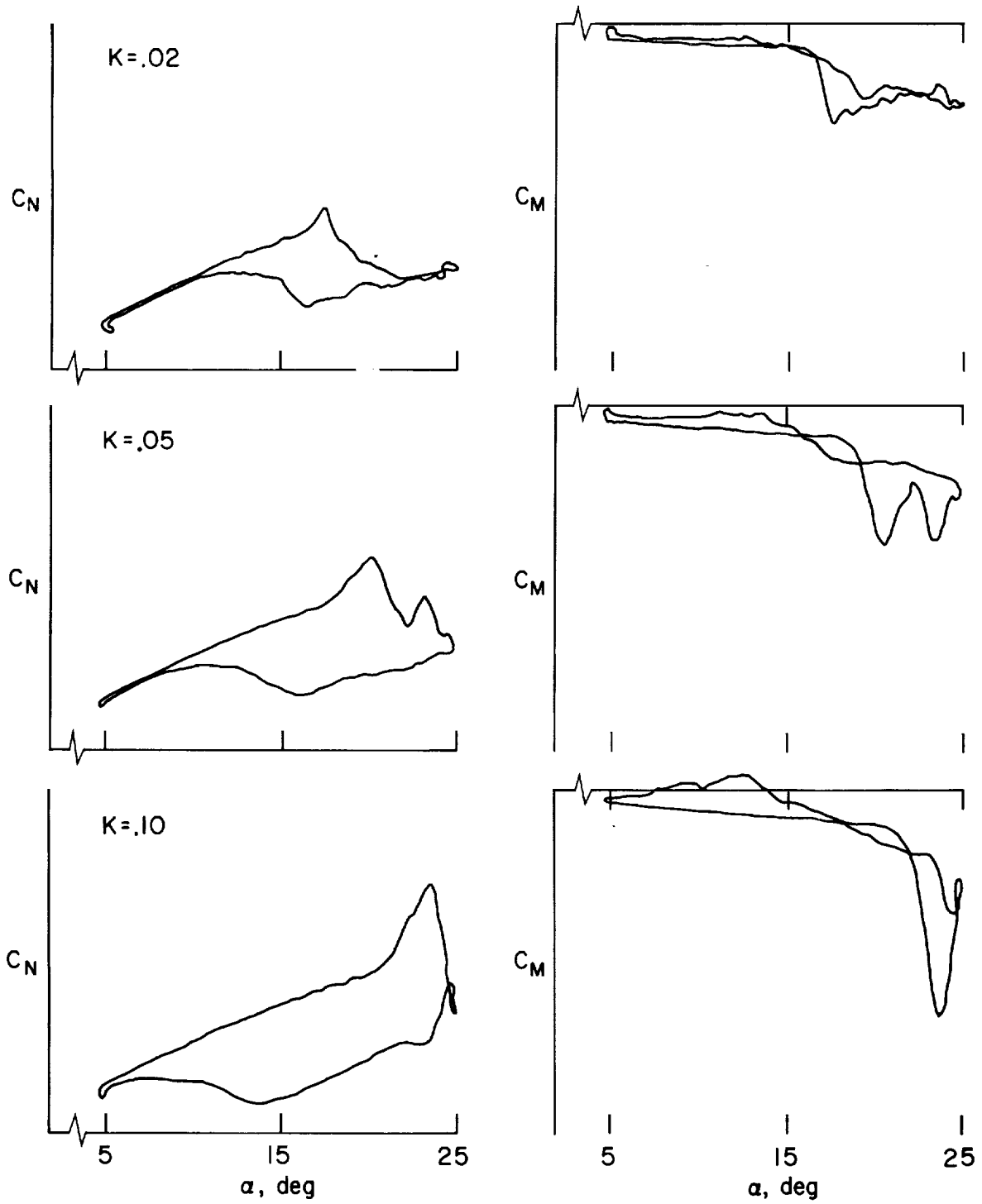
(a) k = 0.02, 0.05, 0.10

Figure 34.- Normal force and pitching moment on NACA 0012 at
$\alpha = 15° + 10° \sin \omega t$, Re $= 2.5 \times 10^6$.
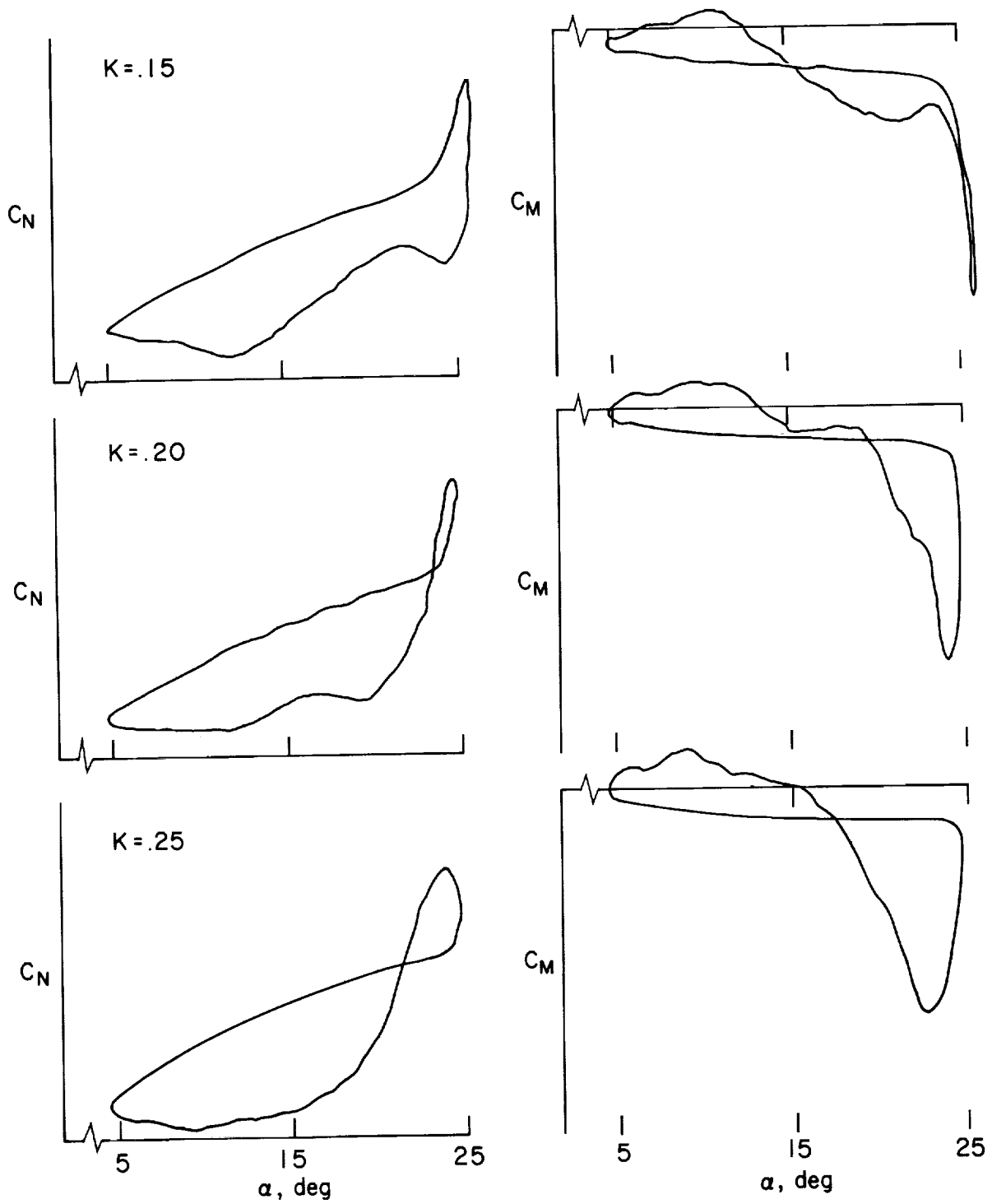
(b) k = 0.15, 0.20, 0.25

Figure 34.- Concluded.
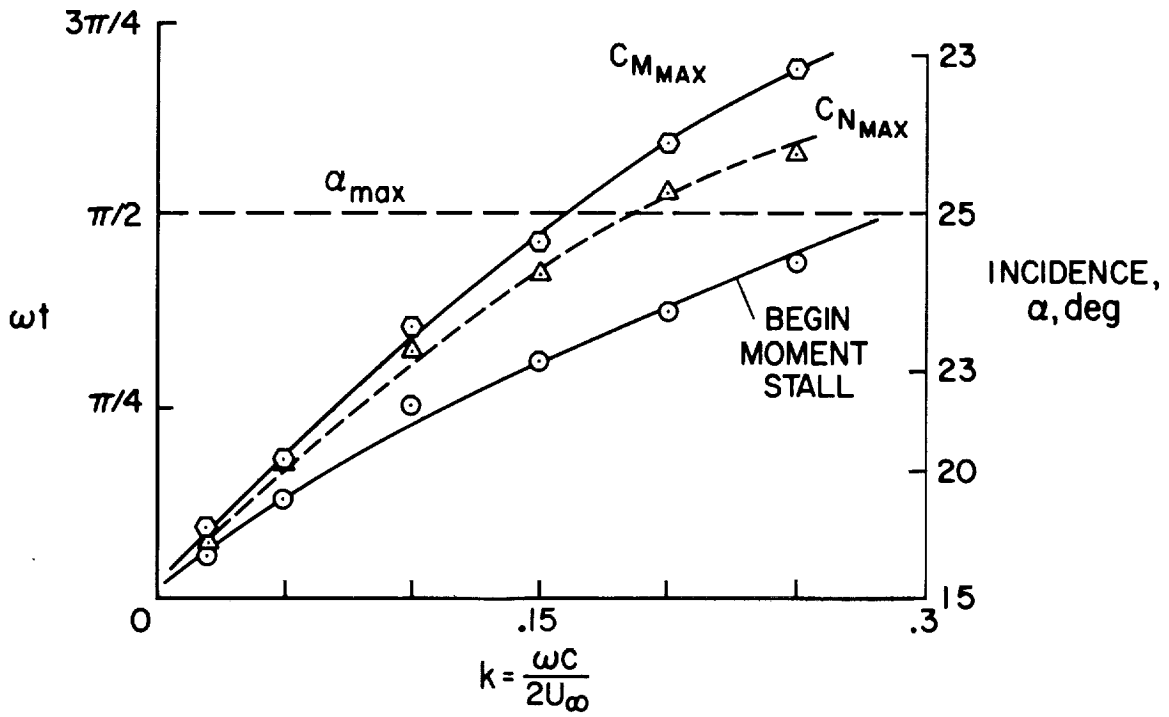
Figure 35.- Maximum force and moment coefficient dependence on reduced frequency for the NACA 0012.
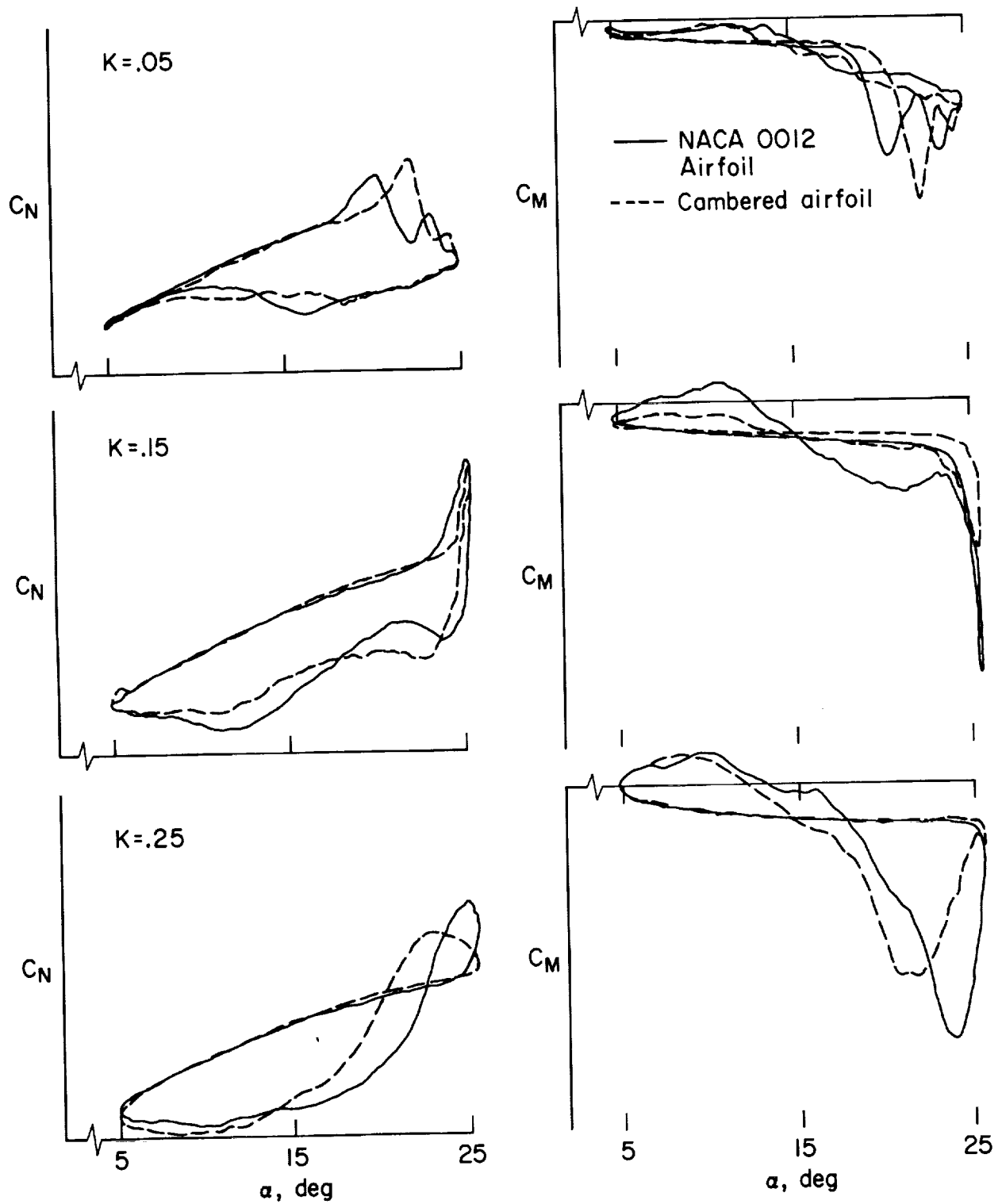
Figure 36.— Normal force and pitching moment on cambered airfoil at k = 0.05, 0.15, 0.25; α = 15° + 10° sin ωt; Re = 2.5×10⁶.
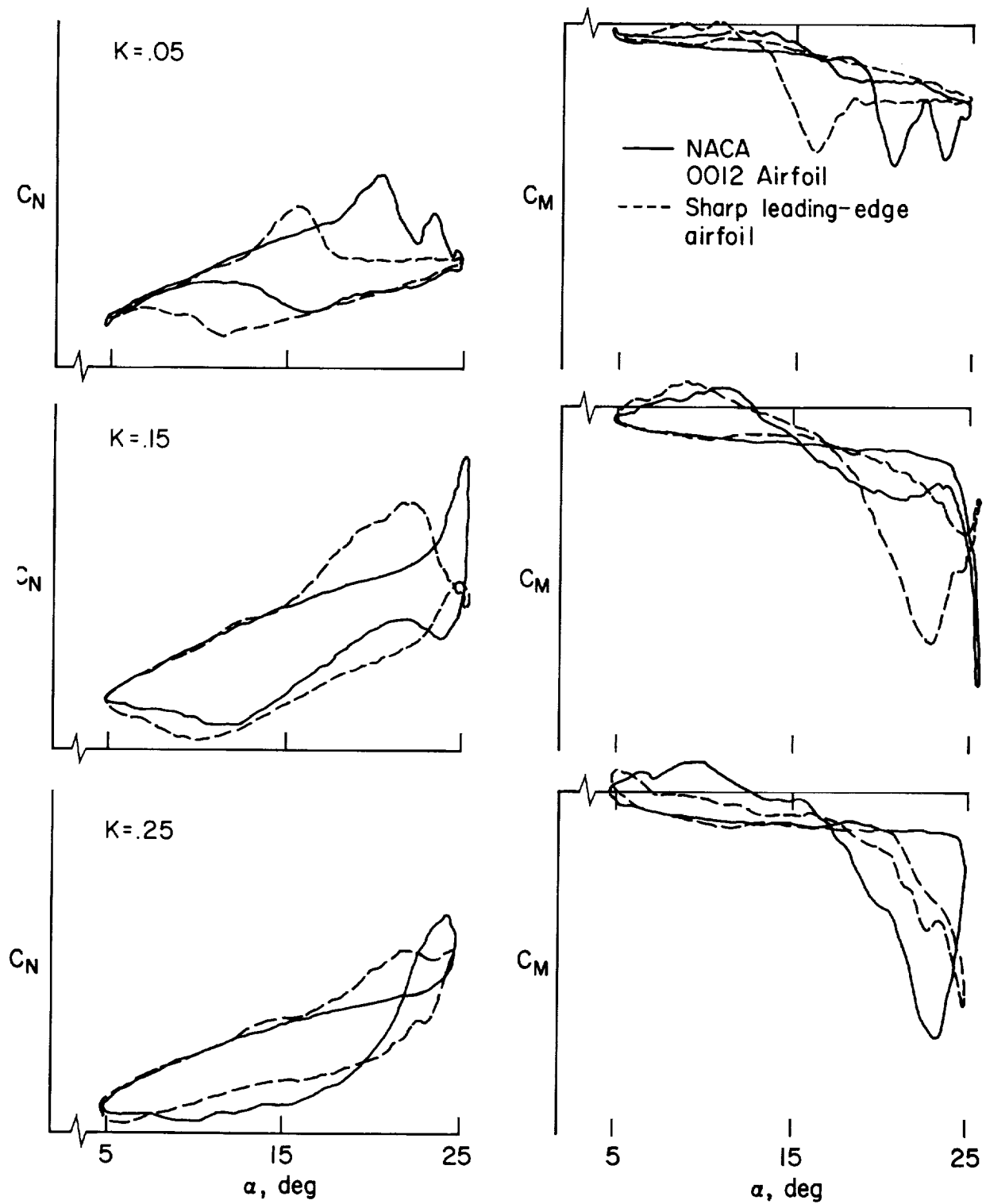
Figure 37.- Normal force and pitching moment on sharp leading-edge airfoil at
k = 0.05, 0.15, 0.25; α = 15° + 10° sin ωt; Re = 2.5×10⁶.
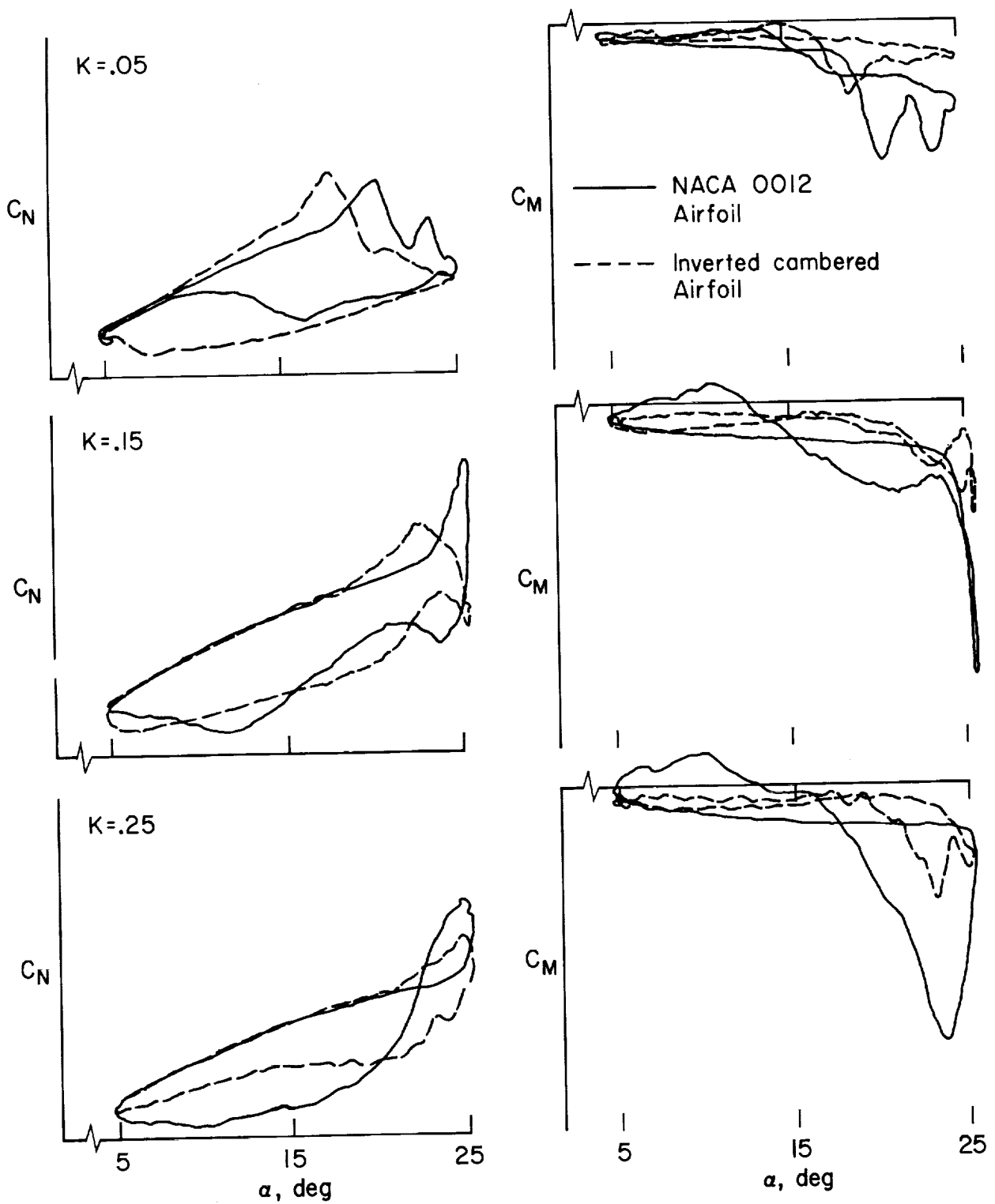
Figure 38.– Normal force and pitching moment on inverted cambered airfoil at k = 0.15; α = 15° + 10° sin ωt; Re = 2.5×10⁶.
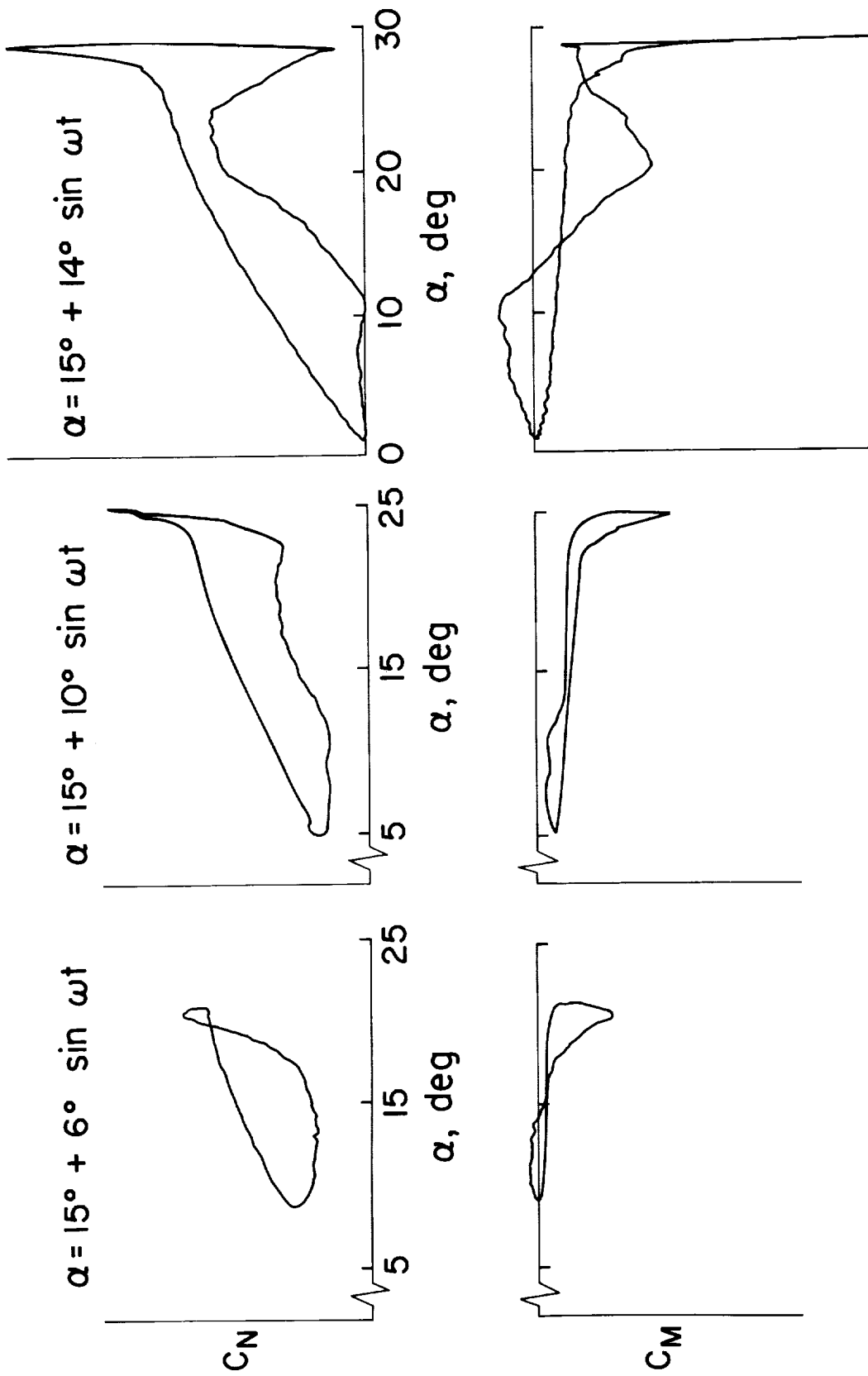
Figure 39.- Normal force and pitching moment on NACA 0012 airfoil at $\alpha_0 = 15°$ and $\alpha_1 = 6°$, $10°$, and $14°$; $k = 0.15$; $Re = 2.5 \times 10^6$.

75
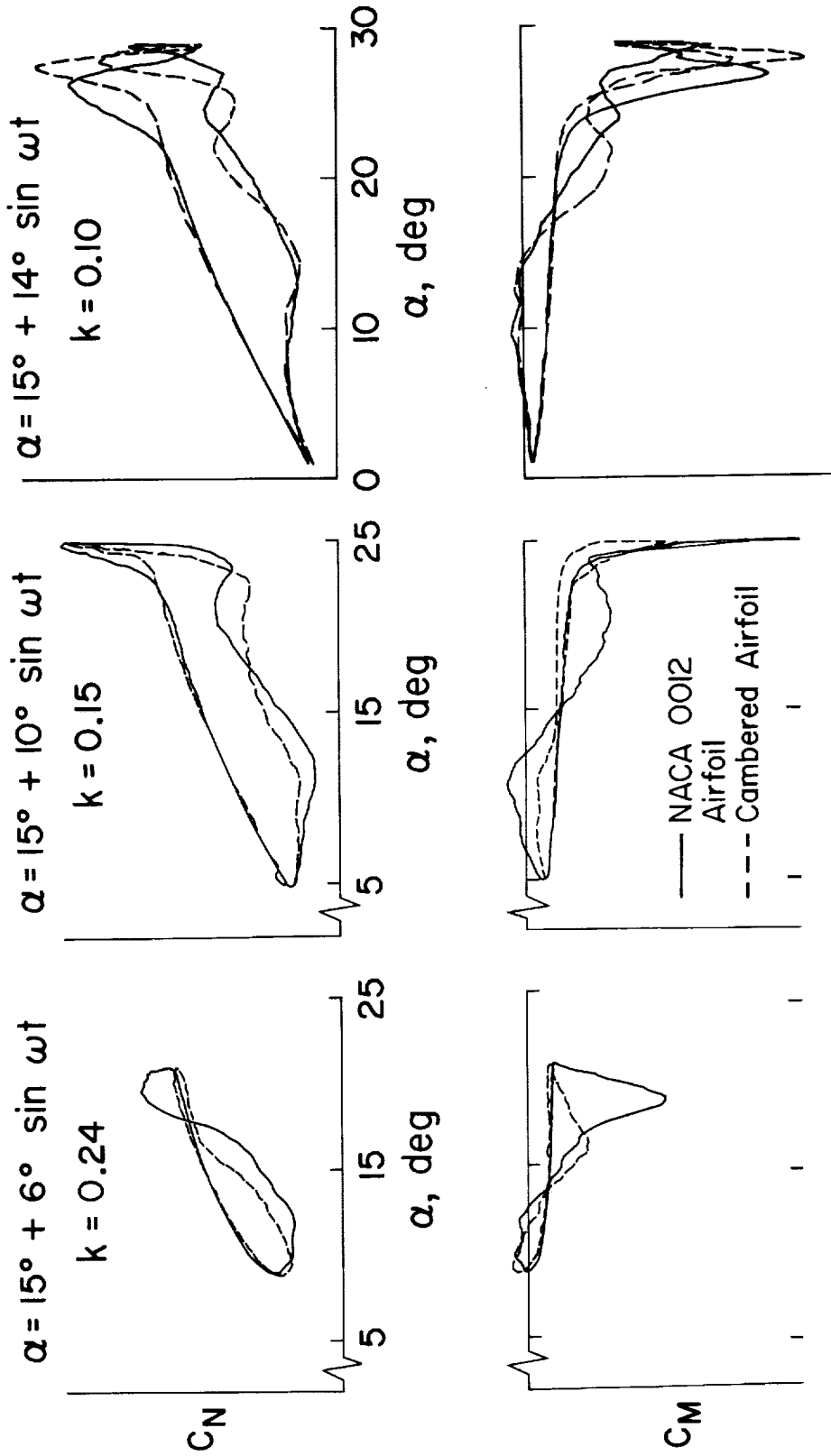
Figure 40.- Normal force and pitching moment on cambered airfoil for constant pitch rate at mean angle.

76
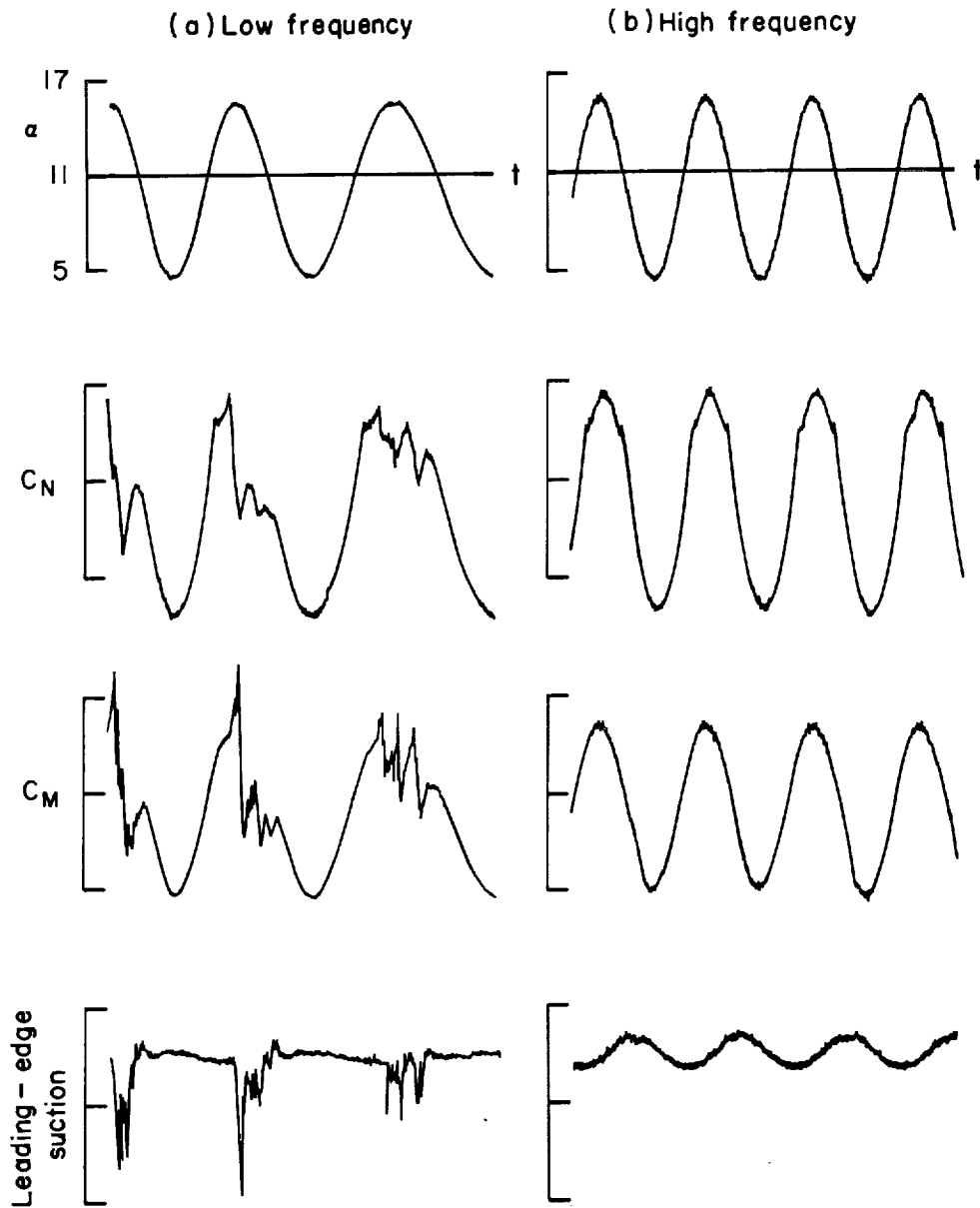
Figure 41.- Dependence of stall on reduced frequency for the NACA 0012 airfoil
at $\alpha = 11° + 6° \sin \omega t$ as shown by C_N, C_M, and leading-edge suction.
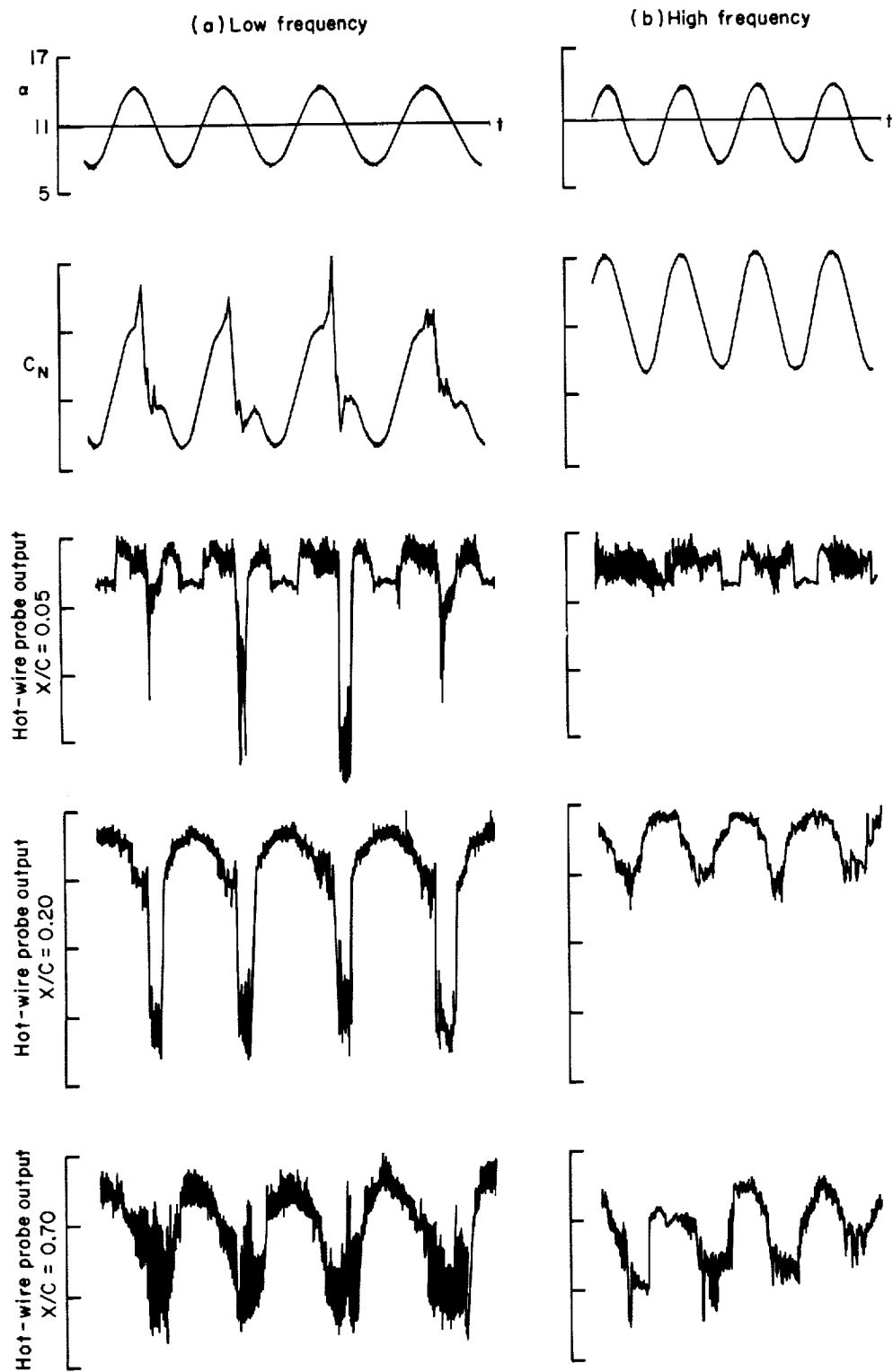
Figure 42.- Dependence of stall on reduced frequency for the NACA 0012 airfoil at $\alpha = 11° + 6°$ sin ωt as shown by C_N and hot-wire anemometer outputs.

78
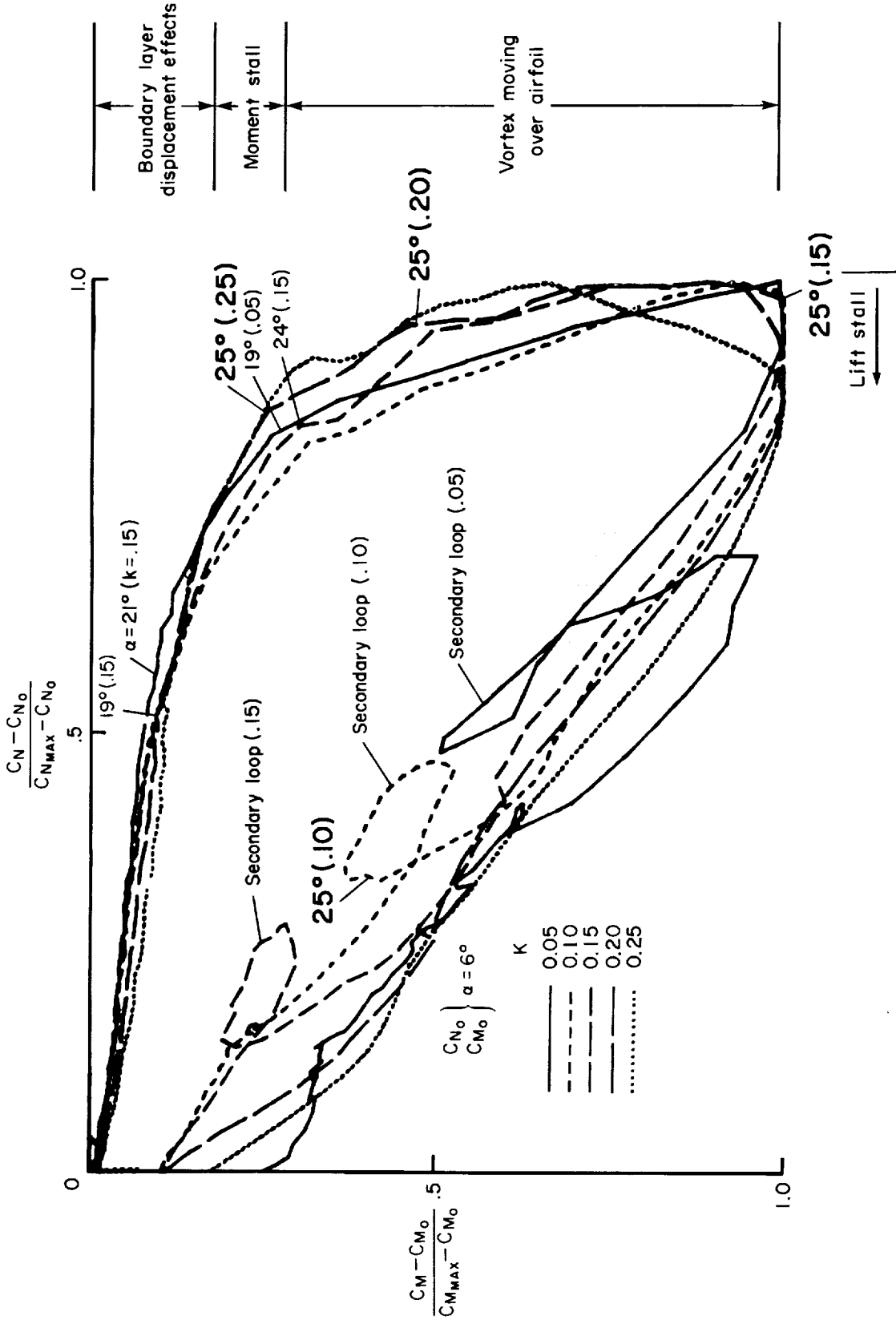
Figure 43.– C_N versus C_M crossplot for the NACA 0012 showing the effects of frequency variation.
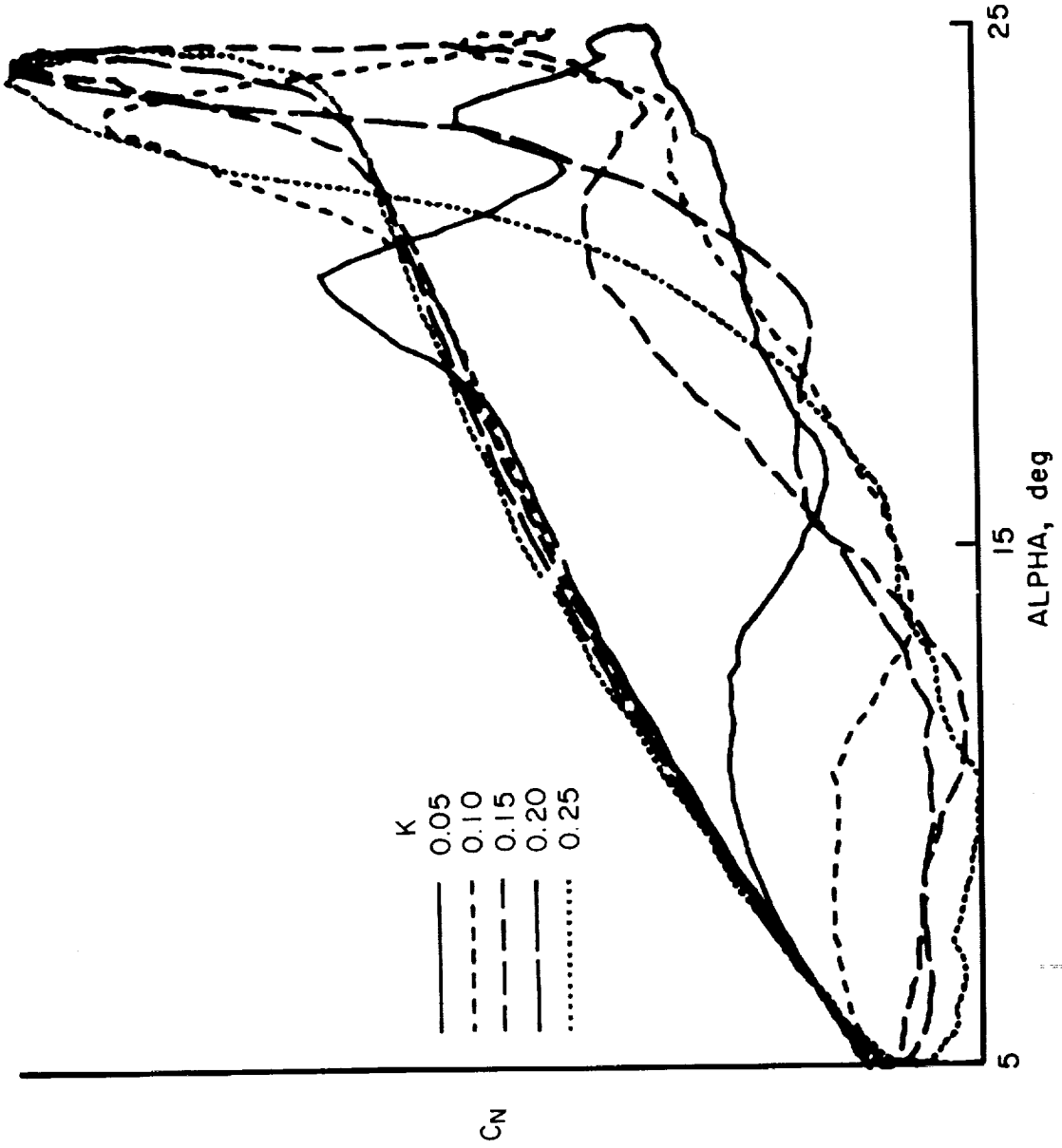
Figure 44.- Normal force coefficient for the NACA 0012 for a range of frequencies; $\alpha = 15° + 10°$ sin ωt; Re = 2.5×10^6.

80

Figure 45.- C_N versus C_M crossplot for the NACA 0012 for a range of Reynolds numbers; $k = 0.15$; $\alpha = 15° + 10°$ sin ωt.
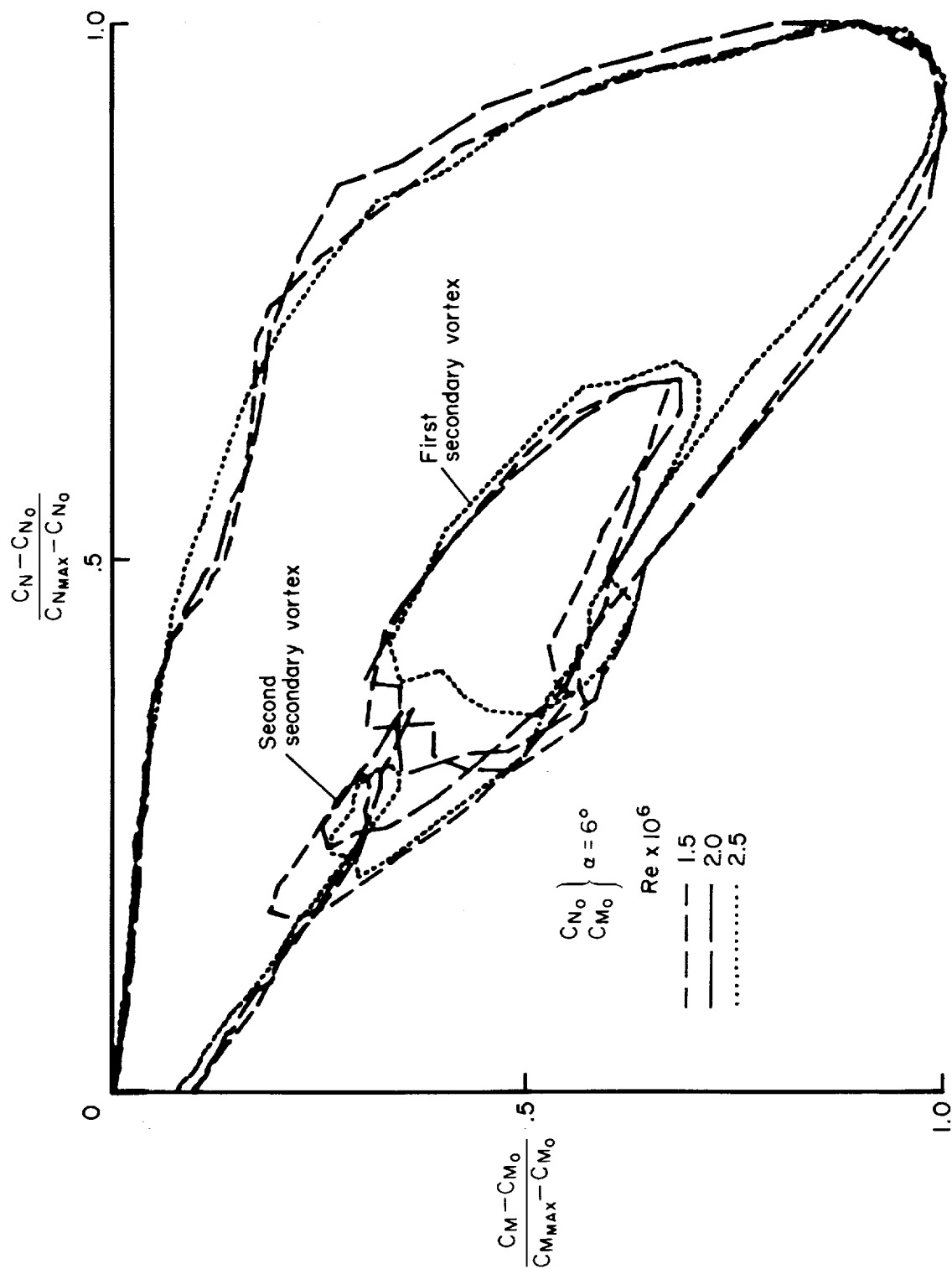
Figure 46.- C_N versus C_M crossplot for the NACA 0012 for a range of Reynolds numbers; $k = 0.15$; $\alpha = 15° + 14°$ sin ωt.

82
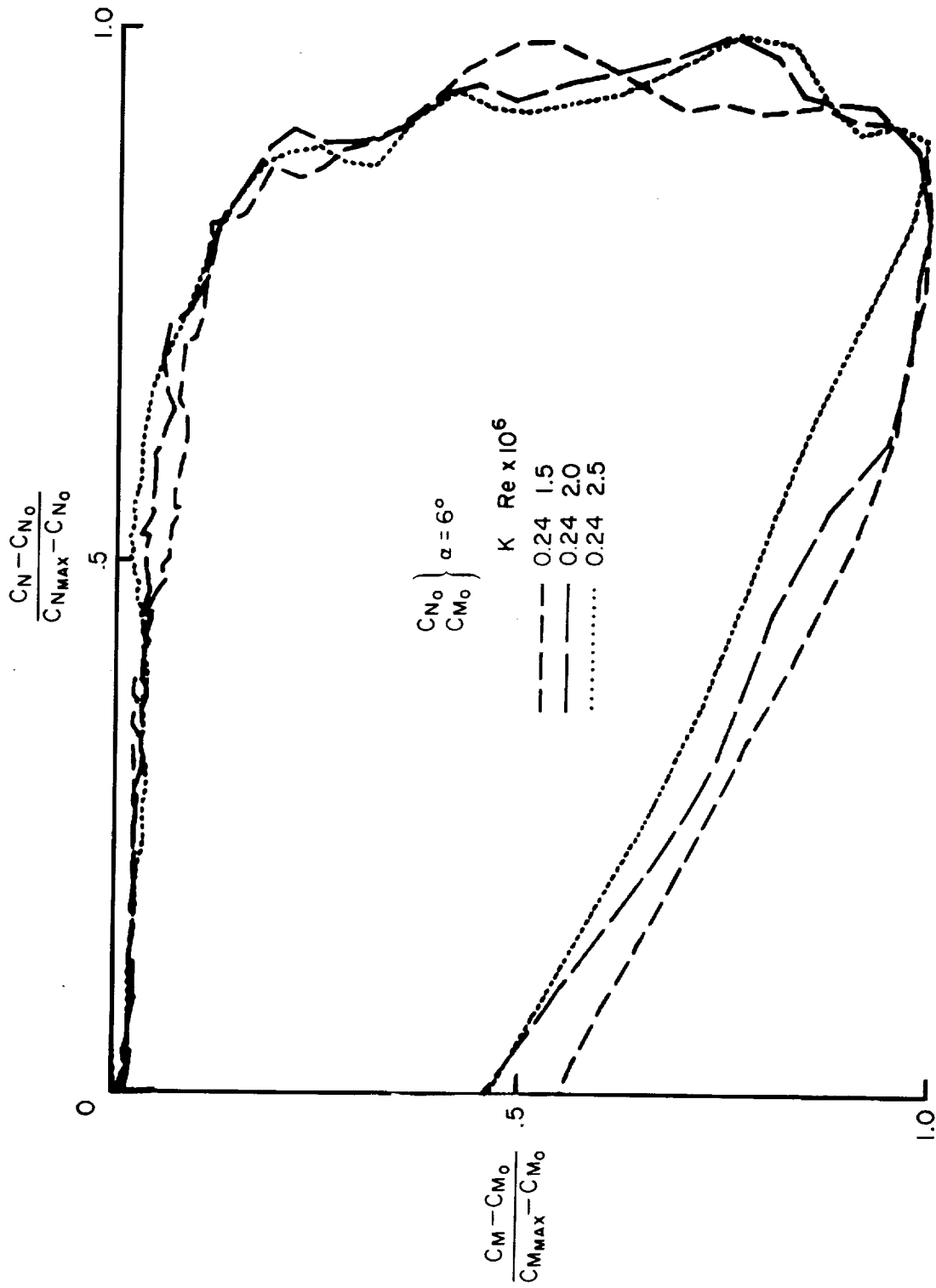
Figure 47.- C_N versus C_M crossplot for the NACA 0012 for a range of Reynolds numbers; $k = 0.24$; $\alpha = 15° + 6°$ sin ωt.
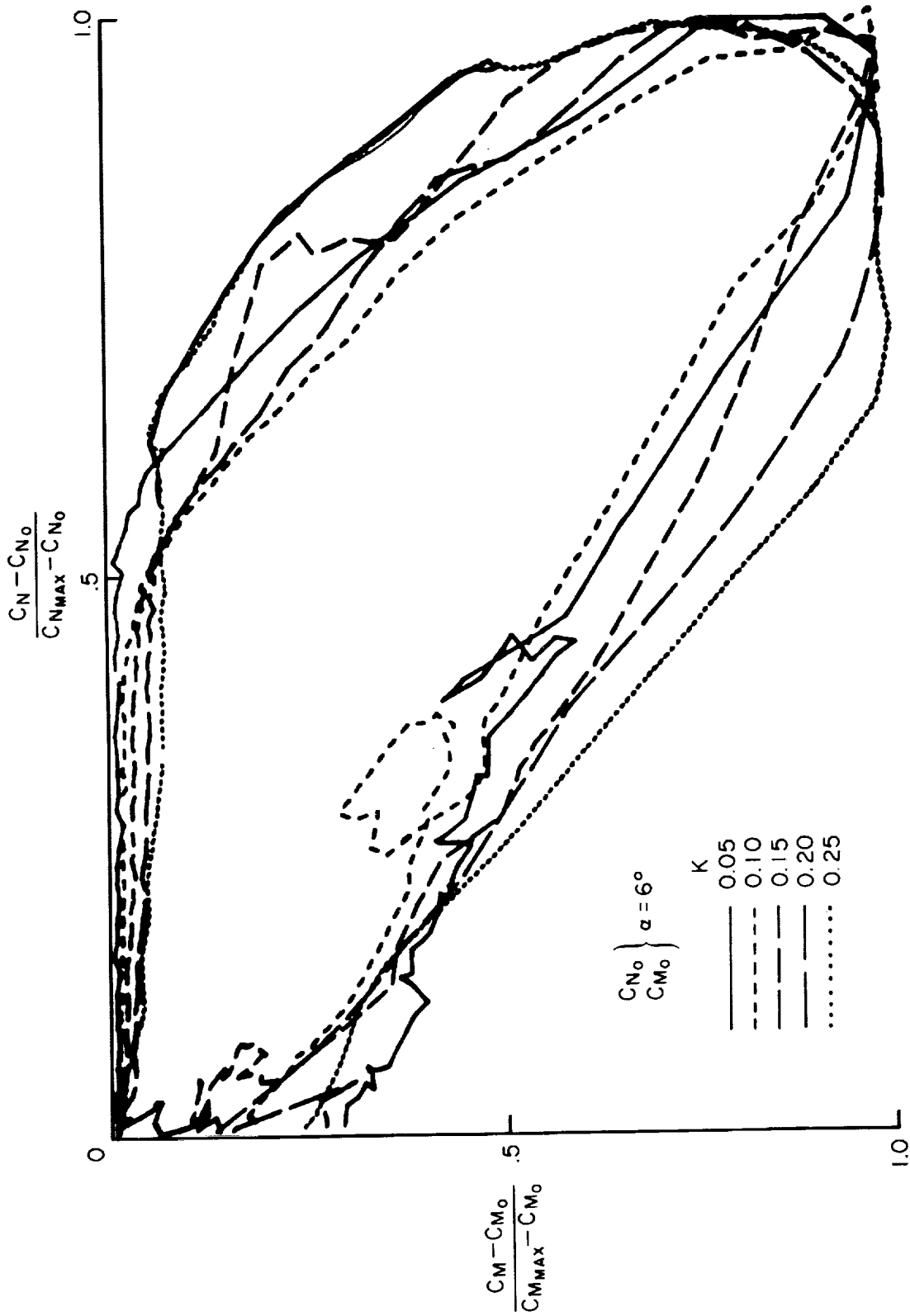
Figure 48.- C_N versus C_M crossplot for the cambered airfoil for a range of frequencies; $\alpha = 15° + 10° \sin \omega t$; Re = 2.5×10^6.

84
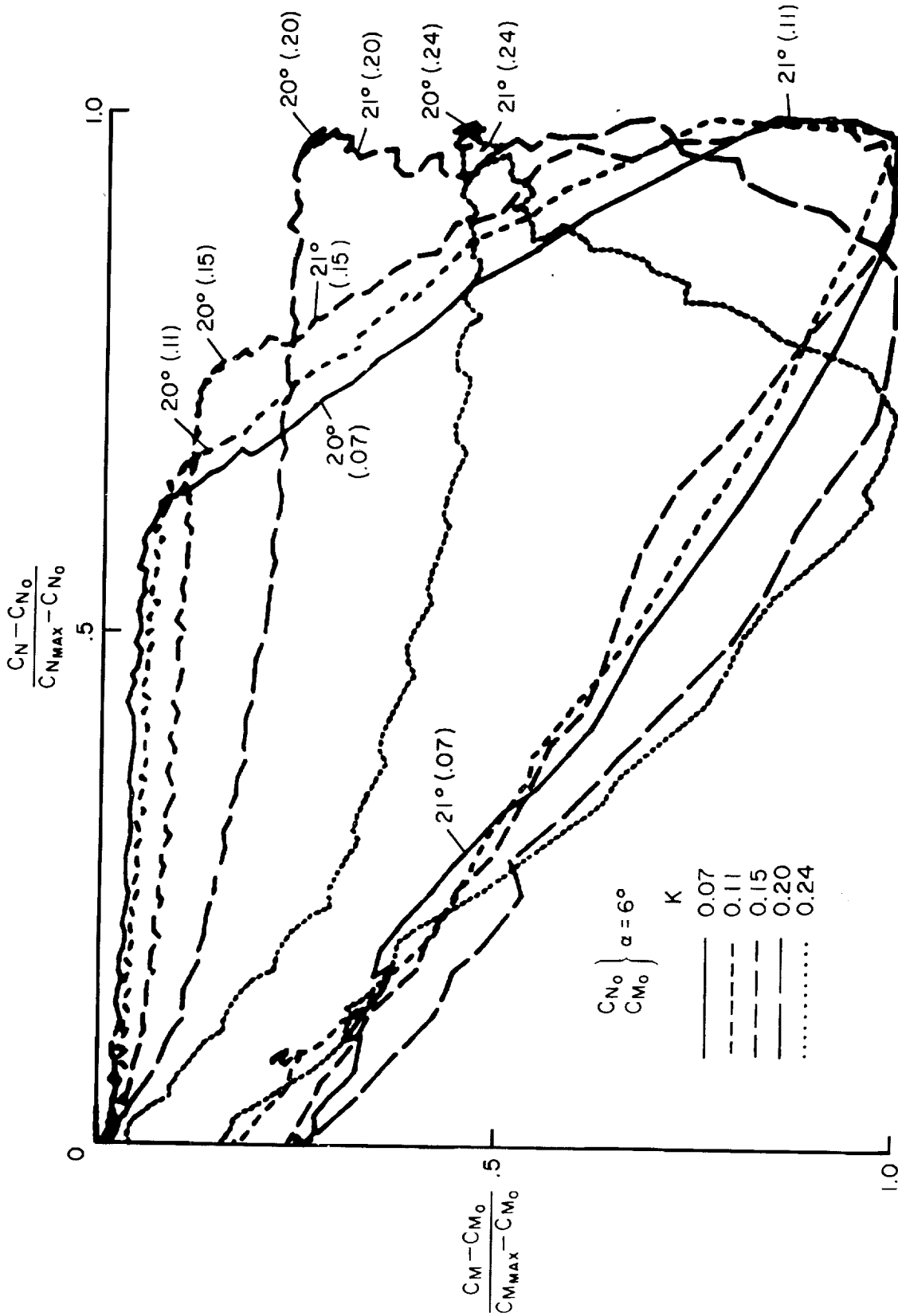
Figure 49.- C_N versus C_M crossplot for the cambered airfoil for a range of frequencies; $\alpha = 15° + 6° \sin \omega t$; Re = 2.5×10^6.
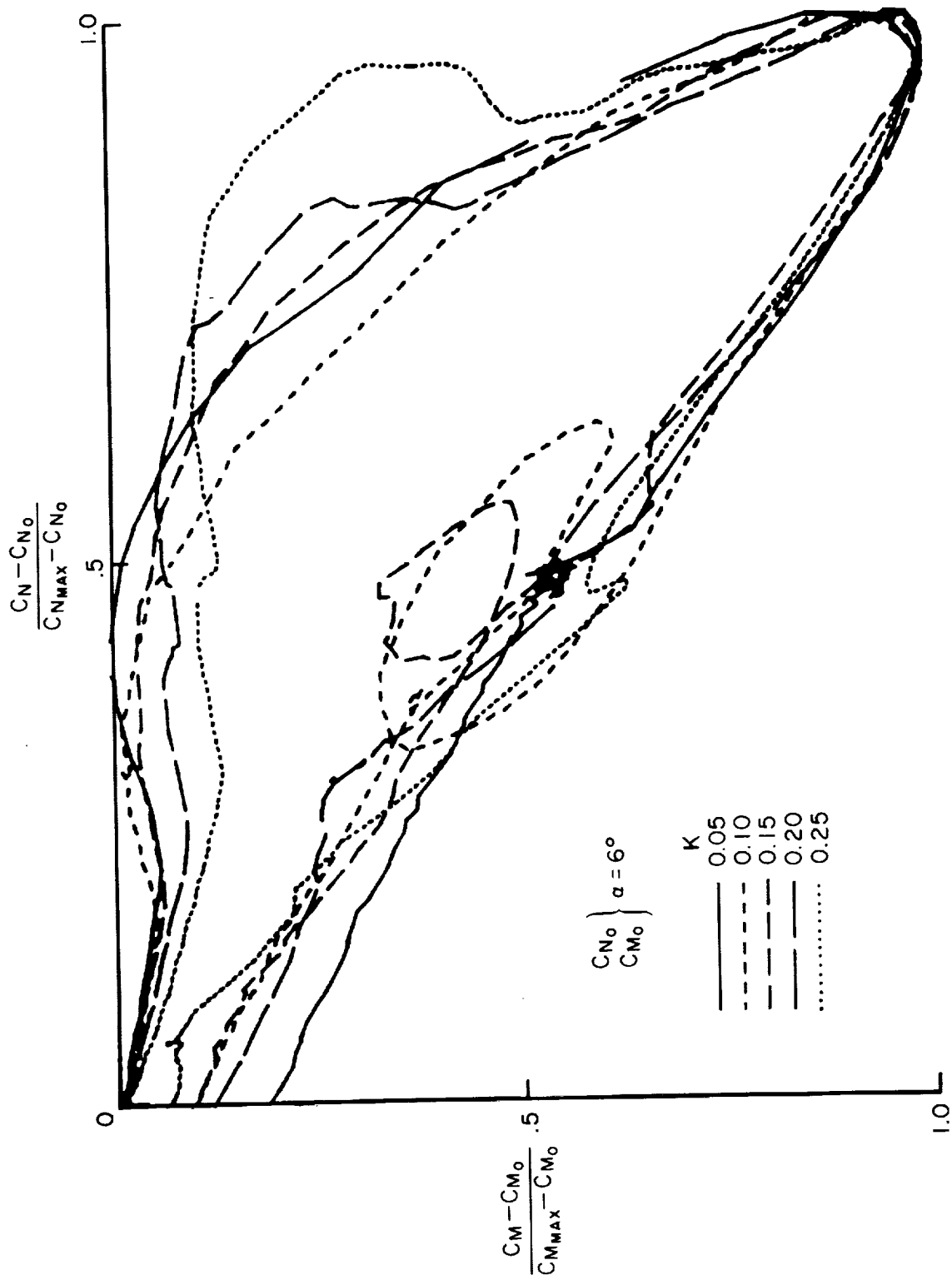
Figure 50.- C_N versus C_M crossplot for the sharp leading-edge airfoil for a range of frequencies; $\alpha = 15° + 10°$ sin ωt; Re = 2.5×10^6.

Legend:

$\left.\begin{array}{l} C_{N_O} \\ C_{M_O} \end{array}\right\} \alpha = 6°$

K	
0.05	
0.10	
0.15	
0.20	
0.25	

Axis labels:

$\dfrac{C_N - C_{N_O}}{C_{N_{MAX}} - C_{N_O}}$

$\dfrac{C_M - C_{M_O}}{C_{M_{MAX}} - C_{M_O}}$

86
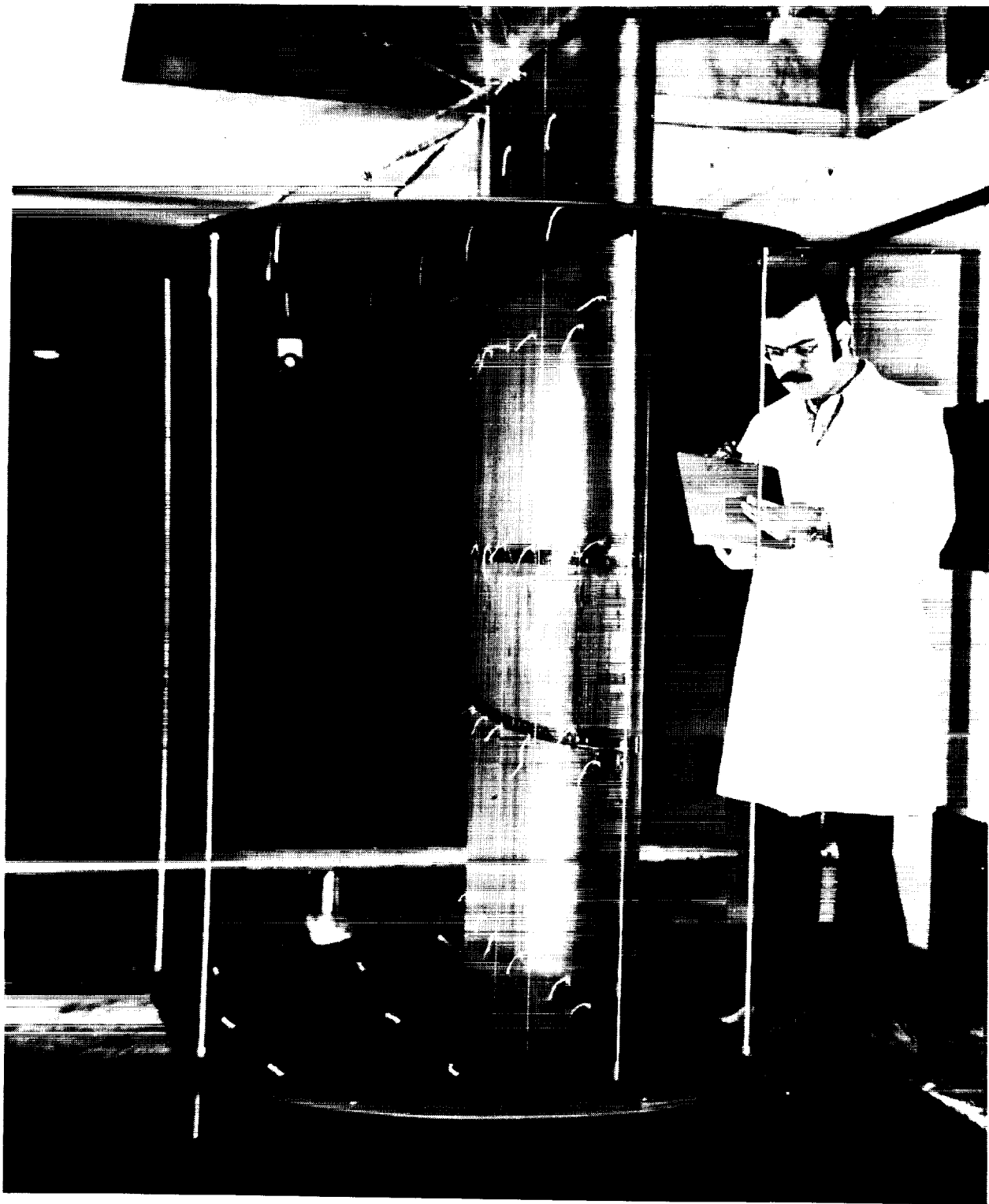
Figure 51.- View of airfoil with end plates.
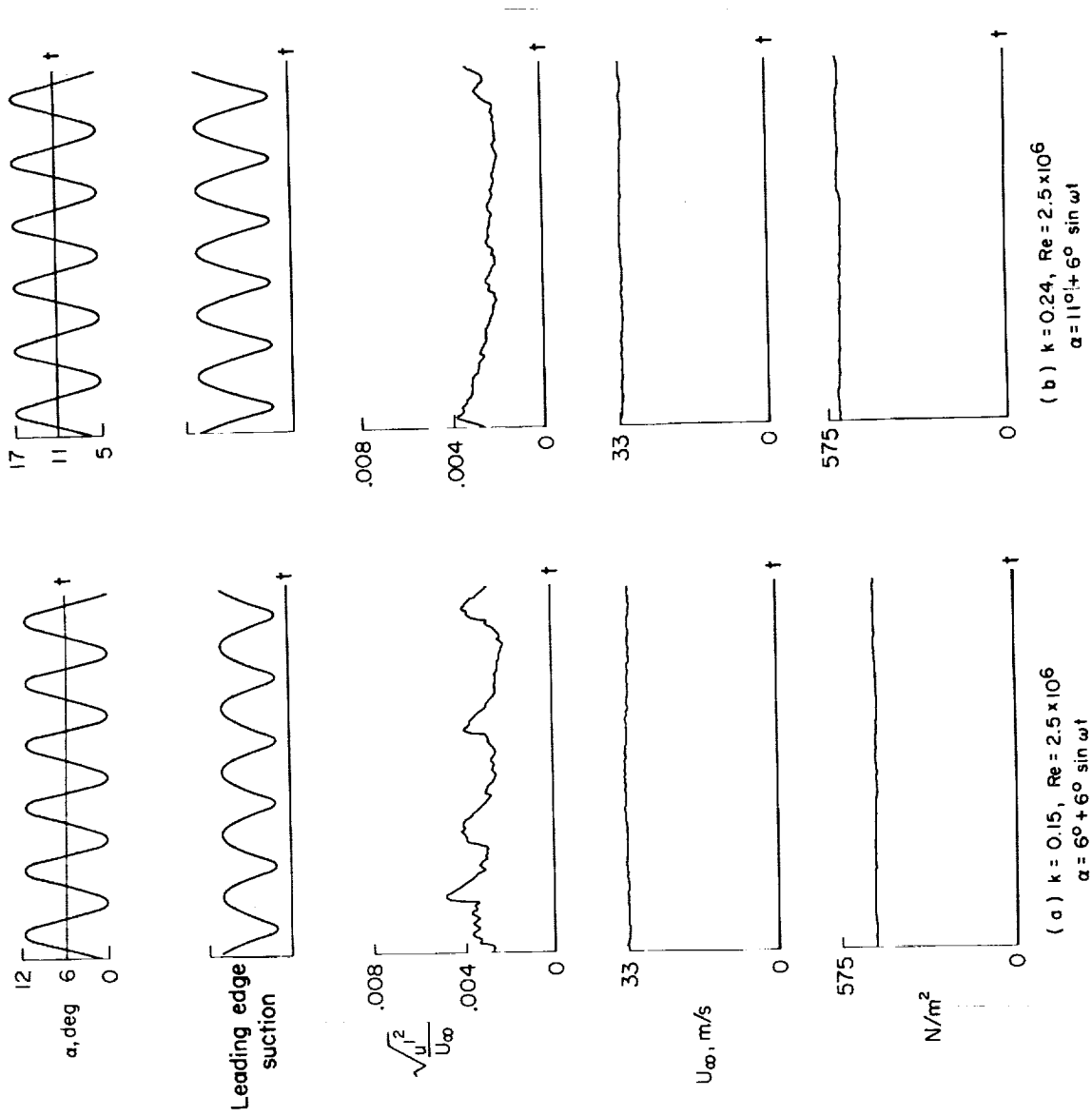
Figure 52.- Response of tunnel flow sensors to changes in mean airfoil angle for oscillations below stall.

88
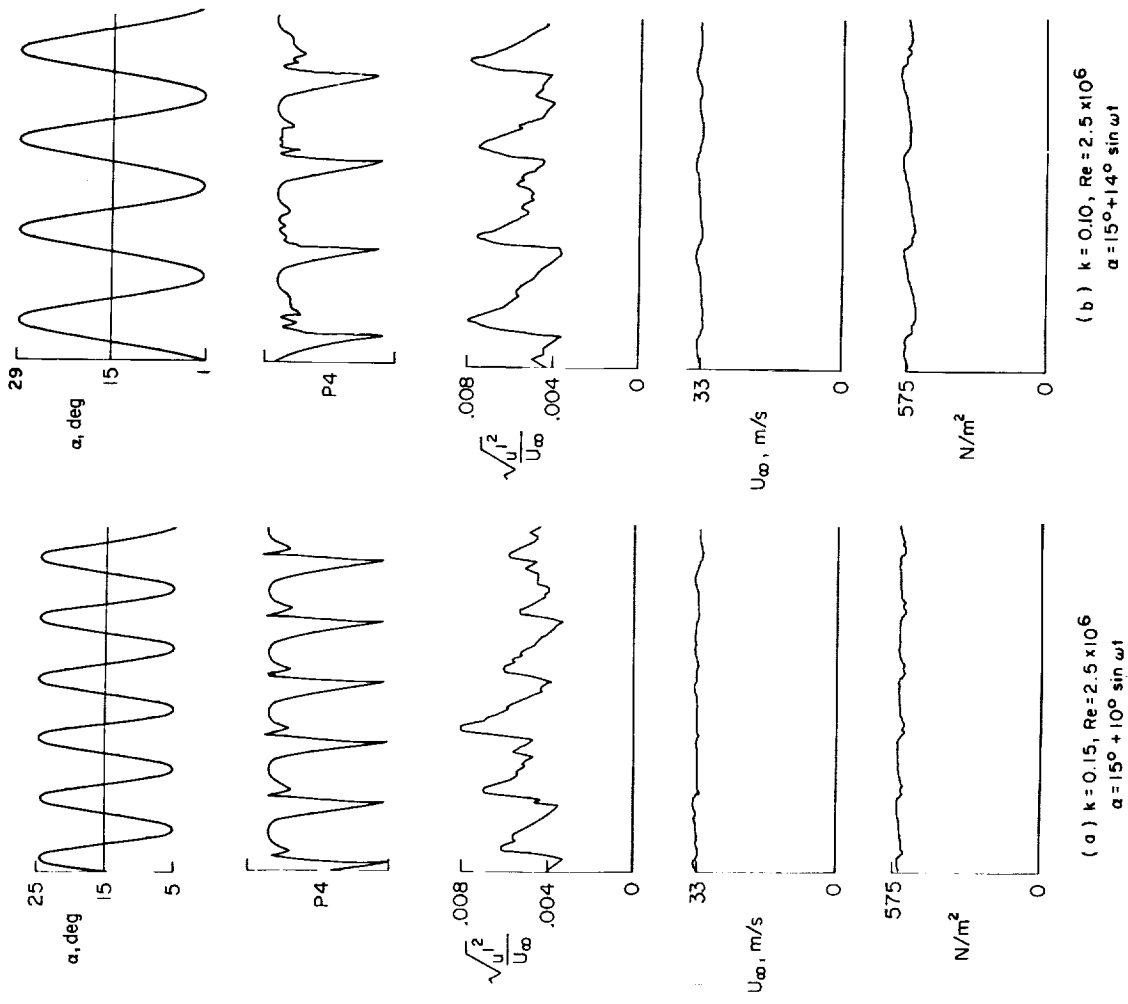
Figure 53.- Response of tunnel flow sensors to changes in airfoil oscillation amplitude for oscillation above stall.

(a) k=0.05, Re=2.5×10⁶
α=15° + 10° sin ωt

(b) k=0.15, Re=2.5×10⁶
α=15° + 10° sin ωt

(c) k=0.25, Re=2.5×10⁶
α=15° + 10° sin ωt
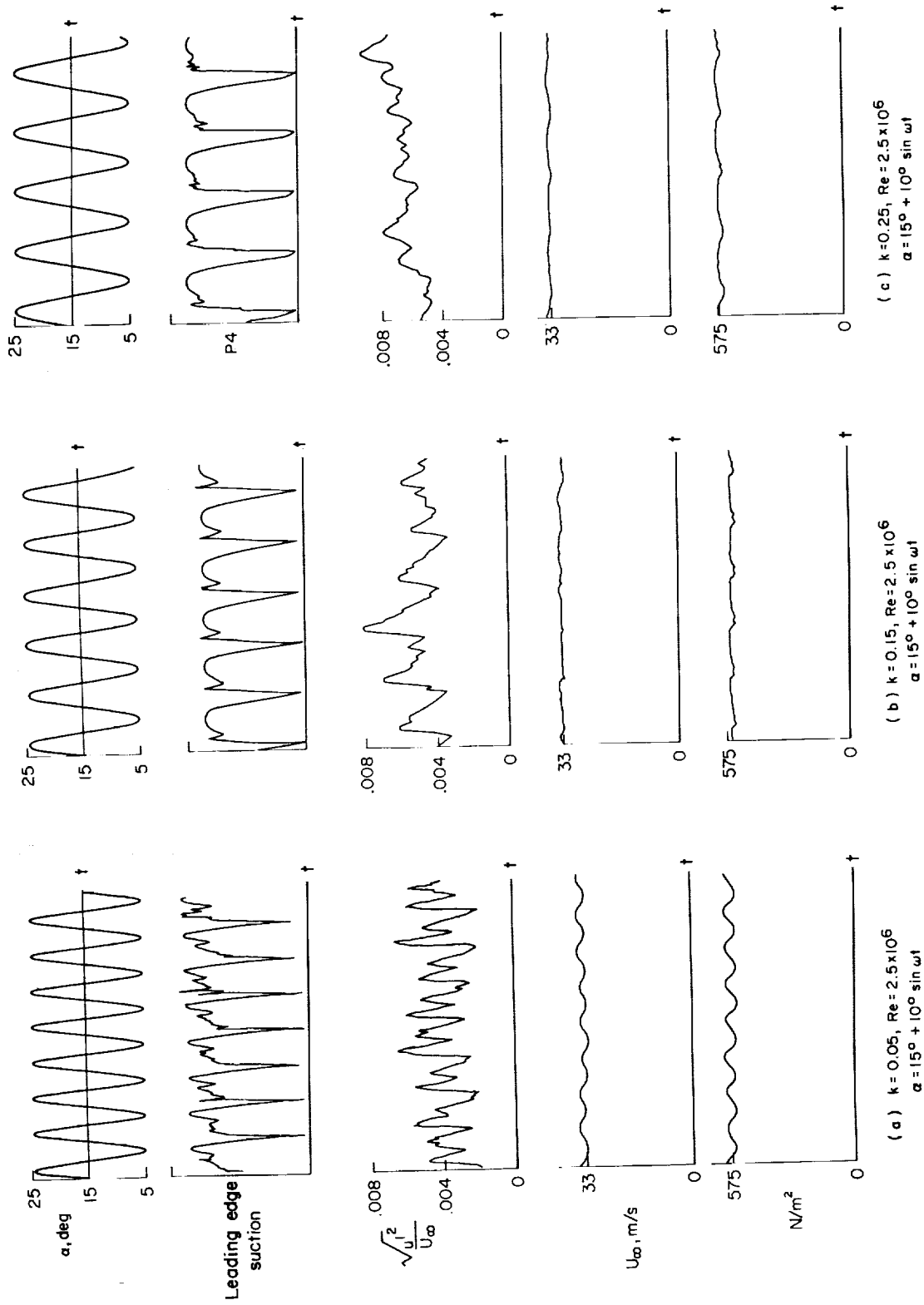
Figure 54.- Response of tunnel flow sensors to changes in oscillation frequency.

90
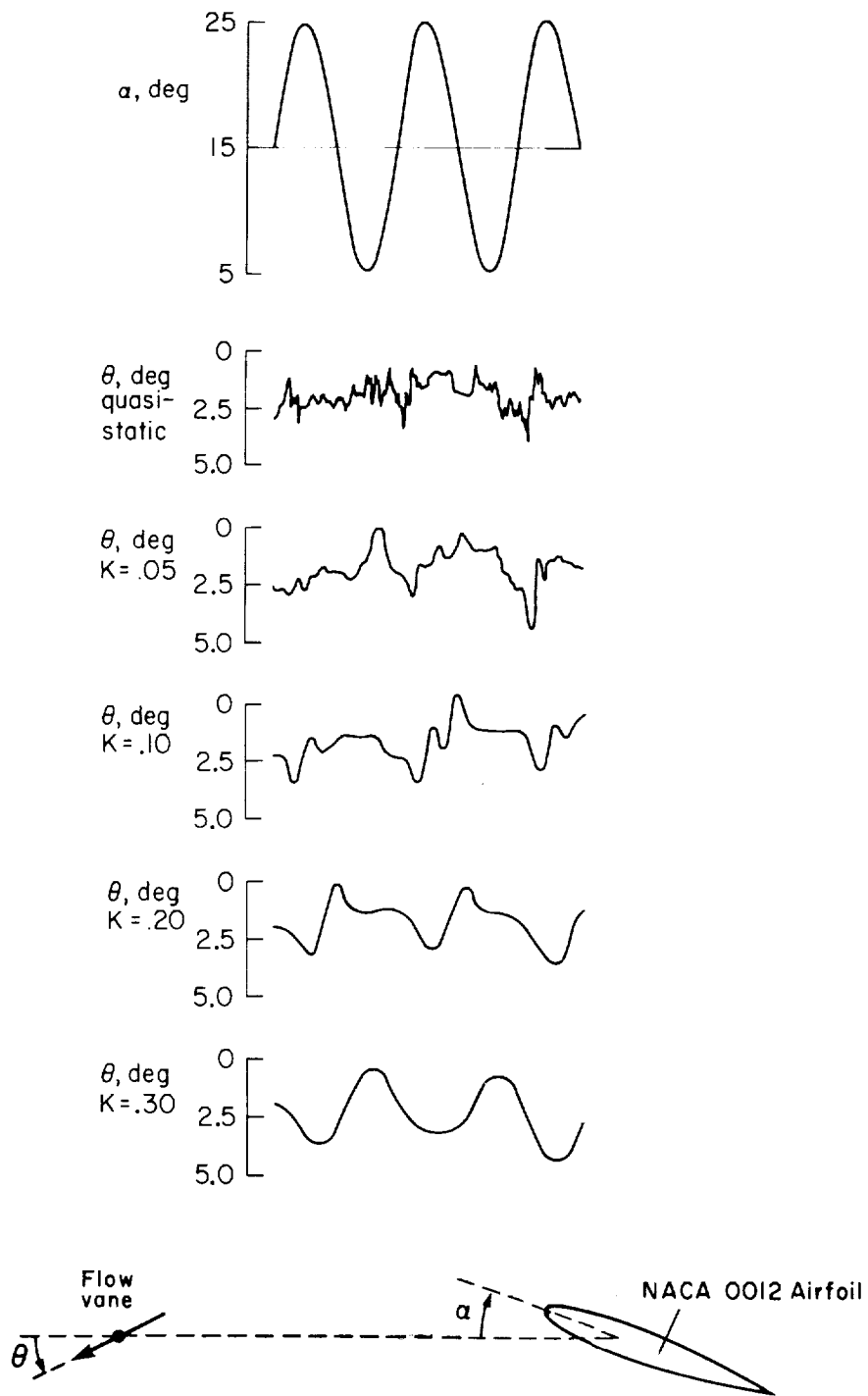
Figure 55.- Flow angularity at two chord lengths ahead of the model as a function of frequency.
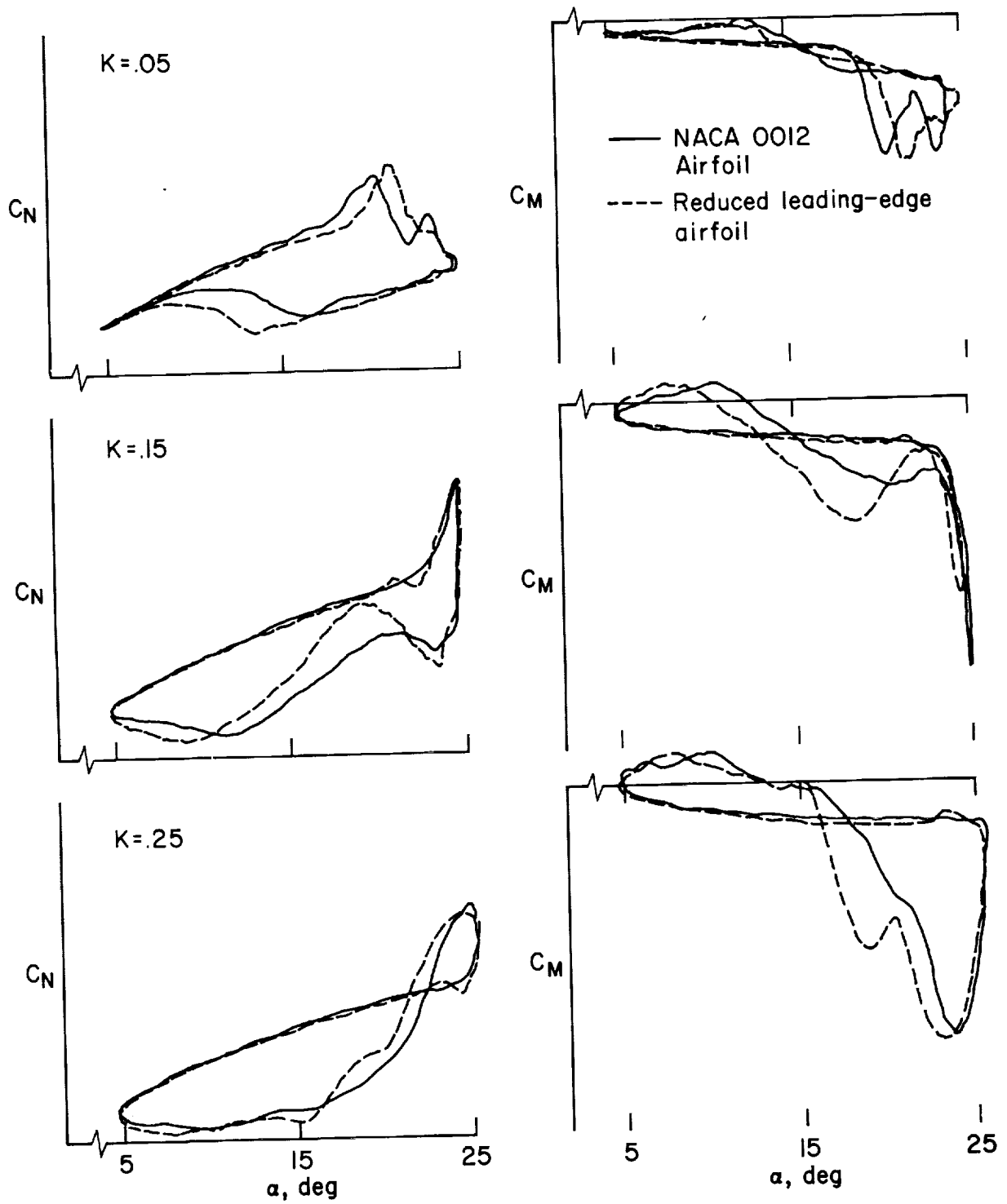
Figure 56.- Normal force and pitching moment on the reduced leading-edge airfoil at k = 0.05, 0.15, 0.25; α = 15° + 10° sin ωt; Re = 2.5×10⁶.

Figure 57.- Normal force and pitching moment on the reduced leading-edge
  airfoil with trip at k = 0.05, 0.15, 0.25; α = 15° + 10° sin ωt;
  Re = 2.5×10⁶.

Figure 58.- Movement of the flow reversal point as a function of incidence angle for the NACA 0012 with leading-edge trip as determined by hot-wire anemometer probes.
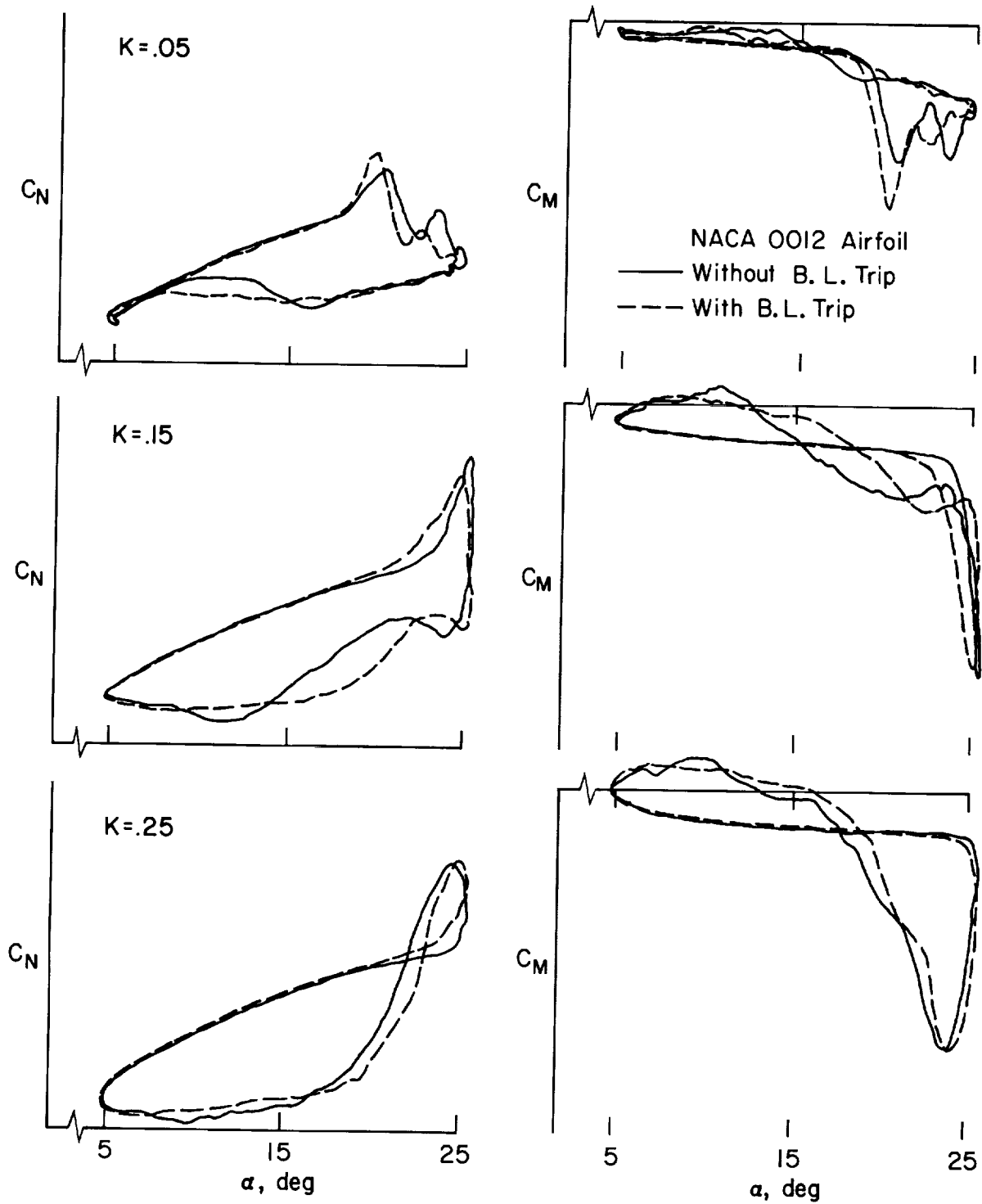
Figure 59.- Normal force and pitching moment on the NACA 0012 with trip vs NACA 0012 without trip; k = 0.05, 0.15, 0.25; α = 15° + 10° sin ωt; Re = 2.5×10⁶.
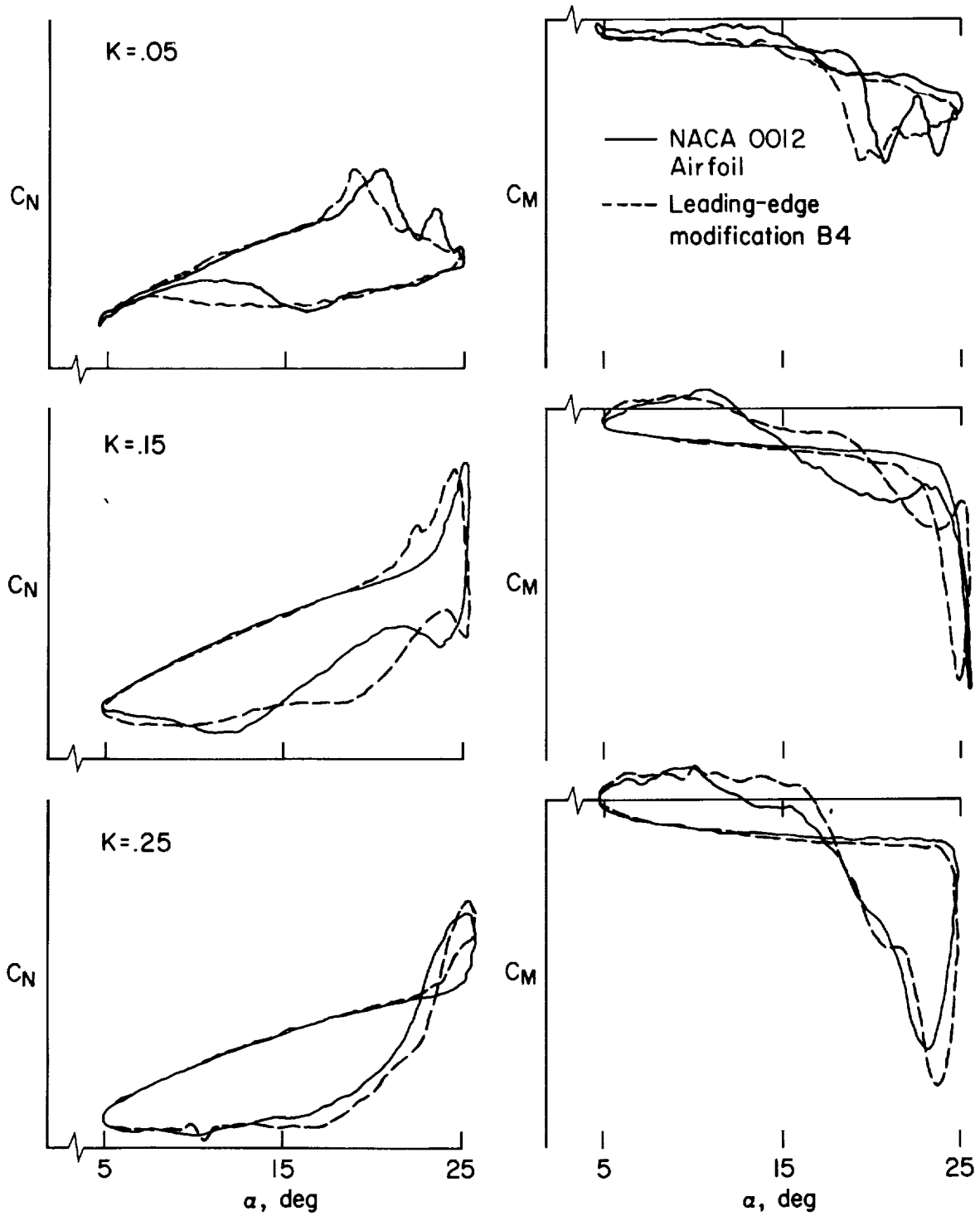
Figure 60.- Normal force and pitching moment on the airfoil with leading-edge
modification B1 at k = 0.05, 0.15, 0.25; α = 15° + 10° sin ωt;
Re = 2.5×10⁶.

Figure 61.– Normal force and pitching moment on the airfoil with leading-edge
modification B4 at k = 0.05, 0.15, 0.25; $\alpha = 15° + 10° \sin \omega t$;
$Re = 2.5 \times 10^6$.

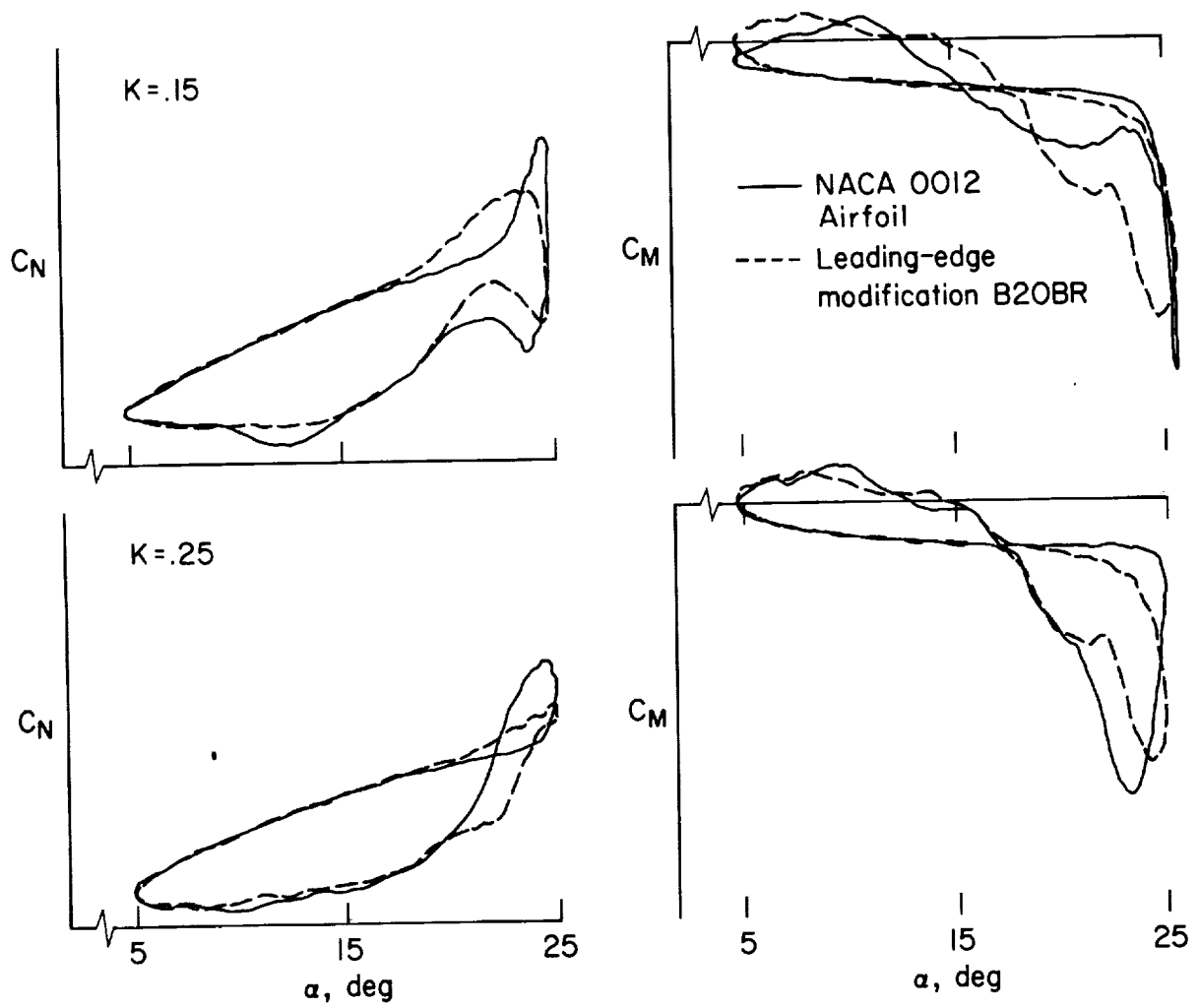Figure 62.- Normal force and pitching moment on the airfoil with leading-edge modification B20BR at   k = 0.15, 0.25; α = 15° + 10° sin ωt; Re = 2.5×10⁶.
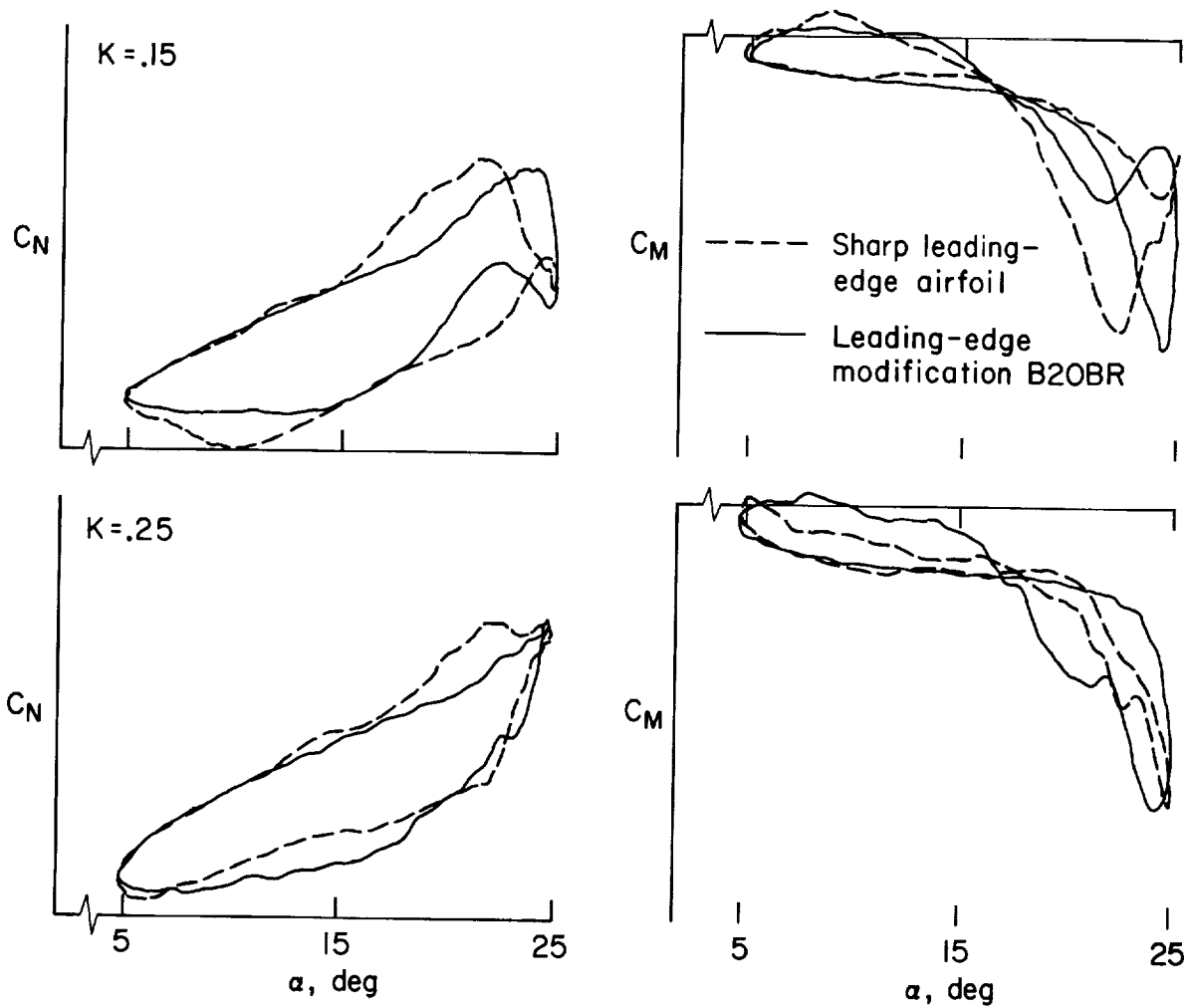
Figure 63.- Normal force and pitching moment on the airfoil with leading-edge modification B20BR vs sharp leading-edge at k = 0.15, 0.25; α = 15° sin ωt; Re = 2.5×10⁶.